Università degli Studi di Trieste
Dipartimento di Fisica

Master Degree in Physics
Curriculum in Nuclear and Subnuclear Physics

Characterization of Z$\gamma\gamma$ and W$\gamma\gamma$ events in pp collisions at the LHC and limits on anomalous couplings

Supervisor:
Dott. Vieri Candelise
Co-Supervisor:
Prof. Giuseppe Della Ricca

Candidate:
Giulia Sorrentino

Anno Accademico 2018/2019

Università degli Studi di Trieste
Dipartimento di Fisica

Laurea Magistrale in Fisica
Curriculum in Fisica Nucleare e Subnucleare

Caratterizzazione di eventi Z$\gamma\gamma$ e W$\gamma\gamma$ in collisioni pp a LHC e limiti su accoppiamenti anomali

Relatore:
Dott. Vieri Candelise
Correlatore:
Prof. Giuseppe Della Ricca

Candidato:
Giulia Sorrentino

Anno Accademico 2018/2019

A mia madre, la mia ancora e il mio vento
A mio padre, ovunque sia

Sommario

Il Modello Standard della Fisica delle Particelle è uno dei traguardi più significativi della fisica moderna. É infatti in grado di descrivere le particelle elementari e le loro reciproche interazioni, oltre a fornire un accurato modello teorico per tre delle quattro forze fondamentali dell'Universo. La validità del Modello Standard è stata confermata nel corso degli anni da un gran numero di esperimenti, i cui risultati si sono rivelati in eccellente accordo con le predizioni teoriche da esso fornite. Con l'avvento del *Large Hadron Collider* (LHC), il più grande e potente acceleratore di particelle al mondo, e con la successiva scoperta del bosone di Higgs, il Modello Standard può definirsi completo, nel modo in cui era stato teorizzato in origine. Esistono tuttavia alcuni fenomeni fisici che non sono completamente spiegati dal Modello Standard: per questo, attualmente, gli scienziati sono alla ricerca di una nuova teoria in grado di estendere e sviluppare il modello teorico attuale in modo da fornire una spiegazione esaustiva delle evidenze sperimentali osservate e della relativa fisica ad esse associata. Sono già state sviluppate diverse teorie oltre il Modello Standard, sebbene finora nessuna di queste sia stata ancora provata, e la ricerca di fisica oltre il Modello Standard è diventata pertanto un elemento cruciale, in grado di fornire agli scienziati un valido punto di partenza sulla base del quale sviluppare la nuova teoria. Ricerche di fisica oltre il Modello Standard sono attualmente in corso ad LHC, effettuate mediante due principali approcci d'indagine: il primo consiste nella ricerca diretta di nuove particelle, il secondo nella ricerca di interazioni nuove tra le particelle già esistenti, misurabili come discrepanze dei risultati sperimentali rispetto alle predizioni teoriche del Modello Standard. Tuttavia, poichè finora nessuna delle ipotetiche nuove particelle è stata ancora scoperta, è probabile che l'energia necessaria alla loro produzione sia molto distante dalle energie raggiungibili dagli attuali acceleratori e il secondo approccio alla ricerca di nuova fisica appare, al momento, come il più promettente. I processi a due o tre bosoni in particolare, sono sensibili all'auto-interazione tra bosoni vettori dell'interazione elettrodebole a causa della presenza di accoppiamenti di gauge tripli e quadrupli, i quali potrebbero essere modificati da eventuali effetti di nuova fisica dando origine ai cosiddetti accoppiamenti anomali. Nel presente lavoro di tesi sono stati studiati i processi $W\gamma\gamma$ e $Z\gamma\gamma$, sono state estratte le distribuzioni della sezione d'urto differenziale utilizzando campioni Monte Carlo

a 13 TeV e sono state calcolate le incertezze teoriche ad esse associate. Le distribuzioni della sezione d'urto differenziale rappresentano il punto di partenza per l'estrazione dei limiti attesi per gli accoppiamenti di gauge anomali. Accoppiamenti quartici anomali infatti produrrebbero un aumento di eventi W$\gamma\gamma$ e Z$\gamma\gamma$ ad alti valori di momento, e una stima teorica di tale incremento si può ottenere confrontando le distribuzioni Monte Carlo con nuove distribuzioni ottenute a partire da simulazioni in cui sono stati introdotti effetti di accoppiamenti anomali. Nel primo capitolo di questa tesi viene introdotto il Modello Standard, insieme ad una breve descrizione dei suoi principali aspetti teorici, quali l'interazione elettrodebole, l'interazione forte e il meccanismo di Brout-Englert-Higgs. Vengono inoltre presentati gli accoppiamenti tripli e quadrupli così come predetti dalla teoria. Nel secondo capitolo vengono introdotti gli accoppiamenti anomali nell'ambito della teoria effettiva di campo, descritta nella prima parte, mentre nella seconda parte del capitolo vengono presentati i diversi processi a multi-bosoni attualmente in studio a LHC. Particolare attenzione viene dedicata all'analisi a 8 TeV svolta dall'esperimento *Compact Muon Solenoid* (CMS) per le produzioni W$\gamma\gamma$ e Z$\gamma\gamma$ e per la relativa estrazione dei limiti sugli accoppiamenti quartici anomali. I generatori di eventi Monte Carlo sono descritti nel capitolo 3 insieme alla struttura delle collisioni protone-protone a LHC, specificando inoltre i generatori usati per la produzione dei campioni a 13 TeV. Nel capitolo 4, LHC e l'esperimento CMS vengono presentati e brevemente descritti. Il capitolo 5 è dedicato alla caratterizzazione dello spazio delle fasi degli eventi W$\gamma\gamma$ e Z$\gamma\gamma$. Le distribuzioni della sezione d'urto differenziale sono ottenute mediante l'utilizzo di una routine Rivet, la cui validità viene testata nella seconda parte del capitolo. Le selezioni applicate allo spazio delle fasi vengono qui riportate in dettaglio. Il capitolo 6 è dedicato allo studio delle incertezze teoriche che interessano le misure di sezione d'urto. Tali incertezze sono dovute alla determinazione delle funzioni di distribuzione partoniche e della costante di accoppiamento forte α_S, e alla scelta delle costanti di rinormalizzazione e di fattorizzazione. Il calcolo di tali incertezze viene eseguito a partire dalle distribuzioni della sezione d'urto differenziale, in modo da poter fornire una stima dell'incertezza teorica totale attesa sulla misura della sezione d'urto. Infine vengono tratte le conclusioni e vengono presentate le procedure necessarie all'estrazione dei limiti attesi sugli accoppiamenti anomali.

Contents

Introduction

The Standard Model (SM) of particle physics is one of the most outstanding achievement of modern physics. It describes elementary particles and their interactions, and it provides an accurate theoretical model for three of the four fundamental forces of the Universe. The validity of the Standard Model have been confirmed over the years by a wide number of experiments that observed excellent agreement between experimental results and model predictions. With the advent of the Large Hadron Collider (LHC), the largest and most powerful particle accelerator of the world, and the Higgs boson discovery, the SM has been finally completed as it was originally theorized. There exists some physics phenomena however that are not fully explained by the Standard Model. This persuaded physicists to seek for a new theory, an extension or a development of the current model, in order to obtain a more comprehensive interpretation of experimental evidence and of the underlying physics. Many Beyond Standard Model (BSM) theories have been developed in the past years although none of them have been proved yet, and therefore the search for BSM physics has remarkably increased its importance, in order to provide to scientists a decisive starting point to elaborate a good model for new physics. Search for BSM are now performed at the LHC, using two different approaches: one consists in looking for new physics directly, via the production of new particles, the other looks for novel interactions of the SM particles, measurable as small deviations from SM predictions. However, since none of the hypothesized new particles have been discovered yet, it seems quite probable that the energy required for their production it is considerably far from the current accelerators capacity and thus, at present, the second approach to BSM search appears to be more efficient. In particular, diboson and triboson processes are sensitive to the self-interaction of electroweak vector bosons via triple and quartic gauge couplings (GC) that can be modified by BSM effects giving rise to the so-called anomalous gauge couplings. In this thesis work, the differential cross section distributions for $W\gamma\gamma$ and $Z\gamma\gamma$ processes are obtained from 13 TeV Monte Carlo samples, and the theoretical uncertainties are evaluated. The differential cross section distributions are needed in the evaluation of the expected limits on the anomalous gauge couplings. Anomalous GC increase the production of $W\gamma\gamma$ and $Z\gamma\gamma$ events at high momentum scales, and this enhancement can be estimated by means of comparisons between MC simulations embedding anomalous GC effects and Standard Model Monte Carlo simulations. In the first chapter of this thesis the Standard Model and its particle content are introduced, together with a brief overview of its main theoretical aspects: the electroweak interaction, the strong interaction and the Brout-Englert-Higgs mechanism. In particular, the SM triple and quartic gauge couplings are described. The second chapter is focused on the anomalous GC, interpreted in the framework of the Effective Field Theory which is described in the first part of the chapter, while in the second part a review of the the multiboson processes under study at LHC is reported. A special focus is placed on the 8 TeV analysis performed by the Compact Muon Solenoid (CMS) experiment for the W$\gamma\gamma$ and Z$\gamma\gamma$ production and the extraction of the limits on anomalous quartic GC. Monte Carlo event generators are described in chapter 3, together with the structure of a proton-proton collision at LHC. The generators used for the 13 TeV samples production are specified. The LHC and the CMS experiment are then introduced and briefly described in chapter 4. In chapter 5, the characterization of the W$\gamma\gamma$ and Z$\gamma\gamma$ phase space is performed, using the Rivet software, in order to obtain the differential cross section distributions, and the selections applied to MC samples are described in detail. In addition, the validity of the Rivet routine developed for the analysis is tested. In chapter 6 the theoretical uncertainties affecting cross section measurements, due to experimental of Parton Distribution Functions, α_S and to the choice of the renormalization and factorization scale, are presented, together with the current prescriptions for their correct calculation. The evaluation of the errors is then performed on the differential cross section distribution, to estimate the expected theoretical uncertainties on the cross section measurement. In the end the conclusions are drawn, and the subsequent procedures for the extraction of the expected limits on anomalous couplings are presented.

Chapter 1

Electroweak Interactions

In the first chapter, the Standard Model of particle physics is introduced, together with its particle content and its main theoretical features. The electroweak interaction, the strong interaction, and the Higgs-Englert-Brout mechanism are described. In the last part of the chapter, the issues that the Standard Model is now facing are briefly listed, and an overview of the Beyond Standard Model theories is presented.

1.1 The Standard Model

The Standard Model (SM) of particle physics is the theoretical model that describes elementary particles and their reciprocal interactions. It includes three of the four fundamental forces existing in the Universe: the electromagnetic, the electroweak and the strong force. The gravitational force is assumed to be too weak to have a significant role in elementary particle physics. According to the SM, there are three kind of elementary particles: leptons, quarks, and mediators (Figure 1.1). The constituents of matter are leptons and quarks, 1/2-spin particles called *fermions.* The dynamics of the fermions are described by the Dirac equation of relativistic quantum mechanics, whose important consequence is that, for each of the twelve fermions, an antiparticle with exactly the same mass exists, with opposite charge. Antiparticles are conventionally labelled with a bar on top (i.e. an antiquark is labelled as $\bar{q}$). There are three negatively charged leptons, the electron (e), the muon (μ) and the tau (τ), and three neutral leptons named neutrinos (ν_e, ν_μ, ν_τ). Leptons are divided in three *generations*, each one constituted of a charged lepton and its corresponding neutrino; the charged lepton mass increases from the first ($m_e \simeq 0.511$ MeV) to the third ($m_\tau \simeq 1777$ MeV) family, while neutrino masses are very small ($\lesssim$ 1 eV) and their hierarchy has not be determined yet. There are six *flavour* of quarks: up (u), down (d), charm (c), strange (s), top (t) and bottom (b). Quarks are classified by the charge and the isospin 3-component: there are three up-type quarks (the isospin 3-component is 1/2 and the charge is 2/3 of the electron charge), and three down-type quarks (the isospin 3-component is -1/2 and the charge is -1/3 of the electron charge). As leptons, quarks are divided in three generations, each of them constituted of an up-type quark and a down-type quark. Due to the nature of strong interactions, they can not be observed as free particles but they are always confined in bound states, known as *hadrons*. Up to now, the only hadronic states that have been observed are: *mesons*, which consist of a quark and an antiquark ($q\bar{q}$), *baryons*, which consist of three quarks (qqq), and *antibaryons*, which consist of three antiquarks ($\bar{q}\bar{q}\bar{q}$). Each of the three forces of

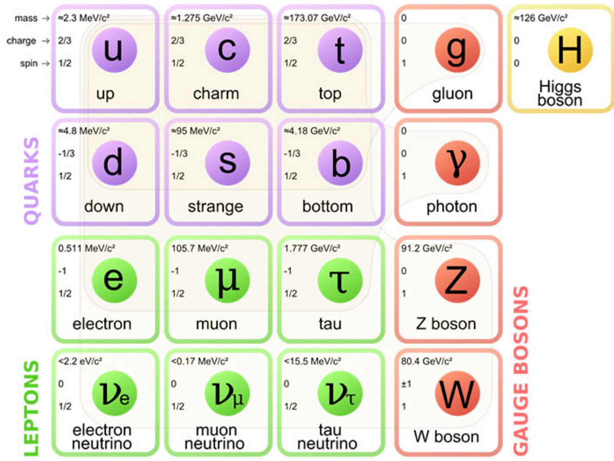

Figure 1.1: The Standard Model of particle physics: leptons, quarks, gauge and Higgs boson, together with their charge, mass and spin.

relevance to particle physics is described by a Quantum Field Theory (QFT) corresponding to the exchange of a mediator, a spin-1 force-carrying particle known as a gauge boson. The photon is the gauge boson of Quantum Electrodynamics (QED), the QFT of electromagnetic interaction; the gluon is the gauge boson of Quantum Chromodynamics (QCD), the QFT of strong interaction. The gluon and the photon are massless. The weak charged-current interaction is mediated by the charged W^+ and W^- bosons; there is also a weak neutral-current interaction, closely related to the charged current, which is mediated by the electrically neutral Z boson. The gauge bosons of weak interactions are massive. The final element of the SM is the Higgs boson, which was discovered by the CMS [1] and ATLAS [2] experiments at the Large Hadron Collider (LHC) in 2012. It is a massive spin-0 scalar particle, and it provides the mechanism by which all other particles acquire mass. The process of interaction by boson exchange can be described by means of the Feynman diagrams. The left-hand side of the diagram represents the initial state, and the right-hand side represents the final state (time flows from the left to the right). The central part of the diagram shows the particles exchanged and the SM vertices involved in the interaction: each vertex is characterized by a coupling constant which determines the interaction strength, and energy and momentum are conserved. Figure 1.2 shows the Feynman diagram for the scattering process

$a + b \to c + d$ through the exchange of another particle X.

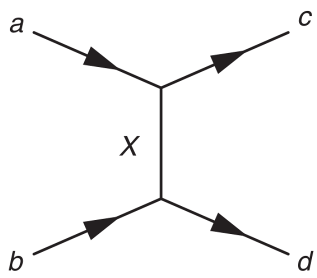

Figure 1.2: The Feynman diagram for the $a + b \to c + d$ scattering

1.2 The local gauge invariance principle

The SM is a gauge theory, which means that the Lagrangian is invariant under certain groups of local transformations. In particular, the gauge group of the SM is $SU(3)_C \times SU(2)_L \times U(1)_Y$, as described in the following sections. The concept of local gauge invariance can be introduced using a simple example, starting from the U(1) symmetry of electromagnetism [3]. Consider the Lagrangian for a free fermion field ψ with mass m, which has a global U(1) symmetry such that

$$\mathcal{L}_0 = i\overline{\psi}(\gamma^\mu \partial_\mu - m)\psi$$

is invariant under the U(1) global phase transformation $\psi \to \psi'(x) = \psi(x)e^{i\alpha}$, where α is an arbitrary real number. Suppose now to require an U(1) local phase transformation such that α depends on the space-time coordinate, $\alpha \to \alpha(x)$. In order to preserve the invariance of $\mathcal{L}_0$, the derivative ∂_μ should be replaced by the covariant derivative D_μ

$$\partial_\mu \to D_\mu = \partial_\mu + iqA_\mu$$

provided that the new field A_μ transforms as

$$A_\mu \to A'_\mu = A_\mu - \partial_\mu \alpha.$$

Hence the gauge-invariant Lagrangian of QED can be written as

$$\mathcal{L}_0 = i\overline{\psi}(\gamma^\mu \partial_\mu - m_e)\psi + e\overline{\psi}\partial^\mu A_\mu \psi - \frac{1}{4}F_{\mu\nu}F^{\mu\nu}.$$

The kinetic term $F_{\mu\nu}F^{\mu\nu} = (\partial_\mu A_\nu - \partial_\nu A_\mu)(\partial^\nu A^\mu - \partial^\mu A^\nu)$ is already invariant under U(1) local gauge transformation. The term containing A_μ, the same that would be introduced using minimal substitution, describes the interaction of the fermions with a new gauge field which can be identified as the photon. Therefore, QED four-vector current $j^\mu = \overline{\psi}\gamma^\mu\psi$ becomes

$$j^\mu = \overline{u}(p')\gamma^\mu u(p)$$

where u and $\overline{u}$ are the Dirac spinor and its adjoint (depending on fermions four-momentum p and p') and the γ^{μ}'s are the four Dirac matrices. All of QED, including Maxwell's equations, can be derived by requiring the invariance of the Lagrangian under U(1) transformation.

1.3 The Electroweak Interaction

1.3.1 The weak interaction: charged current

The weak interaction is obtained by extending the local gauge principle to require that the Lagrangian is invariant under SU(2) local phase transformations [3]

$$\psi \to \psi' = \psi \exp\left(i g_W \boldsymbol{\alpha}(x) \cdot \mathbf{T}\right)$$

where the $T_i = \frac{1}{2}\sigma_i$ with $i \in [1, 2, 3]$ are the three Pauli matrices corresponding to the three generators of SU(2), g_W is the weak coupling constant and $\boldsymbol{\alpha}(x)$ are three functions that specify the local phase at each point in space-time. Since the Pauli matrices do not commute and $\left[\sigma_i, \sigma_j\right] = 2i\epsilon^{ijk}\sigma_k$, the SU(2) group is termed non-Abelian. The covariant derivative therefore becomes

$$\partial_\mu \to D_\mu = \partial_\mu + i g_W \mathbf{T} \cdot \mathbf{W}_\mu$$

where $\mathbf{W}(x)$ are the three new gauge fields, corresponding to three gauge bosons $W^{(1)}$, $W^{(2)}$, $W^{(3)}$. From observations of parity violations in weak interaction, the corresponding four-vector current is required have a different form with respect to QED. It can be written as a linear combination of vector and axial vector currents,

$$j^\mu = \overline{u}(p')\gamma^\mu u(p) + \overline{u}(p')\gamma^\mu\gamma^5 u(p) = g_V j_V^\mu + g_A j_A^\mu$$

where g_V and g_A are the vector and the axial vector coupling constants. The relative strength of the parity violation in weak interactions is given by:

$$\frac{g_V g_A}{g_V^2 + g_A^2}$$

If either g_V or g_A is zero, parity is conserved in the interaction. Furthermore, maximal parity violation occurs when $|g_V| = |g_A|$, corresponding to a pure V-A or V+A interaction. From experiment, it is known that the weak charged current due to the exchange of a $W^{\pm}$ bosons has the form a vector minus axial vector (V-A) interaction. Any spinor can be decomposed into left-handed and right-handed components, through the left- and right-handed projection operators

$$P_R = \frac{1}{2}(1 + \gamma^5) \qquad P_L = \frac{1}{2}(1 - \gamma^5).$$

As a consequence of the V-A interaction, only left-handed (LH) particle states or right-handed (RH) antiparticle states participate in the charged-current weak interaction, because the current term for RH particle states or LH antiparticle states is zero. For this reason, the symmetry group of the weak interaction is referred to as $SU(2)_L$. Since the generators of the SU(2) gauge transformation are the 2×2 Pauli spin-matrices, ψ must be written in terms of two components. In analogy with the definition of isospin, ψ is termed a weak isospin doublet, and it must contains particle states differing by one unit of electric charge, for example

$$\psi(x) = \begin{pmatrix} \nu_e \\ e^- \end{pmatrix}.$$

The total weak isospin I_W is 1/2, while the weak isospin 3-component is 1/2 for the neutrino ν_e and -1/2 for the electron e^-. RH particle and LH antiparticle states are placed in weak isospin singlets with $I_W = 0$. They are therefore unaffected by the $SU(2)_L$ local gauge transformation and they do not couple to the gauge bosons of the symmetry. The requirement of local gauge invariance implies the modification of the Lagrangian to include a new interaction term:

$$ig_W T_k \gamma^\mu W^k_\mu \psi_L = \frac{i}{2} g_W \sigma_k \gamma^\mu W^k_\mu \psi_L$$

which gives rise to the three weak currents, one for each of the Pauli spin-matrices

$$j^1_\mu = \frac{g_W}{2}\overline{\psi}_L \gamma^\mu \sigma_1 \psi_L, \qquad j^2_\mu = \frac{g_W}{2}\overline{\psi}_L \gamma^\mu \sigma_2 \psi_L, \qquad j^3_\mu = \frac{g_W}{2}\overline{\psi}_L \gamma^\mu \sigma_3 \psi_L,$$

where ψ_L represents the weak isospin doublet of LH particles. The four-vector currents corresponding to the exchange of the physical $W^\pm$ bosons are

$$j^\pm_\mu = \frac{1}{\sqrt{2}}(j^1_\mu \pm i j^2_\mu) = \frac{g_W}{2\sqrt{2}}\overline{\psi}_L \gamma^\mu (\sigma_1 \pm i\sigma_2)\psi_L = \frac{g_W}{\sqrt{2}}\overline{\psi}_L \gamma^\mu \sigma_\pm \psi_L.$$

The physical W bosons can be identified as:

$$W^\pm_\mu = \frac{1}{\sqrt{2}}\left(W^1_\mu + iW^2_\mu\right).$$

Therefore, the Lagrangian of weak, charged interaction becomes:

$$\mathcal{L}_{CC} = -\frac{g_W}{2\sqrt{2}}\sum_i \overline{\psi}_i \gamma^\mu \left(1-\gamma^5\right)\left(T^+ W^+_\mu + T^- W^-_\mu\right)\psi_i$$

where the sum is over the three fermion generations, ψ_i is a $SU(2)_L$ doublet and $T^\pm = \frac{1}{2}\left(T^1 \pm T^2\right)$ are the projector operators. The original description of the weak interaction, due to Fermi [4], was formulated as an attempt of explaining the β emission, before the discovery of the parity violation, and it was expressed in terms of a contact interaction. The strength of the weak interaction was given by the Fermi constant G_F, related to the g_W constant as:

$$\frac{G_F}{\sqrt{2}} = \frac{g_W^2}{8m_W^2}.$$

From the observed decay rates of muons and tau leptons it is found that the strength of the weak interaction is the same for all lepton flavours, i.e. $G_F^{(e)} = G_F^{(\mu)} = G_F^{(\tau)}$ (lepton universality). On the other hand, the strength of the weak interaction for quarks, which can be determined from the study of nuclear β-decay, is not the same for all quark flavours. Such differences arise considering that the weak eigenstates of quarks do not coincide with the mass eigenstates, but are related to them by the unitary Cabibbo-Kobayashi–Maskawa (CKM) matrix V_{CKM} [5; 6]:

$$\begin{pmatrix} d' \\ s' \\ b' \end{pmatrix} = V_{CKM} \begin{pmatrix} d \\ s \\ b \end{pmatrix} = \begin{pmatrix} V_{ud} & V_{us} & V_{ub} \\ V_{cd} & V_{cs} & V_{cb} \\ V_{td} & V_{ts} & V_{tb} \end{pmatrix} \begin{pmatrix} d \\ s \\ b \end{pmatrix}$$

The relative strength of the interaction is therefore defined by the relevant element of the CKM matrix. The CKM matrix has four independent parameters, three rotation angles and a complex phase:

$$V_{CKM} = \begin{pmatrix} c_{12}c_{13} & s_{12}c_{13} & s_{13}e^{-i\delta} \\ -s_{12}c_{23} - c_{12}s_{23}s_{13}e^{i\delta} & c_{12}c_{23} - s_{12}s_{23}s_{13}e^{i\delta} & s_{23}c_{13} \\ s_{12}s_{23} - c_{12}c_{23}s_{13}e^{i\delta} & -c_{12}s_{23} - s_{12}c_{23}s_{13}e^{i\delta} & c_{23}c_{13} \end{pmatrix}$$

where c_{ij} stands for $\cos\theta_{ij}$, and s_{ij} for $\sin\theta_{ij}$. The values of these parameters are not predicted by SM, and they have to be evaluated from experiments [7].

1.3.2 The neutral current and the electroweak unification

The $SU(2)_L$ symmetry of the weak interaction implies the existence of a weak, neutral current:

$$j_\mu^3 = \frac{g_W}{2}\overline{\psi}_L\gamma^\mu\sigma_3\psi_L.$$

It can seem reasonable to identify the boson for the neutral current as W^3. However, in that way, it would couple only to LH particles (and RH antiparticles) while from experiments has been observed that also RH particles (and LH antiparticles) can interact via neutral current through the exchange of the physical Z boson. Of the four observed bosons of QED and the weak interaction, the photon and the Z boson, with the corresponding fields A_μ and Z_μ, are both neutral. Consequently, it is plausible that they can be expressed in terms of two neutral bosons, one of which is the W^3 associated with the $SU(2)_L$ local gauge symmetry. In the 1960s Glashow [8], Salam [9] and Weinberg [10] (GSW) proposed a model that was capable of unify the electromagnetism and the weak interaction in a single electroweak interaction. The GSW model was based on the Yang-Mills theory [11], a non abelian SU(N) gauge theory which describes the interaction with the gauge fields via the local gauge principle, and allows to write the gauge field lagrangian as

$$\mathcal{L}_{gf} = -\frac{1}{4} F^{a\mu\nu} F^{a}_{\mu\nu}$$

where a is the index of the generators of the corresponding Lie algebra, and the strenght field tensor $F^{\mu\nu} = \partial^{\mu} A^{\nu} - \partial^{\nu} A^{\mu} - ig\left[A_{\mu}, A_{\nu}\right]$, where A_{μ} is the gauge field. In the GSW model the U(1) gauge symmetry of electromagnetism is replaced with a new $U(1)_Y$ local gauge symmetry

$$\psi(x) \to \psi'(x) = \exp\left(ig' \frac{Y}{2} \zeta(x)\right) \psi(x)$$

giving rise to a new interaction term, in order to preserve local gauge invariance

$$g' \frac{Y}{2} B_{\mu} \gamma^{\mu} \psi.$$

The new gauge field B_{μ} couples to a new kind of charge, termed weak hypercharge Y. In the unified electroweak model, the photon and Z boson are written as linear combinations of B_{μ} and W^3

$$A_{\mu} = B_{\mu} \cos\theta_W + W^3_{\mu} \sin\theta_W$$

$$Z_{\mu} = -B_{\mu} \sin\theta_W + W^3_{\mu} \cos\theta_W$$

where θ_W is termed the weak mixing angle. Therefore, the physical currents of QED and the weak neutral current are:

$$j^{em}_{\mu} = j^{Y}_{\mu} \cos\theta_W + j^{3}_{\mu} \sin\theta_W$$

$$j^{Z}_{\mu} = -j^{Y}_{\mu} \sin\theta_W + j^{3}_{\mu} \cos\theta_W$$

and the Lagrangian of weak, neutral current becomes

$$\mathcal{L}_{NC} = -\frac{g_W}{2\cos\theta_W} \sum_i \overline{\psi}_i \gamma^{\mu} (g^i_V - g^i_A \gamma^5) \psi_i Z^{\mu}$$

where ψ_i can be RH or LH fermionic singlets, and g^i_V and g^i_A are expressed as

$$g^i_V = T^i_3 - 2Q^i \sin^2\theta_W \qquad\qquad g^i_A = T^i_3.$$

The GSW model of electroweak unification then implies that the couplings of the weak and electromagnetic interactions are related

$$e = g_W \sin\theta_W = g' \cos\theta_W.$$

The mixing angle θ_W has been measured in different ways, and the average of the measurements of $\sin^2\theta_W$ gives [12]

$$\sin^2\theta_W = 0.23146 \pm 0.00012.$$

Furthermore, from invariance under $U(1)_Y$ and $SU(2)_L$ local gauge transformations, considering the interactions of the electron and the electron neutrino it can be obtained

$$Y = 2(Q - I_W^3).$$

The electroweak Lagrangian can be then written in a compact way as

$$\mathcal{L}_{EW} = \overline{\chi}_L \gamma^\mu \left(i\partial_\mu - g_W \mathbf{T}\cdot\mathbf{W} - g'\frac{Y}{2}B_\mu \right)\chi_L + \overline{\psi}_R \left(i\partial_\mu - g'\frac{Y}{2}B_\mu \right)\psi_R + \mathcal{L}_{KIN}$$

where χ_L and ψ_R are the fermionic left-handed and right-handed states respectively [13]. The term $\mathcal{L}_{KIN}$ describes the gauge field kinetics

$$\mathcal{L}_{KIN} = -\frac{1}{4}B_{\mu\nu}B^{\mu\nu} - \frac{1}{4}\mathbf{W}_{\mu\nu}\mathbf{W}^{\mu\nu}$$

where

$$B_{\mu\nu} = \partial_\mu B_\nu - \partial_\nu B_\mu \qquad \text{and} \qquad \mathbf{W}_{\mu\nu} = \partial_\mu \mathbf{W}_\nu - \partial_\nu \mathbf{W}_\mu + g_W \mathbf{W}_\mu \times \mathbf{W}_\nu.$$

The last term in $\mathbf{W}_{\mu\nu}$ is due to the non-Abelian structure of $SU(2)_L$.

1.3.3 Triple and quartic gauge couplings

The kinetic term of the electroweak Lagrangian gives rise to triple and quartic self-interactions among the gauge fields, whose strength is given by the same $SU(2)_L$ constant coupling g_W. The explicit Lagrangian for the triple gauge couplings is [13]

$$\begin{aligned}\mathcal{L}_3 = &- ie\cot\theta_W\{(\partial^\mu W^\nu - \partial_\mu W_\nu)W_\mu^\dagger Z_\nu - (\partial^\mu W^{\nu\dagger} - \partial_\mu W_{\nu^\dagger})W_\mu W_\nu + W_\mu W_\nu^\dagger(\partial^\mu Z^\nu - \partial_\mu Z_\nu)\}\\ &- ie\{(\partial^\mu W^\nu - \partial_\mu W_\nu)W_\mu^\dagger A_\nu - (\partial^\mu W^{\nu\dagger} - \partial_\mu W_{\nu^\dagger})W_\mu A_\nu + W_\mu W_\nu^\dagger(\partial^\mu A^\nu - \partial_\mu A_\nu)\}\end{aligned}$$

while for the quartic gauge couplings [13]

$$\begin{aligned}\mathcal{L}_4 = &- \frac{e^2}{2\sin^2\theta_W}\{(W_\mu^\dagger W^\mu)^2 - W_{\mu^\dagger}W^{\mu\dagger}W_\nu W^\nu\} - e^2\cot^2\theta_W\{W_\mu^\dagger W^\mu Z_\nu Z^\nu - W_{\mu^\dagger}Z^\mu W_\nu Z^\nu\}\\ &- e^2\cot\theta_W\{2W_\mu^\dagger W^\mu Z_\nu A^\nu - W_\mu Z^\mu W_\nu A^\nu - W_\mu A^\mu W_\nu Z^\nu\}\\ &- e^2\{W_{\mu^\dagger}W^\mu A_\nu A^\nu - W_{\mu^\dagger}A^\mu W_\nu A^\nu\}\end{aligned}$$

In each coupling there are always at least a pair of charged W bosons. The $SU(2)_L$ algebra does not generate any neutral coupling involving only photons or Z bosons, in order to preserve the gauge invariance. The Feynman diagrams for triple and quartic SM gauge couplings are shown in Figure 1.3.

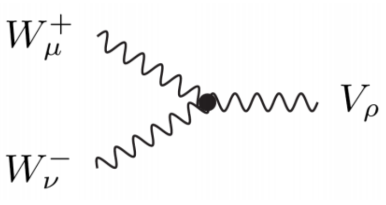

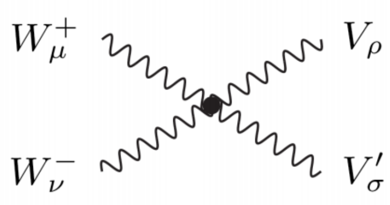

Figure 1.3: Feynman diagrams for triple (left) and quartic (right) gauge couplings. In the triple vertices V_ρ = Z, in the quartic vertices γ and $V_{\rho'}, V_{\sigma'}$ = (W,W), (Z,Z), (Z,γ), (γ,γ).

1.4 The Strong interaction

Quantum Chromodynamics is the QFT of strong interaction and, as for QED and weak interactions, it requires that the Lagrangian is invariant under SU(3) local phase transformation

$$\psi(x) \to \psi'(x) = \exp\left[ig_S\boldsymbol{\beta}(x)\cdot\hat{\mathbf{T}}\right]\psi(x)$$

where $\hat{\mathbf{T}} = \{T^a\}$ represent the eight SU(3) group generators, which are related to the Gellmann matrices λ^a as $T^a = \frac{1}{2}\lambda^a$, and g_S represents the coupling constant. In order to preserve the SU(3) local gauge symmetry the derivatives have to be replaced with the covariant derivative

$$D_\mu^{ij} = \partial_\mu\delta^{ij} + ig_S(T^a)^{ij}G_\mu^a$$

where the G_μ^a are the new fields corresponding to the eight gluons with colour index a and $a \in [1, ..., 8]$. The SU(3) generators do not commute, and $[\lambda_i, \lambda_j] = 2if_{ijk}\lambda_k$. The SU(3) symmetry group is therefore termed non-Abelian and it gives rise to gluon-self interactions and *asymptotic freedom*, discussed below. The theory of QCD appears to be very similar to that of QED. The QED interaction is mediated by a massless photon, the generator of U(1) symmetry, and QCD is mediated by eight massless gluons, corresponding to the eight generators of SU(3). Since the SU(3) generators are 3×3 matrices, ψ must be written including a new three-terms component. This new degree of freedom is termed *colour*, with *red*, *blue* and *green* labelling the three colour wavefunctions

$$r = \begin{pmatrix}1\\0\\0\end{pmatrix} \qquad g = \begin{pmatrix}0\\1\\0\end{pmatrix} \qquad b = \begin{pmatrix}0\\0\\1\end{pmatrix}.$$

The single charge of QED is replaced by three colour charges, *r*, *g* and *b*. In order to conserve the colour at the interaction vertex the gluons must carry colour charge. The colour assignments of each of them can be written

$$r\bar{g},\ g\bar{r},\ r\bar{b},\ b\bar{r}, g\bar{b},\ b\bar{g},\ \frac{1}{2}(r\bar{r} - g\bar{g}) \quad \text{and} \quad \frac{1}{6}(r\bar{r} + g\bar{g} - 2b\bar{b})$$

Only particles that have non-zero colour charge couple to gluon: leptons, which are color neutral, do not feel the strong force. The current term for QCD can be written in analogy with QED

$$j^\mu = \overline{\psi}_j \left(\frac{1}{2} i g_S \lambda^a \gamma^\mu\right) \psi_i,$$

where ψ_i represents a triplet under SU(3) and j is the index colour. The Lagrangian for QCD is therefore

$$\mathcal{L}_{QCD} = \psi_i \left((i\gamma^\mu D_\mu)_{ij} - m\delta_{ij}\right)\psi_j - \frac{1}{4}\widetilde{F}^a_{\mu\nu}\widetilde{F}^{\mu\nu}_a$$

where the last term is the kinetic term, with $\widetilde{F}^a_{\mu\nu} = \partial_\mu G_\nu - \partial_\nu G_\mu + g_S f^{abc} G^b_\mu G^c_\nu$.

1.4.1 Colour confinement and hadronization

Unlike leptons, quarks can not be seen directly. Their non-observation is explained by the hypothesis of colour confinement, which states that objects with colour charge can not propagate as free particles. In spite of its importance in the understanding of QCD processes, the mechanism of colour confinement has not been analytically proved yet. It is believed to originate from the gluon−gluon self-interactions that arise because the gluons carry colour charge and they can interact with other gluons. Considering two free quarks that are pulled apart: the mutual exchange of gluons between them squeeze the colour field into a tube (Figure 1.4) and, as a consequence, the energy stored in the field becomes proportional to the distance between the quarks. It would therefore require an infinity amount of energy to separate them to infinity and so quarks can only exist in colourless hadrons. Furthermore, since also gluons carry colour charge, they can not propagate over macroscopic distances, and they are confined to colourless object. In particle collisions, quarks and gluons are observed as *jet* of colourless particles. A qualitative description of the hadronization process is reported in Figure 1.5. The quark and antiquark produced in an interaction separates at high velocities, restricting the colour field in a tube, consequently to colour confinement; the energy stored in the field increases as the quarks separate further, until it becomes sufficient to produce a new $q\bar{q}$ pair, breaking the colour field in smaller tubes. The process continues until the energy of quarks is sufficiently low to combine and form colourless hadrons. Two jets result from the initial $q\bar{q}$ pair, following the initial directions of the quark and the antiquark respectively.

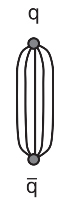

Figure 1.4: Qualitative picture of the colour field between a $q\bar{q}$ pair.

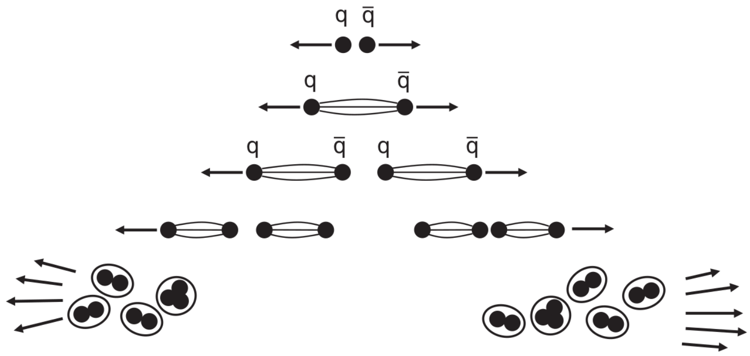

Figure 1.5: A qualitative description of the hadronization process.

1.4.2 Asymptotic freedom and the running of α_S

To understand qualitatively the concept of asymptotic freedom, one can make a comparison with the case of QED. Due to vacuum polarization, pairs of particle-antiparticle are created around a test charge q_c. The particles of charge opposite to q_c will tend to be closer to the test charge, analogously to the electric charge screening in a dielectric medium. In both cases, by Gauss' law, the total charge inside a sphere of radius r is smaller than q_C and, the larger r, the more the total charge will tend to the test charge value q_C. The potential determined by the screening is:

$$V(r) \propto q_C \frac{e^{-r}}{r}.$$

Therefore, the magnitude of the running coupling in QED will decrease at larger distances, tending to its macroscopic value $\alpha(0) \simeq 1/137$, and get stronger at small distances. For QCD the situation is different because gluons carry color charge. Since the $SU(3)_C$ group is non-Abelian, the Gauss' law has to include an additional term containing f_{abc}, where a, b and c are the colour indices. This new term determines the anti-screening, that enhance the field at large distances. As a consequence of the anti-screening the QCD coupling constant tends to decrease with small distance and to increase at large distance. Formally, the running of a coupling originates from the renormalization procedure. The strong coupling constant can be rewritten as

$$\alpha_S = \frac{g_S}{4\pi}.$$

Its value depends on the energy scale of the interaction Q and on a renormalization factor μ_R which is introduced to eliminate the divergences that arise in QCD calculations. The scale dependence of the strong coupling is controlled by the β-function [14]

$$Q^2 \frac{\partial \alpha_S}{\partial Q^2} = \beta(\alpha_S) = -\left(\frac{\alpha_s}{4\pi}\right)^2 = \sum_{n=0} \left(\frac{\alpha_s}{4\pi}\right)^n \beta^n$$

where the β_n depend on the quark and gluon loops and on the renormalization scheme used. The exact analytical solution for α_S is known only to β_0 order. At this order

$$\alpha_S(Q^2) = \frac{\alpha_S(\mu_R^2)}{1 + \beta_0 \ln(Q^2/\mu_R^2)\alpha_S(\mu_R^2)}.$$

This equation relates the strength of the coupling at a scale Q to the one at scale μ_R, assuming both scales to be in the perturbative regime. The value of α_S is currently extrapolated at the value of the Z mass, at which it is sufficiently small to the perturbation theory to be applied and its value is $\alpha_S(m_Z^2) = 0.1181 \pm 0.0011$ [12]. When the coupling approaches unity, perturbation theory is not valid anymore and the QCD scale parameter Λ_{QCD} is introduced as the scale at which $\alpha_S(Q^2)$ diverges [14]

$$\alpha_S(Q^2) = \frac{4\pi}{\beta_0 \ln(Q^2/\Lambda_{QCD})}.$$

At value of $\Lambda_{QCD} \sim 200$ MeV (the *Landau pole*), the strong coupling becomes infinite, perturbation theory can not be applied anymore and quarks and gluons combine into hadrons.

1.5 The Higgs boson

1.5.1 The Spontaneous Simmetry Breaking

The required local gauge invariance of SM is broken by the terms in the Lagrangian corresponding to bosons masses. For example, if the photon was massive, the QED Lagrangian would contain an additional term $\frac{1}{2}m_\gamma^2 A_\mu A^\mu$ and, considering a U(1) local gauge transformation, the photon field would transform as

$$A_\mu \to A'_\mu = A_\mu - \partial_\mu \alpha.$$

Therefore, the mass term would become

$$\frac{1}{2}m_\gamma^2 A_\mu A^\mu \to \frac{1}{2}m_\gamma^2(A_\mu - \partial_\mu\alpha)(A^\mu - \partial^\mu\alpha) \neq \frac{1}{2}m_\gamma^2 A_\mu A^\mu$$

breaking the local gauge U(1) invariance. This is not a problem for QED and QCD, where the gauge bosons are massless, but it is conflicting with the observation of the large masses of W and Z bosons [15; 16]. The same problem arises in the case of fermion masses: in the gauge transformation of the weak interaction the left-handed particles transform as weak isospin doublets and the right-handed particles as singlets, which implies that the fermion mass term in the SM Lagrangian should be written as

$$m_f(\overline{\psi}_L\psi_R + \overline{\psi}_R\psi_L)$$

breaking the required $SU(2)_L$ gauge invariance. In order to preserve the correct properties of the SM Lagrangian, in the 1960s, Higgs, Englert and Brout [17; 18] introduced the idea of the spontaneous symmetry breaking (SSB), a mechanism that brings in the Lagrangian the mass term for a scalar field as a consequence of a broken symmetry. As an example, consider a complex scalar field

$$\phi = \frac{1}{2}(\phi_1 + i\phi_2)$$

whose Lagrangian

$$\mathcal{L} = \frac{1}{2}(\partial_\mu \phi)^*(\partial^\mu \phi) - V(\phi) \quad \text{with} \quad V(\phi) = \mu^2(\phi^* \phi) + \lambda(\phi^* \phi)^2 \tag{1.1}$$

is invariant under U(1) global symmetry transformation. The potential has a finite minimum if $\lambda > 0$. Its shape depends on the sign of μ^2, as shown in Figure 1.6. If $\mu^2 > 0$, the potential minimum occurs when both ϕ_1 and ϕ_2 are zero; if $\mu^2 < 0$, the potential has an infinite set of minima defined by:

$$\phi^\dagger \phi = \frac{1}{2}(\phi_1^2 + \phi_2^2) = \frac{-\mu^2}{\lambda} = v^2.$$

Without loss of generality, the physical vacuum state can be chosen to be any

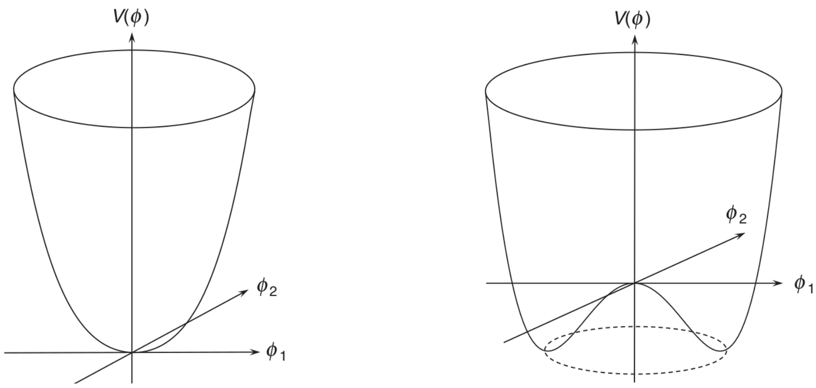

Figure 1.6: The V(ϕ) potential for (left) $\mu^2 > 0$ and (right) $\mu^2 < 0$

minimum of such set, breaking the global symmetry of the Lagrangian. Choosing the vacuum state in the real direction, $(\phi_1, \phi_2) = (v, 0)$ and expanding the field around it by writing $\phi_1(x) = \eta(x) + v$ and $\phi_2(x) = \xi(x)$, one obtains

$$\phi = \frac{1}{2}(\eta + v + i\xi).$$

The Lagrangian can be therefore written in term of the fields η and ξ, exploiting the relation $\mu^2 = -\lambda v^2$. The term which is quadratic in the field η can be identified as the mass terms, while the terms with three or four powers of the fields are interaction terms. Thus, the Lagrangian becomes

$$\mathcal{L} = \frac{1}{2}(\partial_\mu \eta)(\partial^\mu \eta) - \frac{1}{2}m_\eta^2 \eta^2 + \frac{1}{2}(\partial_\mu \xi)(\partial^\mu \xi) - V_{int}(\eta, \xi)$$

and it represents a scalar field η with mass $m_\eta = \sqrt{2\lambda v^2}$ and a massless scalar field, whose associated massless scalar particle is known as a Goldstone boson [19].

1.5.2 The Brout-Englert-Higgs mechanism

The W^+, W^- and Z masses are included in the SM lagrangian integrating the SSB with the local $SU(2)_L \times U(1)_Y$ gauge symmetry, and giving rise to the so-called Brout-Englert-Higgs (BEH) mechanism. Consider first the simpler example of the U(1) symmetry. The Lagrangian for a complex scalar field is not invariant under U(1) local gauge transformation $\phi \to \phi'(x) = \exp(ig\alpha(x)) \cdot \phi(x)$, therefore the derivatives have to be replaced by the covariant derivatives $\partial_\mu \to D_\mu = \partial_\mu + igB_\mu$, where the new gauge field B_μ transforms as $B_\mu \to B'_\mu = B_\mu - \partial_\mu \alpha(x)$. The combined Lagrangian for the complex scalar field ϕ, the gauge field B and the potential $V(\phi) = \mu^2\phi^2 - \lambda\phi^4$ is

$$\mathcal{L} = -\frac{1}{4}F^{\mu\nu}F^{\mu\nu} + (D_\mu\phi)^*(D_\mu\phi) - \mu^2\phi^2 - \lambda\phi^4.$$

As before, the choice of the physical vacuum state spontaneously breaks the symmetry: choosing $\phi_1 + i\phi_2 = v$, and expanding about such vacuum state, the following Lagrangian is obtained

$$\mathcal{L} = \frac{1}{2}(\partial_\mu\eta)(\partial^\mu\eta) - \lambda v^2\eta^2 + \frac{1}{2}(\partial_\mu\xi)(\partial^\mu\xi) - \frac{1}{4}F^{\mu\nu}F^{\mu\nu} + \frac{1}{2}g^2v^2B_\mu B^\mu - V_{int}(\eta,\xi) + gvB_\mu(\partial^\mu\xi).$$

The SSB produces, as before, a massive scalar field η and a massless Goldstone boson ξ. In addition, due to the requirement of local gauge invariance, the previously massless gauge field B acquires a mass term $\frac{1}{2}g^2v^2B_\mu B^\mu$: the aim of giving mass to the gauge boson is therefore achieved. However, the last term in the Lagrangian represent a direct coupling between the Goldstone field ξ and the gauge field B which would lead to the transformation of the spin-1 gauge field into a spin-0 scalar field. The Goldstone field can be eliminated from the Lagrangian by making the following gauge transformation

$$B_{\mu(x)} \to B'_\mu(x) = B_\mu(x) + \frac{1}{gv}\partial_\mu\xi(x)$$

which corresponds to taking $\alpha(x) = -\xi(x)/gv$, such that $\phi(x) \to \phi'(x) = \exp(-i\frac{\xi(x)}{v}) \cdot \phi(x)$. As a consequence the complex scalar field $\phi(x)$, after the expansion about the vacuum state, appears to be entirely real

$$\phi(x) = \frac{1}{\sqrt{2}}(v + \eta(x)) \equiv \frac{1}{\sqrt{2}}(v + h(x))$$

where the field $\eta(x)$ has been written as the "Higgs field" $h(x)$ to emphasize that this is the physical field in this gauge, called the *Unitary gauge.* After cancelling the Goldstone field, the Lagrangian can be rewritten (ignoring constant terms) as

$$\mathcal{L} = \frac{1}{2}(\partial_\mu h)(\partial^\mu h) - \lambda v^2 h^2 - \frac{1}{4}F_{\mu\nu}F^{\mu\nu} + \frac{1}{2}g^2 v^2 B_\mu B^\mu + \\ + g^2 v B_\mu B^\mu h + \frac{1}{2}g^2 B_\mu B^\mu h^2 - \lambda v h^3 - \frac{1}{4}\lambda h^4.$$

It describes a massive scalar Higgs field h and a massive gauge boson B, associated with the U(1) local gauge symmetry. It contains interaction terms between the Higgs boson and the gauge boson, and Higgs boson self-interaction terms. The mass of the gauge boson is $m_B = gv$, while the mass of the Higgs boson is $m_H = \sqrt{2\lambda}v$.

Consider now the $SU(2)_L \times U(1)_Y$ gauge symmetry. The simplest Higgs model consists of two complex scalar fields which constitute a weak isospin doublet. In order to generate the masses of the electroweak bosons, one of the scalar fields must be neutral, written as ϕ^0, and the other must be charged such that ϕ^+ and $(\phi^+)^* = \phi^-$ give the longitudinal degrees of freedom of the W^+ and W^-:

$$\phi = \begin{pmatrix} \phi^+ \\ \phi^0 \end{pmatrix} = \frac{1}{\sqrt{2}} \begin{pmatrix} \phi_1 + i\phi_2 \\ \phi_3 + i\phi_4 \end{pmatrix}.$$

The Lagrangian for the Higgs field and the associated Higgs potential, have the same form of 1.1 and it possesses a global $SU(2)_L \times U(1)_Y$ symmetry. Expanding the fields around the chosen minimum and writing the doublet in a unitary gauge, one obtains:

$$\phi(x) = \frac{1}{2}\begin{pmatrix} 0 \\ v + h(x) \end{pmatrix}.$$

In order to respect the $SU(2)_L \times U(1)_Y$ local gauge symmetry of the electroweak model, the derivatives have to be replaced with the appropriate covariant derivatives

$$\partial_\mu \to D_\mu = \partial\mu + ig_W \mathbf{T} \cdot \mathbf{W}_\mu + ig'\frac{Y}{2}B_\mu.$$

Its effect on the Higgs doublet ϕ is

$$D_\mu \phi = \frac{1}{2}\left[2\partial_\mu + \left(ig_W \sigma \cdot \mathbf{W}_\mu + ig' B_\mu\right)\right]\phi$$

The gauge bosons masses are determined by the terms in $(D_\mu\phi)^\dagger(D^\mu\phi)$ that are quadratic in the gauge boson fields (D_μ is a 2×2 matrix, and the identity matrix multiplying ∂_μ and B_μ terms is implicit in the expression)

$$(D_\mu\phi)^\dagger(D^\mu\phi) = \frac{1}{2}(\partial_\mu h)(\partial^\mu h) + \frac{1}{8}g_W^2(W_{1\mu} + iW_{2\mu})(W^{1\mu} + iW^{2\mu})(v+h)^2 + \\ + \frac{1}{8}(g_W W_\mu^3 - g' B_\mu)(g_W W^{3\mu} - g' B^\mu)(v+h)^2.$$

The mass terms for the W^1 and W^2 fields are $\frac{1}{2}m_W^2 W_\mu^1 W^{1\mu}$ and $\frac{1}{2}m_W^2 W_\mu^2 W^{2\mu}$, therefore the mass of the W boson is $m_W = \frac{1}{2}g_W v$. The mass terms for the W^3 and B fields instead can be written as

$$\frac{v^2}{8}\begin{pmatrix} W_\mu^3 & B_\mu \end{pmatrix}\begin{pmatrix} g_W^2 & -g_W g' \\ -g_w g' & g'^2 \end{pmatrix}\begin{pmatrix} W^{3\mu} \\ B^\mu \end{pmatrix} = \frac{v^2}{8}\begin{pmatrix} W_\mu^3 & B_\mu \end{pmatrix}\mathbf{M}\begin{pmatrix} W^{3\mu} \\ B^\mu \end{pmatrix}$$

where $\mathbf{M}$ is the non-diagonal mass matrix, which allows the mixing of the two fields. The physical boson fields (A_μ and Z_μ) correspond to the basis in which the mass matrix is diagonal, and their masses correspond to the eigenvalues of the mass matrix, hence

$$\frac{v^2}{8}\begin{pmatrix} A_\mu & Z_\mu \end{pmatrix}\begin{pmatrix} 0 & 0 \\ 0 & g_W^2 + g'^2 \end{pmatrix}\begin{pmatrix} A^\mu \\ Z^\mu \end{pmatrix} = \frac{1}{2}\begin{pmatrix} A_\mu & Z_\mu \end{pmatrix}\begin{pmatrix} m_A^2 & 0 \\ 0 & m_Z^2 \end{pmatrix}\begin{pmatrix} A^\mu \\ Z^\mu \end{pmatrix}$$

from which the masses of the photon and the Z boson are respectively

$$\begin{aligned} m_A &= 0, \\ m_Z &= \frac{1}{2}v\sqrt{g_w^2 + g'^2}. \end{aligned}$$

The mass of the Higgs boson m_H is obtained from the lagrangian term which is quadratic in h, hence $m_H = \sqrt{2\lambda v^2}$. The vacuum expectation value of the Higgs field is $v = 246$ GeV, while λ is a free parameter. Therefore, the Higgs mass is not predicted by theory. In order to obtain the fermion masses, the scalar Higgs field couples to fermions through the so-called Yukawa interaction. A left-handed doublet L, when combined with a scalar field ϕ and right-handed singlet R, $\overline{L}\phi R$, it is invariant under $SU(2)_L$ and $U(1)_Y$ gauge transformations, as is its Hermitian conjugate $(\overline{L}\phi R)^\dagger = \overline{R}\phi^\dagger L$. Hence, the mass term for all the Dirac fermions can be obtained from the Yukawa Lagrangian

$$L_Y = -\sum_{i,j=1}^{3}\left[y_{ij}^u u_{Ri}\phi_C Q_{Lj} + y_{ij}^d \overline{d}_{Ri}\phi^\dagger Q_{Lj} + y_{ij}^e \overline{e}_{Ri}\phi^\dagger Q_{Lj}^e\right] + \text{hermitian conjugate.}$$

The sum is performed over the three generations of quarks and leptons, ϕ_C is the hermitian conjugate of the Higgs doublet ϕ and Q_{Lj} and Q_{Lj}^e are the left-handed doublets for quarks and leptons, respectively. The values $y^{u,d,e}$ correspond to the Yukawa coupling constants which are related with the fermion masses through the vacuum expectation value v.

1.5.3 Search for the Higgs boson

The Higgs boson was theorized for the first time in 1964, in order to include in the SM the particle masses, and the first attempts to demonstrate its existence and to constrain its mass started in the early 1970s [20]. One of the main problems in the search for the Higgs boson was in fact the unknown value of its mass. During 70s, theoretical studies on Higgs possible production and decay were published, however providing a very wide range for its mass, between 10 and 1000 GeV [21; 22]. The Large Electron-Positron collider (LEP), which operated at CERN from 1989 to 2000, was the first experiment to approach the energy necessary to its detection and, even though it was not able to make the discovery, it placed a significant limit on its mass, which was measured to be greater than 114 GeV [23]. Searches for the Higgs boson were provided also by the Tevatron collider [24]. With the beginning of the Large Hadron Collider operations, the mass range was further restricted and after the achievement of the 8 TeV at the center of mass it was expected that LHC would have finally excluded or confirmed the Higgs boson existance.

Production modes

The Higgs boson couples preferentially to the heavy particles (W, Z, top and bottom quarks and τ-leptons) and it can be produced in proton-proton collisions through a number of different processes [12]. The value of the associated cross section are shown in Figure 1.7. The *gluon-gluon fusion* processes ($\mathrm{gg} \rightarrow \mathrm{H} + \mathrm{X}$) are the dominant processes at the LHC, and the gluon coupling to the Higgs boson in the SM can be mediated by triangular top- and bottom-quark loops. The second important Higgs production channel is the *vector-boson fusion* ($qq \rightarrow qq\mathrm{H}$), whose cross section is about one order of magnitude smaller than the gluon-fusion one. The Higgs boson is here produced together with two forward jets coming from the break-up of the colliding protons, without the QCD radiation that instead accompany the gluon-fusion process, producing more easily identifiable final states. Other relevant production modes are the *Higgs strahlung* ($q\bar{q} \rightarrow \mathrm{WH}$ or $q\bar{q} \rightarrow \mathrm{ZH}$), which was the dominant channel at the LEP, where an electron and a positron collided to form a virtual Z boson, and the $\mathrm{t\bar{t}}$ associated production ($q\bar{q} \rightarrow \mathrm{t\bar{t}H}$). These last two processes have a cross section from one to two order of magnitude smaller than the gluon-fusion cross section. At LHC, at a center of mass of about 8 TeV, the total production cross section for a Higgs boson with a mass of 125 GeV was approximately 20 pb^{-1} [12].

Decay modes

The largest Higgs boson branching ratios are to the more massive particles, as listed in Table 1.1. The fermionic decay ($\mathrm{H} \rightarrow \mathrm{b\bar{b}}$ and $\mathrm{H} \rightarrow \tau^{-}\tau^{+}$) is the most promising channel for probing the coupling of the Higgs field to the quarks and leptons. Nevertheless, the presence of very large backgrounds makes the isolation

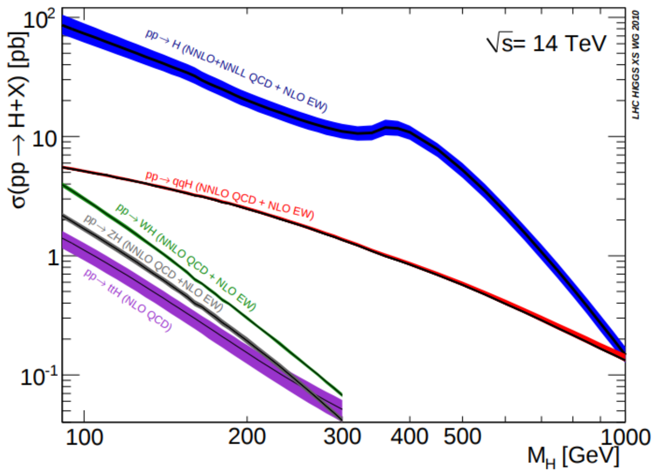

Figure 1.7: The SM Higgs production cross section at $\sqrt{s}$ = 14 TeV. From top to bottom: the gluon-gluon fusion (blue), the vector boson fusion (red), the associate production with a W/Z-boson (green/grey) and the $\mathrm{t\bar{t}}$ production (violet). Next-to-leading order and next-to-next-to leading order corrections have been also applied [25].

of a Higgs boson signal in these channels quite challenging [12]. The decays into massless bosons, as gluons or photons, needs to be mediated by W and heavy fermion loops. In the H $\rightarrow$ $\mathrm{W^+W^-}$, the W bosons can subsequently decay either into a quark and an antiquark or into a charged lepton and a corresponding neutrino. The decays into quarks are difficult to distinguish from the background, and the decays into leptons can not be fully reconstructed due to presence of neutrinos. A cleaner signal is given by the H $\rightarrow$ ZZ decay, with each Z boson decaying into a lepton-antilepton pair.

Decay channel	Branching ratio
$H \rightarrow \gamma\gamma$	2.27×10^{-3}
$H \rightarrow ZZ$	2.62×10^{-2}
$H \rightarrow W^+W^-$	2.14×10^{-1}
$H \rightarrow \tau^+\tau^-$	6.27×10^{-2}
$H \rightarrow b\bar{b}$	5.84×10^{-1}
$H \rightarrow Z\gamma$	1.53×10^{-3}
$H \rightarrow \mu^+\mu^-$	2.18×10^{-4}

Table 1.1: The predicted branching ratios of the Higgs boson for m_H=125 GeV [12].

The Higgs discovery

For a low-mass Higgs (between 110 and 150 GeV) the five final states that play an important role at the LHC are $\gamma\gamma$, ZZ^*, WW^*, $\tau^-\tau^+$ and $\mathrm{b\bar{b}}$. In particular, despite the low branching ratios, in the H $\rightarrow \gamma\gamma$ and H $\rightarrow \mathrm{ZZ}^* \rightarrow 4\ell$ all final state particles can be precisely measured and the reconstructed m_H resolution is excellent (1-2 GeV) [1]. For that reason, these two channel have been called the *golden* *channels*, and both ATLAS and CMS experiments relied on these to measure the Higgs boson mass. In the first case, the search was performed for a narrow peak over a smoothly falling background in the invariant mass distribution of two high p_T photons. An excess of events was found, with significance above 5σ, resulting in an estimate for the mass of the observed particle of $126.0 \pm 0.4\ (stat.) \pm\ 0.4(syst.)$ GeV [1]. In the second case, the search was performed for a narrow mass peak over a small continuous background dominated by non-resonant ZZ* production, deriving from quark-antiquark annihilation and gluon-gluon fusion processes [12]. An excess of events was found, with significance above 5σ, resulting in an estimate for the mass of the observed particle of $125.3 \pm 0.4\ (stat.) \pm\ 0.5(syst.)$ GeV [2]. In Figure 1.8, the distribution of the reconstructed invariant mass of the two photons in $\mathrm{H} \to \gamma\gamma$ events in the ATLAS detector is shown on the left, while on the right the distribution of the invariant masses of the four charged leptons in the CMS $\mathrm{H} \to \mathrm{ZZ}^* \to 4\ell$ search is shown. The combined mass measurements gave as a result [26]:

$$m_H = 125.09 \pm 0.21(stat.) \pm 0.11(syst.).$$

The discovery of the Higgs boson was announced by ATLAS and CMS on 4 July 2012 and, on 8 October 2013, the Nobel prize in physics was awarded jointly to Englert and Higgs “for the theoretical discovery of a mechanism that contributes to our understanding of the origin of mass of subatomic particles, and which recently was confirmed through the discovery of the predicted fundamental particle, by the ATLAS and CMS experiments at CERN’s Large Hadron Collider” [27].

1.6 Beyond the Standard Model

The existence of the Higgs boson is one of the most important confirmation of the validity of SM. The Higgs boson discovery has completed the theory as it was formulated in 1980s, and the experiments have further verified the efficacy of its predictions up to the electroweak scale. Precision evaluation of the SM parameters have been first performed at LEP and SLC (Stanford Linear Collider). For example, the value of top quark mass was extracted from analysis of other electroweak parameters. This indirect measurement resulted to be in great agreement with the direct one [28], providing a stringent prove of the SM accuracy. Precision tests have been also performed at the LHC, especially in the Higgs sector [29]. However, there are some physical phenomena that can not be fully explained by the SM, here briefly listed:

- **Dark matter and dark energy**. It is though that *dark matter* constitutes the 85% of matter in the Universe. Even though dark matter has never been directly observed yet, there are many evidence that support its existence. One of most important comes from the velocity distributions of stars as they

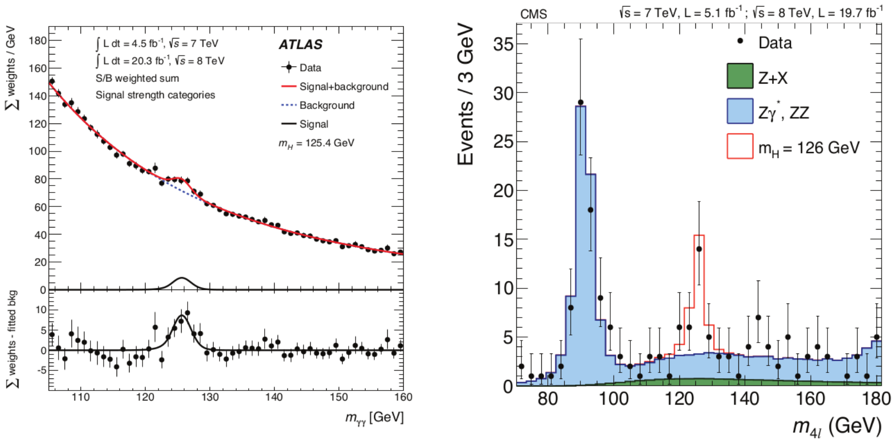

Figure 1.8: Left: the reconstructed invariant mass distribution of the diphotons candidates in the ATLAS experiment. The points represent the data, the dotted line represents the background, and the solid line the fit to the data of the sum of a signal component fixed to m_H = 126.5 GeV and of a background component. Right: the distribution of the reconstructed invariant masses of the four leptons candidates in the CMS experiment. The points represent the data, the filled histograms represent the background, and the open histogram shows the signal expectation for a Higgs boson of mass 125 GeV.

orbit around the galactic center. Assuming that most of the galaxy mass is concentrated in the central bulge, the tangential velocities of the stars should decrease as $M(r)/r$ but, instead, the galaxy rotation curve remains flat as the distance from the center increases, and the stars velocities decreases slowly with r. Dark matter is though to be non-baryonic, consisting in undiscovered particles. The weakly interacting massive particles (WIMPs) are the most popular search candidates for dark matter which could interacts via gravity or any other force potentially not part of the SM itself [30]. Searches for dark matter particles are also performed at the LHC, for example through the invisible decay of the Higgs boson [31]. The *dark energy* is assumed to be a new form of energy with exotic physical properties, that was hypothesized to explain the acceleration rate of the Universe expansion [32].

- **Gravity**. While the Standard Model describes three of the four fundamental forces, gravity is interpreted in the theoretical framework of general relativity. However, general relativity appears to be incompatible with the underlying SM QFT.

- **Neutrino masses**. The masses of the neutrinos are very different from the masses of the other fermions, and if neutrinos were normal Dirac particles, this would imply an unnaturally small Yukawa coupling to the Higgs field.

One of the hypothetical model developed to provide an alternative explanation for the smallness of these masses is the *seesaw mechanism* [33], that describes neutrinos as *Majorana particles*, implying that the neutrinos are their own antiparticles, i.e. $\nu \equiv \bar{\nu} \equiv \nu_M$.

In addition to these phenomena the Standard Model has to face other issues, as the hierarchy problem, consisting in the large discrepancy between aspects of the weak force and gravity (as an example, the weak force appears to be many order of magnitudes stronger than gravity); the unexplained origin of the charge-parity violation; the renormalization problem, which consists in the appropriate extraction from the divergent pertubative integral of the finite and convergent part. In the last decades, many Beyond Standard Model (BSM) theories have been developed by scientists, in order to provide an extended and more exhaustive formulation of the Standard Model. Among them, the most popular is the theory of Supersymmetry (SUSY) that predicts a "super-symmetric partner" for each particles in the SM. Such particles would be characterized by the same mass of their respective SM particle, but they would possess a spin that differs by half of a unit. Hence, bosons would be associated with fermions and vice versa. The SUSY would solve many of the problems of the SM but, up to now, none of the supersymmetric particles has been observed and no other evidence of this theory has been found.

Chapter 2

Anomalous triple and quartic gauge couplings

In this chapter, the anomalous triple and quartic gauge couplings are introduced in the framework of the Effective Field Theory, whose features are described in the first section. The six- and eight-dimensions operators that arise in the Effective Field Theory parameterization are also listed. The multiboson processes now under study at the LHC are then presented, with a special focus on the 8 TeV analysis of $W\gamma\gamma$ and $Z\gamma\gamma$ processes performed at CMS. In particular, the results obtained in the evaluation of the limits on anomalous quartic gauge couplings are reported, together with the 8 TeV expected limits.

2.1 The Effective Field Theory

One of the possible strategy to search for new Beyond Standard Model (BSM) physics is looking for direct signals of new particles (i.e., the on-mass shell production of non-Standard Model (SM) particles). However, the Higgs boson was the last particle to be observed directly and, up to now, no one of the hypothetical new particles has been observed. It appears quite probable that their production requires collider energies not yet accessible, and, consequently, BSM effects need to be investigated using a different approach. New physics can in fact manifests itself also in the form of small deviations between measurements and predictions of properties of SM particles. Such deviations can be due to the virtual presence of new particles in quantum loops and in new amplitudes generated by their exchange at tree-level, thus changing the value of the measured cross sections. In section 1.3.3, Triple Gauge Couplings (TGC) and Quartic Gauge Couplings (QGC) have been described as a consequence of the non-Abelian SU(2)×U(1) gauge symmetry of the SM, and therefore their values are fixed and precisely predicted by theory. These couplings appears to be an interesting place to search for new physics in the framework on an Effective Field Theory (EFT), since they are particularly sensitive to

BSM effects that can modify their values, giving rise to anomalous TGC and QGC. The Effective Field Theory is a model-independent approach to physics of non-standard interactions. Using this kind of approach has two advantages. First, it allows to search for new physics without referring to a particular extension of the SM: this feature of EFT is quite important, since no one of the BSM theory has been proved true yet. Second, in the case that no new physics appears, it allows to quantify how accurately the new physics is excluded. In order to construct an EFT of the Standard Model the following features are needed [34]:

- The S-matrix axioms of unitarity and analitycity should be respected. The S-matrix connects the initial and the final state of a physical system undergoing a scattering process and therefore it is closely related to the transition probability amplitude in QFT and to the cross sections of the interactions.
- The symmetries of the SM (Lorentz invariance and $\mathrm{SU(3)} \times \mathrm{SU(2)_L} \times \mathrm{U(1)_Y}$ gauge symmetry) should be respected.
- The SM should be recovered in the appropriate limit.
- It should be possible to calculate radiative corrections at any order in the SM interactions.
- It should be possible to calculate radiative corrections at any order in the new interactions of the extended theory.

In the SM Lagrangian, all the operators are restricted to be of mass dimension four or less. The Lagrangian can be extended adding operators of higher dimension that, by dimensional analysis, result to have coefficients of inverse powers of mass and hence they are suppressed if such mass is large compared with the experimentally-accessible energies

$$\mathcal{L}_{EFT} = \mathcal{L}_{SM} + \sum_{d>4} \sum_{i} \frac{c_i}{\Lambda^{d-4}} O_i.$$

Λ is termed the mass scale, and the dimensionless coefficients c_i of the higher-dimension operators O_i parameterize the strength with which the new physics couples to the SM particles, while d corresponds to the dimension of the operators. The SM Lagrangian is recovered in the limit $\Lambda \to \infty$. The mass scale Λ can be regarded as the scale of new physics and it is required to be large compared with the experimentally-accessible energies. In that sense, the EFT is a low-energy approximation to the new physics, where "low" means less than Λ, and the dominant extended operators will therefore be those of the lowest dimensionality. Operators with odd dimension do not conserve baryon and lepton numbers and for that reason they are generally neglected in Standard Model EFT. Consequently, the largest new physics contribution is expected from dimension-six and dimension-eight operators, which affect the triple and quartic gauge couplings.

2.1.1 Dimension-six operators

There is no reason to believe that C and P are conserved by the dimension-six operators, unless the physics beyond the standard model respects these symmetries. Therefore, three dimension-six operators that conserve CP can be written

$$\begin{aligned} \mathcal{O}_{WWW} &= Tr\left[W_{\mu\nu}W^{\nu\rho}W^{\mu}_{\rho}\right] \\ \mathcal{O}_{W} &= (D_\mu\phi)^\dagger W^{\mu\nu}(D_\nu\phi) \\ \mathcal{O}_{B} &= (D_\mu\phi)^\dagger B^{\mu\nu}(D_\nu\phi) \end{aligned}$$

and two dimension-six operators that violate CP

$$\begin{aligned} \mathcal{O}_{\widetilde{W}WW} &= Tr\left[\widetilde{W}_{\mu\nu}W^{\nu\rho}W^{\mu}_{\rho}\right] \\ \mathcal{O}_{\widetilde{W}} &= (D_\mu\phi)^\dagger \widetilde{W}^{\mu\nu}(D_\nu\phi) \end{aligned}$$

where $\widetilde{W}_{\mu\nu} = \sum_j W^j_{\mu\nu}\frac{\sigma^j}{2}$ and ϕ corresponds to the Higgs doublet field. The covariant derivative for ϕ, which has hypercharge $Y = 1/2$ is given by

$$D_\mu \equiv \partial_\mu + i\frac{g'}{2}B_\mu + ig_W\mathbf{W}_\mu\frac{\mathbf{T}^\mu}{2}.$$

In addition, there are also three CP-conserving operators

$$\begin{aligned} \mathcal{O}_{\phi d} &= \partial_\mu(\phi^\dagger\phi)\partial^\mu(\phi^\dagger\phi) \\ \mathcal{O}_{\phi W} &= (\phi^\dagger\phi)Tr[W^{\mu\nu}W_{\mu\nu}] \\ \mathcal{O}_{\phi B} &= (\phi^\dagger\phi)B^{\mu\nu}B_{\mu\nu} \end{aligned}$$

and two CP-violating operators

$$\begin{aligned} \mathcal{O}_{\widetilde{W}W} &= \phi^\dagger\widetilde{W}_{\mu\nu}W^{\mu\nu}\phi \\ \mathcal{O}_{\widetilde{B}B} &= \phi^\dagger\widetilde{B}_{\mu\nu}B^{\mu\nu}\phi \end{aligned}$$

that modify the coupling of the Higgs boson to the weak gauge bosons. In Table 2.1 the list of triple and quartic couplings produced by each dimension-six operator is reported. The operators affecting the couplings of the bosons to fermions have been neglected. This is a minimal set of independent dimension-six operators involving vertices of three and four electroweak gauge bosons [35]. In fact, the choice of the basis of operators is not unique and additional dimension-six operators invariant under SM symmetries can be constructed, but they can be shown to be equivalent to a linear combination of the ones described above.

2.1.2 Dimension-eight operators

In can be seen in Table 2.1 that the dimension–six operators giving rise to QGCs also exhibit TGCs. The lowest dimension operator that leads to quartic interactions without involving two or three weak gauge boson vertices is of dimension eight. There are three classes of genuine QGC operators [35], and all quartic couplings that they induce are reported in Table 2.2.

	ZWW	AWW	HWW	HZZ	HZA	HAA	WWWW	ZZWW	ZAWW	AAWW
$\mathcal{O}_{WWW}$	X	X					X	X	X	X
$\mathcal{O}_{W}$	X	X	X	X	X		X	X	X	
$\mathcal{O}_{B}$	X	X		X	X					
$\mathcal{O}_{\Phi d}$			X	X						
$\mathcal{O}_{\Phi W}$			X	X	X	X				
$\mathcal{O}_{\Phi B}$				X	X	X				
$\mathcal{O}_{\tilde{W}WW}$	X	X					X	X	X	X
$\mathcal{O}_{\tilde{W}}$	X	X	X	X	X					
$\mathcal{O}_{\tilde{W}W}$			X	X	X	X				
$\mathcal{O}_{\tilde{B}B}$				X	X	X				

Table 2.1: TGCs and QGCs produced by each dimension-six operator. The couplings induced by each of them are marked with X in the corresponding column [35].

Operators containing only $D_\mu\phi$

This class contains two independent operators

$$\begin{aligned} O_{S,0} &= \left[(D_\mu\phi)^\dagger(D_\nu\phi)\right] \times \left[(D^\mu\phi)^\dagger(D^\nu\phi)\right] \\ O_{S,1} &= \left[(D_\mu\phi)^\dagger(D^\mu\phi)\right] \times \left[(D_\nu\phi)^\dagger(D^\nu\phi)\right]. \end{aligned}$$

These operators contain quartic $W^+W^-W^+W^-$, W^+W^-ZZ and ZZZZ interactions that do not depend on the gauge boson momenta.

Operators containing $D_\mu\phi$ and two field strength tensors

This class contains the following operators, generated by considering two electroweak field strength tensors and two covariant derivatives of the Higgs doublet

$$\begin{aligned} O_{M,0} &= Tr\left[W_{\mu\nu}W^{\mu\nu}\right] \times \left[(D_\beta\phi)^\dagger D^\beta\phi\right] \\ O_{M,1} &= Tr\left[W_{\mu\nu}W^{\nu\beta}\right] \times \left[(D_\beta\phi)^\dagger D^\mu\phi\right] \\ O_{M,2} &= \left[B_{\mu\nu}B^{\mu\nu}\right] \times \left[(D_\beta\phi)^\dagger D^\beta\phi\right] \\ O_{M,3} &= \left[B_{\mu\nu}B^{\nu\beta}\right] \times \left[(D_\beta\phi)^\dagger D^\mu\phi\right] \\ O_{M,4} &= \left[(D_\mu\phi)^\dagger W_{\beta\nu}D^\mu\phi\right] \times B^{\beta\nu} \\ O_{M,5} &= \left[(D_\mu\phi)^\dagger W_{\beta\nu}D^\nu\phi\right] \times B^{\beta\mu} \\ O_{M,6} &= \left[(D_\mu\phi)^\dagger W_{\beta\nu}W^{\beta\nu}D^\mu\phi\right] \\ O_{M,7} &= \left[(D_\mu\phi)^\dagger W_{\beta\nu}W^{\beta\mu}D^\nu\phi\right]. \end{aligned}$$

In this class of operators the quartic gauge-boson interactions depend upon the momenta of the vector bosons due to the presence of the field strength in their definitions.

Operators containing only field strength tensors

This class contains the following operators

$$\begin{aligned}
O_{T,0} &= Tr\left[W_{\mu\nu}W^{\mu\nu}\right] \times Tr\left[W_{\alpha\beta}W^{\alpha\beta}\right] \\
O_{T,1} &= Tr\left[W_{\alpha\mu}W^{\nu\beta}\right] \times Tr\left[W_{\mu\beta}W^{\alpha\nu}\right] \\
O_{T,2} &= Tr\left[W_{\alpha\mu}W^{\mu\beta}\right] \times Tr\left[W_{\beta\nu}W^{\nu\alpha}\right] \\
O_{T,5} &= Tr\left[W_{\mu\nu}W^{\mu\nu}\right] \times B_{\alpha\beta}B^{\alpha\beta} \\
O_{T,6} &= Tr\left[W_{\alpha\mu}W^{\nu\beta}\right] \times B_{\mu\beta}B^{\alpha\nu} \\
O_{T,7} &= Tr\left[W_{\alpha\mu}W^{\mu\beta}\right] \times B_{\beta\nu}B^{\nu\alpha} \\
O_{T,8} &= B_{\mu\nu}B^{\mu\nu}B_{\alpha\beta}B^{\alpha\beta} \\
O_{T,9} &= B_{\alpha\mu}B^{\mu\beta}B_{\beta\nu}B^{\nu\alpha}.
\end{aligned}$$

As one can see, the last two operators give rise to QGCs containing only the neutral electroweak gauge bosons.

	WWWW	WWZZ	ZZZZ	WWAZ	WWAA	ZZZA	ZZAA	ZAAA	AAAA
$\mathcal{O}_{S,0}$, $\mathcal{O}_{S,1}$	X	X	X						
$\mathcal{O}_{M,0}$, $\mathcal{O}_{M,1}$,$\mathcal{O}_{M,6}$,$\mathcal{O}_{M,7}$	X	X	X	X	X	X	X		
$\mathcal{O}_{M,2}$,$\mathcal{O}_{M,3}$, $\mathcal{O}_{M,4}$,$\mathcal{O}_{M,5}$		X	X	X	X	X	X		
$\mathcal{O}_{T,0}$,$\mathcal{O}_{T,1}$,$\mathcal{O}_{T,2}$	X	X	X	X	X	X	X	X	X
$\mathcal{O}_{T,5}$,$\mathcal{O}_{T,6}$,$\mathcal{O}_{T,7}$		X	X	X	X	X	X	X	X
$\mathcal{O}_{T,8}$,$\mathcal{O}_{T,9}$			X			X	X	X	X

Table 2.2: QGCs produced by each dimension-eight operator. The couplings induced by each of them are marked with X in the corresponding column [35].

2.2 Multiboson production

Triple and quartic gauge couplings have been first studied at LEP [36] and Tevatron [37], even though the limited statistics did not allow to test all the possible couplings. At present, multiboson production is under study at LHC. In the following section, the main diboson and triboson processes investigated by ATLAS and CMS experiment are briefly listed.

2.2.1 Diboson production

Diboson production is dominated by $q\bar{q}$ annihilation, as shown in Figure 2.1. The main diboson processes studied at LHC by both ATLAS and CMS experiments are listed below [38].

- **Wγ and Zγ production**
  The cross section of such final state has been measured and limits on aTGC

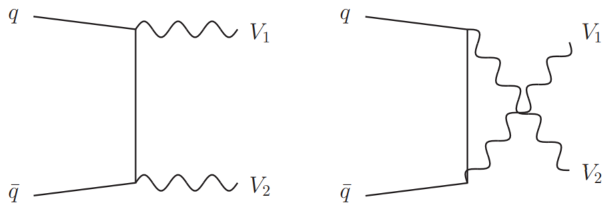

Figure 2.1: Leading-order Feynman diagrams for diboson production [39].

at 95% confidence level were placed by both CMS [40] and ATLAS [41] at a center of mass of 7 TeV, with an integrated luminosity of approximately 5 fb^{-1}. The W boson was observed in the leptonic final state, with the charged lepton being either an electron or a muon, while the Z boson was identified by a pair of oppositely charged electron or muon. The photon was required to be isolated in both processes. The SM TGC which contributes to $\mathrm{W}\gamma$ production is the $\mathrm{WW}\gamma$ coupling, while the TGCs for $\mathrm{Z}\gamma$ processes are $\mathrm{ZZ}\gamma$ and $\mathrm{Z}\gamma\gamma$, which arise at loop level.

- $\mathrm{W}^{+}\mathrm{W}^{-}$ **production**
  Two decay modes have been studied. In the leptonic mode, both W bosons decay into a charged lepton and a neutrino. In the semi-leptonic case, one W boson decays leptonically while the other decays hadronically. The leptonic decay have been studied by CMS [42] and ATLAS [43] at 8 TeV ($\sim$ 20 fb^{-1}). The production cross section was measured and the limits on anomalous $\mathrm{WW}\gamma$ and WWZ couplings were placed. The semi-leptonic decay has to be studied together with the WZ production, since the hadronic W boson decays can not be fully distinguished from hadronic Z boson decays due to limited dijet mass resolution. The WW + WZ cross section was measured in the $\ell\nu jj$ final state ($\ell = \mathrm{e}, \mu$) by CMS [44] and ATLAS [45] at 7 TeV ($\sim$ 5 fb^{-1}) and both experiments also constrain anomalous $\mathrm{WW}\gamma$ and WWZ couplings.

- $\mathrm{W}^{\pm}\mathrm{Z}$ **production**
  Such production has been studied by CMS [46] and ATLAS [47; 48] at 7 and 8 TeV ($\sim$ 5 fb^{-1} and 20 fb^{-1} respectively), considering in the final state the leptonic decay of both W and Z bosons. The cross section and the limits on the aTGC were evaluated. In particular, the $\mathrm{W}^{\pm}\mathrm{Z}$ production includes only the TGC of WWZ, as opposed to WW production which has both $\mathrm{WW}\gamma$ and WWZ vertices.

- ZZ **production**
  The production of ZZ boson pairs has been studied in two decay modes. In the 4ℓ mode both Z bosons decay into same-flavour, oppositely-charged lepton pairs, while in the $2\ell 2\nu$ mode one Z boson decays into a same-flavour, oppositely-charged lepton pair, while the other one decays to neutrinos, pro-

ducing a large missing transverse energy in the final state. Both decay modes have been studied by CMS [49; 50] and ATLAS [51; 52] at 7 and 8 TeV (~ 5 fb^{-1} and 20 fb^{-1} respectively). In the SM there are no TGC for the double Z boson production (the HZZ vertex is here not considered to be a TGC vertex), but anomalous ZZγ and ZZZ couplings can arise in analogy with the Zγ case.

2.2.2 Triboson production

The inclusive production of three gauge bosons has a much lower cross section compared to that for the production of two gauge bosons. The main triboson processes studied at LHC by both ATLAS and CMS experiments are listed below [38], except for the W$\gamma\gamma$ and the Z$\gamma\gamma$ processes that will be described in the following sections.

- **WVγ production**
  The semileptonic decays with one charged lepton (electron or muon), missing transverse energy, at least two jets and an energetic photon in the final state represent an extension of the study of WV production (with V=W or Z) described in section 2.2.1. As before, the W and the Z bosons can not be fully distinguished due to the limited dijet mass resolution. The production of WVγ has been studied by CMS [53] at 8 TeV and the limits on the anomalous WWZγ and WW$\gamma\gamma$ gauge couplings were placed.

- **$W^{\pm}W^{\pm}W^{\mp}$ production**
  This triboson production constitutes the largest inclusive triple gauge boson cross section with three massive bosons and it has been studied first by ATLAS [54] at 8 TeV, selecting final states with three leptons (electrons or muons), or with two same-charge leptons plus two jets. Limits were also set on WWWW anomalous quartic gauge couplings. The same analysis has been then performed by CMS [55] at 13 TeV (~ 36 fb^{-1}).

2.2.3 Vector Boson Scattering and Vector Boson Fusion

Vector boson scattering (VBS) and vector boson fusion (VBF) processes, as the multiboson production, can be used to study aTGC and aQGC. They are predicted by the SM, as a consequence of the non-Abelian structure of the electroweak interaction. Both processes are initiated by two quarks, produced by the two colliding protons, that emit an electroweak gauge boson (W, Z or γ). The two bosons can fuse together to form a single boson (VBF) or scatter (VBS). The outgoing quarks produce hadronic jets, commonly referred to as tagging jets, near to the initial beam directions. The main VBF processes studied at LHC are the productions of a W or a Z boson in association with two jets. The Wjj and Zjj processes have been studied at 7 [56] and 8 TeV [57; 58] by the CMS experiment in order to extract the fiducial cross section and to place the limits on the WWγ, WWZ and WWZ aTGC respectively. The main VBS processes are listed below [38].

- **W$^{\pm}\gamma jj$ production**
  This is the largest cross-section VBS process studied at the LHC and it includes SM QGC contributions from the WW$\gamma\gamma$ and WWZγ vertices. CMS has performed a search for such production using leptonic W boson decays in final states with one charged lepton (electron or muon), missing transverse energy, two jets well-separated in rapidity and an energetic photon at a center of mass energy of 8 TeV [59].

- **W$^{\pm}Vjj$ production**
  The semileptonic final state of such process includes contributions from the W$^{\pm}$W$^{\pm}jj$, W$^{\pm}$W$^{\mp}jj$, and W$^{\pm}$Zjj VBS processes and it has been studied by ATLAS at 8 TeV [60]. The analysis also sets constraints on the aQGC. The fully leptonic final state in the W$^{\pm}$W$^{\pm}jj$ production has been studied by both CMS [61] and ATLAS [62] at 8 TeV, requiring the two tagging jets to exhibit a large dijet invariant mass and to be well-separated in rapidity. Limits on WWWW aQGC have been set. The fully leptonic final state in W$^{\pm}$Zjj production has been studied by ATLAS [63] at 8 TeV, and limits on the WZWZ and WγWZ anomalous QGC were placed.

2.3 W$^{\pm}\gamma\gamma$ and Z$\gamma\gamma$ production

The study of the leptonic final states of such triboson production has been performed by CMS [64] and ATLAS [65; 66] at a center of mass of 8 TeV. The largest cross section is that for W$^{\pm}\gamma\gamma$ production, and the best signal-to-background ratio is achieved when studying the leptonic W boson decay modes into a charged lepton (e or μ) and a neutrino [38]. The SM Z$\gamma\gamma$ triboson production arises from Z boson production with photons radiated off from initial state quarks or final state radiation photons from a Z decay lepton, since the ZZ$\gamma\gamma$ vertex are not allowed in the SM but can arise in the framework of a dimension-eight EFT. The Feynman diagrams that enter into the leading order matrix element for W$^{\pm}\gamma\gamma$ and Z$\gamma\gamma$ production, are shown in Figure 2.2 and 2.3.

The Z$\gamma\gamma$ production can be studied in two decay modes: in the first one, the Z boson decays into a same-flavour, oppositely-charged lepton (e or μ) pair, in the second one it decays into neutrinos, giving rise to large missing transverse energy in the final state. In both modes, the two photons are required to be energetic and isolated. The cross sections of both processes have been calculated at the next-to-

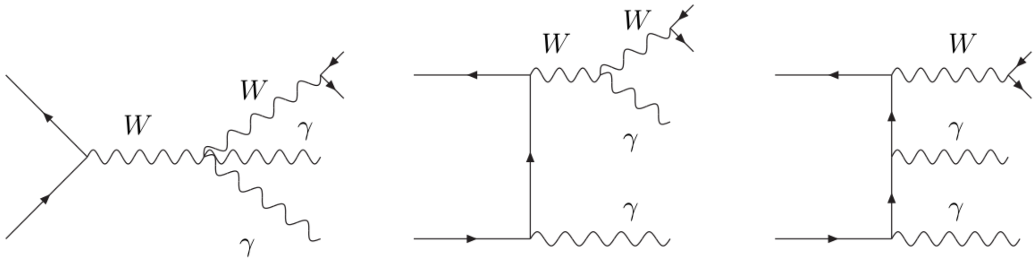

Figure 2.2: Examples of the three topologies of Feynman diagrams contributing to the W$\gamma\gamma$ process at tree-level.

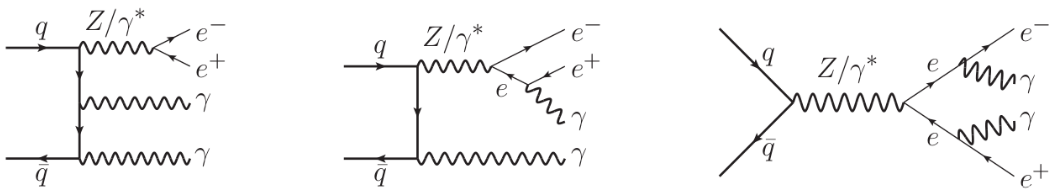

Figure 2.3: Examples of the three topologies of Feynman diagrams contributing to the Z$\gamma\gamma$ process at tree-level.

leading order (NLO) in QCD [67; 68] and they result to be strongly dependent on the threshold applied to the transverse momentum (p_T) of the photons.

2.3.1 The anomalous $W^{\pm}W^{\mp}\gamma\gamma$ coupling

In the CMS analysis [64], operators of dimension-eight were used to study only aQGC, since they do not produce aTGC, unlike dimension-six operators. In particular, in a dimension-eight effective field theory, the $W^{\pm}\gamma\gamma$ final state has a contribution from only the $W^{\pm}W^{\mp}\gamma\gamma$ quartic coupling, and the operators that affect such vertex are $O_{M,0}$, $O_{M,1}$, $O_{M,2}$, $O_{T,0}$, $O_{T,1}$, $O_{T,2}$ and $O_{T,3}$, as defined in 2.1.2. The $O_{M,0}$ and $O_{M,2}$ contributions are the same except for a factor of $\frac{1}{2}\sin\theta_W^2$ on the first and $\cos\theta_W^2$ on the second, where θ_W is the Weinberg angle, i.e. $O_{M,0}$ behaves the same way as $O_{M,2}$ with a coupling strength 6.67 times greater (Figure 2.4). To set limits on the anomalous QGC, the region of interest was restricted to events with leading photon p_T greater than 70 GeV since, at low photon p_T, the difference in SM and aQGC events is not significant. However, the EFT theory is not always valid

Coupling	Unitarity limit (GeV)
f_{T0}	1860
f_{T1}	2403
f_{T2}	2061
f_{M2}	1206
f_{M3}	1575

Table 2.3: Unitarity limits for the couplings f considered in the CMS analysis [64]

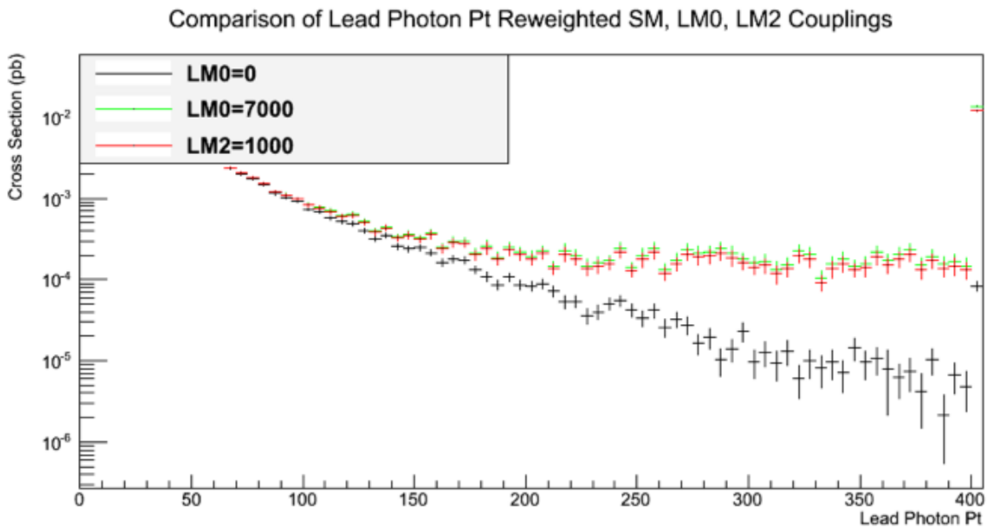

Figure 2.4: Cross section for the $W^{\pm}\gamma\gamma$ process, plotted as a function of the leading photon p_T. $O_{M,0}$ behaves the same way as $O_{M,2}$ with a coupling strength about 7 times greater [64].

since, if the coupling constant related to the new physics grows, the amplitude could become greater than one, violating unitarity. Hence, a form factor that reduces the anomalous coupling parameter at energies near the unitarity limit has to be introduced. The unitary limit corresponds to the energy at which a form factor is required to avoid unitarity violation and its values for the couplings considered in the analysis are reported in Table 2.3. The limits would be violated if a significant number of signal events are produced having an invariant mass above them. The coupling constant c is modified by an introduction of a form factor in the following way

$$c \rightarrow \frac{c}{\left(1 + \hat{s}/\Lambda^2\right)}$$

where $\hat{s}$ is the collision energy and Λ is the scale of the new physics. All limits are far beyond 1 TeV. In the signal simulation samples the number of predicted events where the invariant mass of the final state lepton, neutrino and photons is greater than 1 TeV is less than 0.1. Therefore unitarity is not violated for the aQGCs considered and the relative limits are reported in Table 2.4.

$W\gamma\gamma$	Expected (TeV^{-4})	Observed (TeV^{-4})
$f_{M,2}/\Lambda^4$	$[-549, 531]$	$[-701, 683]$
$f_{M,3}/\Lambda^4$	$[-916, 950]$	$[-1170, 1220]$
$f_{T,0}/\Lambda^4$	$[-26.5, 27.0]$	$[-33.5, 34.0]$
$f_{T,1}/\Lambda^4$	$[-34.5, 34.8]$	$[-44.3, 44.8]$
$f_{T,2}/\Lambda^4$	$[-74.6, 73.7]$	$[-93.8, 93.2]$

Table 2.4: Expected and observed limits on anomalous quartic gauge couplings with a confidence level of 95%. Limits are obtained using $W\gamma\gamma$ events in which the leading photon p_T exceeds 70 GeV [64].

Chapter 3

Monte Carlo event generators

In this chapter, an overview of the most common used Monte Carlo event generators is presented. The structure of a proton-proton collision at the LHC is described, and the different steps in the generation of an event are outlined. The event generators used to produce the 13 TeV samples are then specified, and the reweighting procedure of the Monte Carlo samples is also illustrated.

3.1 Structure of the events

Monte Carlo (MC) event generators are software libraries used to produced simulation of the final states of high-energy collisions. The generated distributions are compared with data in order to estrapolate a signal region over the background and to perform measurements of the SM parameters, calibrate the detectors or to develop new techniques to propose to the experiments. The structure of a proton-proton collision at the LHC, as built up by the MC event generators, can be described by the following main steps [69]:

- Hard process
- Parton shower
- Hadronization
- Underlying event
- Unstable particle decays

The simulation is started calculating the probability distribution of the highest momentum transfer process in the event, i.e. the hard process, from perturbation theory. The scattered quarks radiate gluons that can themselves radiate other gluons, since they possess colour charge. This leads to an extended parton "shower" which lasts until the partons have enough momentum to continue radiating and they get confined into hadrons through the hadronization processes. Then, unstable hadrons decay into secondary particles. Apart from the hard process, one must take into account the underlying events, which consist of secondary interactions between proton remnants plus initial and final state radiation. A qualitative picture of the structure of an event is shown in Figure 3.1.

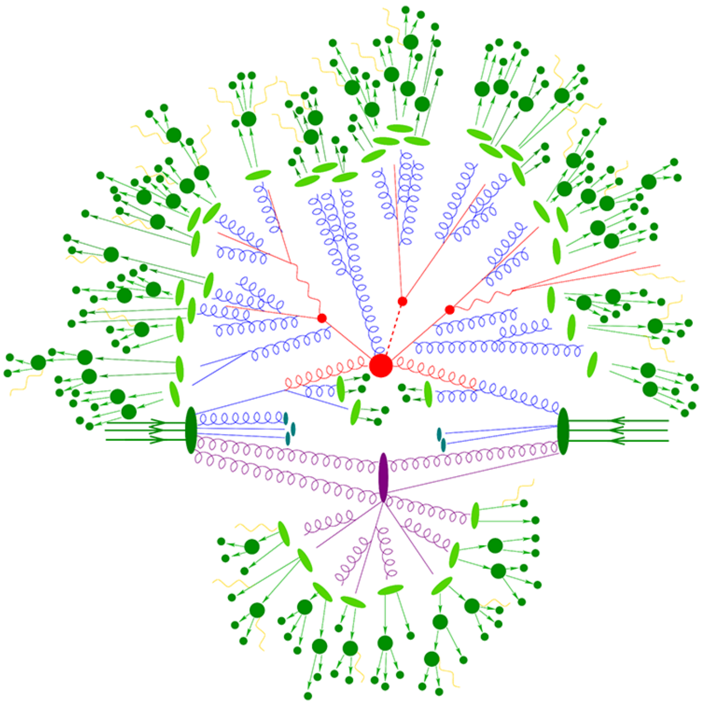

Figure 3.1: Qualitative picture of a proton-proton collision at the LHC. The hard process is shown in red, the parton shower in blue, the beam remnants in light blue, the multiple interactions in violet and in light and dark green the hadronization and the hadron decays.

3.2 Monte Carlo methods

Event generators employ Monte Carlo methods in order to produce a set of representative points in the phase space of the process under study, according to the probability distribution predicted for such process. Consider the simple case of a single variable x to be distributed in the region $[x_{min}, x_{max}]$ with probability distribution proportional to $f(x) \geq 0$ [70]. The values of x can be generated as follows

$$\int_{x_{min}}^{x} f(x')\mathrm{d}x' = R \int_{x}^{x_{max}} f(x')\mathrm{d}x'$$

where $R \in [0, 1]$ is a uniform, pseudo-random number. This expression is equivalent to

$$F(x) = RF(x_{max}) + (1 - R)F(x_{min})$$

where $F(x)$ is the indefinite integral of $f(x)$. The equation can be solved once provided the inverse function F^{-1}. If the inverse function is not known the *hit-or-miss* method can be used, considering a function $g(x) \geq f(x)$ in the same interval $[x_{min}, x_{max}]$, that has a known indefinite integral $G(x)$ which can be inverted for x. Once a new distribution has been generated according to $g(x)$, the points that are accepted are those for which $f(x) < R'g(x)$, where $R' \in [0, 1]$ is another pseudo-random number. In particular, $g(x)$ can be chosen to be a constant $g(x) = g_u \geq \max\{f(x), x \in [x_{min}, x_{max}]\}$, generating the distribution as

$$x = Rx_{max} + (1 - R)x_{min},$$

and the points are accepted if $f(x) \geq R'g_u$. In a collision at the LHC, the phase space has $3n - 4$ dimension, where n is the number of particles produced in the final state. Each particle has three components of momentum, while the four constraints account for the overall energy-momentum conservation. Performing an integration, for example for the calculation of a cross section, over a multidimensional phase space using standard integration methods is too laborious and it leads often to inaccurate results. To figure out this issue, the concept of an integral as an average, on which the Monte Carlo method is based, can be exploited. For example, suppose to integrate a function $f(\mathbf{x})$ over a region V of the $\mathbf{x}$-space, where $\mathbf{x}$ is a m-component vector.

$$I[f] = \int_V \mathrm{d}^m x f(\mathbf{x})$$

If the M points $\{\mathbf{x}_i, i = 1, ..., M\}$ are randomly distributed in V, according to the central limit theorem of statistics, the mean value of f on those points is the unbiased estimator of the integral

$$I = \langle f \rangle \simeq \frac{1}{M} \sum_{i=1}^{M} f(\mathbf{x}_i)$$

whose estimated error $E[f]$ is given by the variance of f

$$Var\langle f \rangle = \langle f^2 \rangle - \langle f \rangle^2,$$

and therefore

$$E[f] = \sqrt{\frac{Var\langle f \rangle}{M - 1}}.$$

To each point in the phase space a weight $w = f_i$ can be associated. To compare the generated distribution with data the events need to be unweighted, comparing the value of w_i/w_{max} for randomly chosen phase-space points with a random number $R'' \in [0, 1]$. If $w_i/w_{max} > R''$ the point is accepted. The fraction of generated events kept is termed efficiency of the generators and it is $w_{average}/w_{max}$.

3.3 Generating events

3.3.1 Hadronic collisions

The cross section for a hard scattering process $ab \to n$ in proton-proton collisions can be written in the collinear factorization limit as [70]

$$\sigma = \sum_{a,b} \int_0^1 \mathrm{d}x_a \mathrm{d}x_b \int \mathrm{d}\Phi_n f_a^{h_1}(x_a, \mu_F) f_b^{h_2}(x_b, \mu_F)$$
$$\times \frac{1}{2\hat{s}} |M_{ab\to n}|^2 (\Phi_n; \mu_R, \mu_F)\,.$$

The sum is performed over all the possible types of initial partons a and b, while $\mathrm{d}\Phi_n$ is the differential phase space element over the n final-state particles

$$\mathrm{d}\Phi_n = \prod_{i=1}^{n} \frac{\mathrm{d}^3\mathrm{p_i}}{2E_i(2\pi)^3} \cdot (2\pi)^4 \delta^{(4)} \left(p_a + p_b - \sum_{i=1}^{n} p_i \right)$$

where p_a and p_b are the partons initial-state momenta, given by $x_a P_a$ and $x_b P_b$. The momentum fraction x of a parton with respect to the total momentum P of its parent hadron, is termed the Bjorken variable. $f_a^h(x, \mu)$ are the Parton Distribution Functions (PDFs) that describe momenta distributions among quarks and gluons inside the proton. They depend on the Bjorken variable x of parton a with respect to its parent hadron h, and on the factorization scale μ_F. Qualitatively, μ_F corresponds to the resolution with which the hadron is being probed [71]. μ_R is the renormalization scale. The parton flux is $1/2\hat{s} = 1/2x_a x_b s$ where s is the hadronic center-of-mass energy squared. The factorization allows to separate the perturbative computations for short-distance particle interactions from the non-perturbative terms (the PDFs), associated to long-distance particle interactions. In the collinear approximation, the transverse momentum of the partons inside the hadrons is neglected. To compute the cross section, the matrix element (ME) squared $|M_{ab\to n}|^2$ has to be evaluated for each point in the phase-space. At leading order the ME can be computed with different methods, using dedicated generators. In general, it can be written as a sum over Feynman diagrams, including the summation over the possible helicities and colour configurations.

3.3.2 Parton shower

After the generation of a hard process according to the matrix elements, the parton shower has to be implemented. Through the parton shower, particles momentum decrease down to approximately 1 GeV, which is the energy at which perturbation theory breaks down and the partons get confine into hadrons. The original cross section that produces partons of any flavour i is modified by the emission of another parton j in the following way

$$\sigma \sim \sigma_0 \sum_{partons,i} \frac{\alpha_s}{2\pi} \frac{\mathrm{d}\theta}{\theta^2} \mathrm{d}z P_{ij}(z,\phi) \mathrm{d}\phi$$

where θ and ϕ are the opening and the azimuthal angle of the emission, and z is the fraction of the energy of i carried by j. The functions $P_{ij}(z,\phi)$ that describe the distribution of z are known as the Dokshitzer-Gribov-Lipatov-Altarelli-Parisi (DGLAP) and they are flavour-dependent. This formula can be iterated to generate the parton shower, however, it diverges for collinear emission ($\theta \to 0$) and for emission of soft gluons ($z \to 0$). A physical measurement in fact can not distinguish an exactly collinear pair of partons from a single parton with the same total momentum and other quantum numbers. In order to resolve the two partons, an energy cutoff Q_0 is introduced, that eliminates both divergences.

3.3.3 Matching with the matrix elements and hadronization

The fixed-order matrix elements need to be matched with the parton shower in order to obtain the correct partonic final states. If the matrix elements are evaluated at the leading order, the "CKKW" or the "MLM" matching scheme can be used [72]. The idea underlying CKKW is to divide the phase space of partonic emissions into a regime of jet production, described by matrix elements, and a regime of jet evolution, described by parton showering. The separation between two regimes is defined by a merging scale Q_{cut}. The jets are identified through the $k_\perp$-algorithm, according to which two final-state particles belong to two different jets, if their relative transverse momentum

$$k_\perp^{(ij)^2} = 2\min\{p_\perp^(i), p_\perp^(j)\} \left[\cosh(\eta^{(i)} - \eta^{(j)}) - cosh(\phi^{(i)} - \phi^{(j)})\right]$$

is larger than a critical value, $k_{\perp,0}^2$. The matrix elements are then reweighted to include terms that would appear in the corresponding parton shower evolution, and a smooth transition between them and the parton shower region is achieved by choosing suitable starting conditions. The MLM matching scheme instead does not make use of reweighting procedures. The events at parton level are defined by a minimum transverse energy threshold E_T^{min} and a minimum separation among them $\Delta R > R_{min}$. The events are then showered and the jets are identified using a jet cone algorithm with cone size R_{min} and minimum transverse energy E_T^{min}. For the matching, the jets which are closest in (η, ϕ) to a parton are selected, and if the distance between the parton and the centroid of one of these jets is smaller than R_{min}, the matching can be performed. If there are no jet candidates satisfying the matching requirements, the event is rejected. The rejection procedure is so able to remove double counting that can arise in the production of two collinear partons, or soft partons.

If the ME are evaluated at the NLO insted, the merging procedure becomes slightly different. The cross section at NLO is in fact composed of three part, the LO part (or Born-level part), and the real and the virtual emission parts, corresponding to high-level corrections

$$d\sigma^{NLO} = d\widetilde{\Phi}_n \left[\mathcal{B}(\widetilde{\Phi}_n) + \alpha_S \mathcal{V}(\widetilde{\Phi}_n)\right] + d\widetilde{\Phi}_{n+1}\alpha_S \mathcal{R}(\widetilde{\Phi}_{n+1}).$$

The tildes over the phase space elements denote integrals over the n-particle final state and the Bjorken variables, including the incoming partonic flux. The PDFs, and the summation over flavours are implicit in the formula. The terms $\mathcal{B}$, $\mathcal{V}$, and $\mathcal{R}$ denote the Born, virtual and real emission parts. In particular, the virtual corrections correspond to the emission and subsequently re-absorption of a gluon, while the real corrections to its emission only. In order to describe the difference between the leading and higher order cross sections the theoretical K-factor is defined as the ratio [74]

$$K_{th}^{(1)} = \frac{\sigma^{NLO}}{\sigma^{LO}}$$

where the superscript (1) indicates that only the first order corrections have been taken into account. The infrared and ultraviolet divergences appearing in the evaluation of this cross section are treated using infrared subtraction algorithms and dimensional regularization, respectively. The merging of the parton shower and the matrix elements in such case has to be performed in a different way, in order to take into account the NLO corrections and to eliminate the double counting of the possible same configuration that can arise both from the parton shower and from the NLO. To perform that, consider a typical cross section for a process with a given Born-level state

$$\begin{aligned} d\sigma^{NLO} &= d\Phi_0 \left[B(\Phi_0) + \alpha_S V_1(\Phi_0) + \int d\Phi_{1|0} S_1(\Phi_1)\right] \\ &\quad + d\Phi_1 \alpha_S \left[R_1^s(\Phi_1) - S_1(\Phi_1)\right] + d\Phi_1 \alpha_S R_1^{ns}(\Phi_1) \end{aligned}$$

where the real part of the cross section has been splitted in one containing all the singularities R_1^s, and the no singular one R_1^{ns}, while the virtual part of the cross section is $V_1(\Phi_0)$. Φ_0 and Φ_1 constitute the real-emission phase space and $B(\Phi_0)$ is the corresponding tree-level matrix elements. The subtraction factor S_1 regularizes the real emission part, making everything finite. After the first emission in the parton shower, the cross section is modified as follows

$$\begin{aligned} d\sigma^{PS} &= d\Phi_0 B(\Phi_0) \left[\overline{\Delta}(Q^2, Q_0^2) + \int d\Phi_{0|1(>Q_0^2)} \alpha_S \frac{R_1^s(\Phi_0)}{B(\Phi_0)} \overline{\Delta}(Q^2, q_1^2)\right] \\ &\quad + d\Phi_1 \alpha_S R_1^{ns}(\Phi_1). \end{aligned}$$

The ordering variable [75] for the parton shower is q, while Q and Q_0 are the starting energy scale and the cutoff scale of the shower, respectively. The number of gluons emitted at each step of the parton shower is arbitrary, with probability controlled by the Sudakov form factors $\overline{\Delta}(Q^2, q^2)$ [76]. The aim of the merging is to obtain $O(\alpha_S)$ accuracy at the cross section level. For this purpose, different methods can be employed. The first one is the POWHEG [77] (POsitive Weight Hardest Emission Generator) approach, that consists in reweighting the matrix element, replacing the Born-level term $B(\Phi_0)$ in the first emission cross section with the weighted Born-level term

$$\overline{B}(\Phi_0) = B(\Phi_0) + \alpha_S V_1(\Phi_1) + \alpha_S \int \mathrm{d}\Phi_{1|0} S_1 \Phi_1 + \alpha_S \int \mathrm{d}\Phi_{1|0} \left[R_1^s(\Phi_1) - S_1(\Phi_1)\right]$$

in a way that $R_1^{ns} = 0$. Another, widely used approach, is the MC@NLO [78]. In that case, the singular terms R_1^s are assumed to be identical to the subtraction terms S_1. The jet matching at NLO can be also performed using the FxFx matching scheme [79], that consists in an improved and extended version of the MLM scheme and makes use of a $k_\perp$ jet-finding algorithm. A function of the mass scale is introduced in order to dealing with the different configurations arising in a n partons productions. The reconstruction could be in fact return a n-jets configuration, or a $(n-1)$-jets configuration, since the matrix element for the process gives the Born contribution to the n parton production but also the first order contribution to a $(n-1)$ parton production. The partons produced after the parton shower need to be combine to produce the hadronic final state. The two most commonly used model for the hadronization are the string and cluster ones. The first one is based on the assumption of linear confinement, as described in section 1.4.1, and confine partons directly into hadrons, while the second method instead employs intermediate clustered objects, with a typical mass scale of a few GeV. The last part of the generation consists in the decay of the hadrons. The simulation of such decays is based on the results of experimental measurements provided in the Particle Data Group (PDG)'s Review of Particle Physics, but such information is often insufficient since, for example, not all resonances have been measured, especially for excited meson multiplets or for excited mesons and baryons containing heavy quarks. Therefore, a decay table has to be chosen, depending on the particular model used for the simulation. Furthermore, the underlying events need to be included, by means of a multi-parton interaction model. The modelling of the underlying events, the description of the parton shower, the hadronization and the subsequent hadrons decay, rely on a number of free parameters that need to be tuned in order produce simulations in good agreement with data. In high-energy physics there are three different types of tuning [73]:

- **Manual tuning**. This approach is done "by hand", it requires appropriate expertise and it is very slow. Moreover, this method can be used only for small parameter sets.

- **Brute-force tuning**. A large number of runs for each candidate configuration of parameters has to be performed, resulting in considerable run-times that make this method impractical for the estimation of a significant number of parameters.

- **Parameterization-based tuning**. This approach consists in calculating a function which describes the MC generator response depending on the parameters that need to be tuned, and then finding the best estimation of the parameters using a goodness-of-fit function.

3.4 Monte Carlo event generators

There are different types of Monte Carlo event generators: the *multi-purpose generators*, which include large collections of pre-computed matrix elements, implementation of the parton shower and of the hadronization model; *matrix-element generators*, that instead are capable of evaluating the matrix elements for a wide number of different processes, including Beyond Standard Model (BSM) processes, but they need to be interfaced with other generators to obtain the complete event reconstruction; *specialized generators*, for simulation of multi-parton processes or to simulate specific physical phenomena. The most widely used Monte Carlo event generators are now briefly described.

Pythia

PYTHIA is a multi-purpose program for generating high energy physics events at e^-e^+, pp and ep colliders [80]. The principal process that can be implemented are $2 \to 1$ and $2 \to 2$ processes, with some $2 \to 3$ processes also available, and the matrix elements information are interfaced with PYTHIA via the Les Houches Accord [81]. Processes with higher final-state multiplicity can be implemented if the particles arise from decays of resonances. Therefore, apart from the standard QCD scatterings, electroweak processes (including prompt photon production, single production of γ^*/Z and $W^\pm$ and pair production of weak bosons), charmonium, bottomium and top production, and Higgs processes can be included. Furthermore, different categories of BSM can be simulated, as the production of supersymmetric particles or new gauge bosons. In PYTHIA, the parton shower is based on the standard DGLAP evolution equations, accounting for ISR and FSR via appropriate algorithms, while the hadronization employs the string model. The generation of the events, especially as regards multiparton interactions and particles decay, relies on a set of parameters that have to be tuned in order to get a good agreement with data. The Pythia tuning is performed using the parameterization-based approach, by means of the PROFESSOR tuning system [82].

Herwig++

Herwig++, as Pythia, is a general-purpose event generator for the simulation of high-energy lepton-lepton, lepton-hadron and hadron-hadron collisions [83], based on the the previous Herwig (Hadron Emission Reactions With Interfering Gluons) event generators. The number of matrix elements for QCD and electroweak processes included in Herwig++ is relatively small, for that reason an interface to specialized matrix element generators is provided, via the Les Houches Accord. The parton shower evolution is obtained through the DGLAP equations and, in that part of the generation, the main difference with respect to Pythia is the treatment of the colour coherence [84], appearing in hard photoproduction processes (Figure 3.2). The hadronization is performed using the cluster method and the underlying events are implemented using an eikonal model [85] that represents them as additional semi-hard and soft partonic scatters. The free parameters on which the generator relies are tuned with the same method used by Pythia.

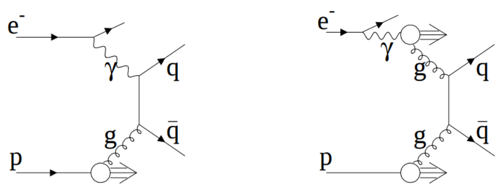

Figure 3.2: Examples of (left) direct and (right) resolved photoproduction.

MadGraph

MadGraph is a tool for automatically generating matrix elements for high energy physics processes, such as decays and $2 \to n$ scatterings [86]. It generates all the Feynman diagrams for a given process, provided the initial and the final state particles, and evaluate the matrix element for each point in the phase space. The diagrams generation is performed through the following steps:

- All the possible topologies associated to the process are generated, together with the appropriate number of external leg (i.e. Feynman propagators which have at least one end at an external vertex). Then, particles are assigned to external legs.
- The vertices are identified, with at most one unassigned line.
- All the lines in each vertex are scanned: if exist an interaction in the model which is able to accomodate the given line, the appropriate particle ID is assigned to it. When all the lines in the vertex are known, the diagram is complete and written to file. If there are no suitable interactions in the model, the topology is discarded and the algorithm goes to the next one.

The algorithm is optimized to only produce topologies that yield valid diagrams and, for a better efficiency, all the diagrams are generated in parallel. The evaluation of the matrix elements is performed by means of helicity wavefunctions, that allow to obtain expressions for amplitudes containing a large number of external legs [87]. The calculation can be obtained both at LO and NLO. The merging of the hard process with the parton shower and the subsequent hadronization are not implemented in MadGraph, that has to be therefore interfaced with Pythia or Herwig++ for a complete description of the events.

Sherpa

Sherpa [88] (Simulation of High-Energy Reactions of PArticles) is a Monte Carlo event generator that can be employ, besides lepton-lepton, lepton-hadron and hadron-hadron collisions, also in lepton–photon and photon–photon collision. Only a few $2 \to 2$ processes are included in the program and the internal Sherpa matrix-element generator is most usually employed. The parton shower (implemented with DGLAP equations) is matched with the matrix elements through the CKKW merging approach. The hadronization processes employ the cluster method, and the subsequent hadron decays rely on decay tables. The underlying events are generated by a multiple parton interactions algorithm, included in the generator.

3.5 V$\gamma\gamma$ Monte Carlo samples

The CMS 13 TeV MC samples used in the present analysis have been obtained with MadGraph5aMC@NLO, interfaced with Pythia 8 for parton shower. It combines in a unique framework all the features of MadGraph5 and of MC@NLO, providing LO and NLO for a many different processes, including BSM effects. The parton shower matching is performed by means of MLM for LO matrix elements, and of FxFx for NLO. The parameters related to the simulation of the hadronization and beam remnants are those obtained with the Monash tune [89], while other tunes related to multipartonic interactions, initial and final state radiations have been recently extracted using CMS data collected at a center of mass energy of 13 TeV [90]. One of the most important features of the MadGraph5aMC@NLO generator is that it allows to produce reweighted V$\gamma\gamma$ samples that incorporate anomalous coupling effects. The reweighting procedure consists in using only one sample of events generated under a certain theoretical hypothesis (the Standard Model), and associating with those events an additional weight that corresponds to a new theoretical hypothesis (the presence of anomalous gauge couplings); both the original and the additional weights are based only on matrix-element computations. The new weight W_{new}, corresponding to a new matrix element M_{new} is evaluated as follows:

$$W_{\text{new}} = \frac{|M_{\text{new}}|^2}{|M_{\text{orig}}|^2} W_{\text{orig}}.$$

The weights can be propagated through all of the simulation chain, avoiding performing a new simulation on an additional event sample. The new reweighted distributions can be therefore compared to theoretical predictions obtained by the Standard Model $V\gamma\gamma$ samples, in order to place the new expected limits on the anomalous couplings.

Chapter 4

The Large Hadron Collider and the CMS experiment

This chapter is dedicated to the Large Hadron Collider (LHC), to its main experiments and their goals. Amomg them, the Compact Muon Solenoid (CMS) experiment is more detailed presented, providing a brief description of its structure and of the detector's different components.

4.1 The Large Hadron Collider

The Large Hadron Collider [91] is the world's largest and most powerful particle collider. It operates at CERN (Conseil Europeen pour la Recherche Nucleaire), an organization for Particle Physics research, established in 1954 and located near Geneva, on the border between Switzerland and France. The LHC is a hadron and ion accelerator and collider that is running since September 2008. It is situated in a 26.7 km circular tunnel which was constructed between 1984 and 1989 for the Large Electron-Positron (LEP) collider and lies between 45 and 170 meters underground. The protons circulating in the LHC collider are supplied by a complex injection chain, as shown in Figure 4.1. First, proton are accelerated up to 50 MeV in the LINAC (LINear ACcelerator), then they enter the Proton Synchrotron Booster (PSB) to reach 1.4 GeV and finally the Super Proton Synchrotron (SPS) increases their energy up to 450 GeV before they are at last injected into the main ring. In the LHC, protons are grouped in 2808 *bunches*, each one constituted by $1.15 \cdot 10^{11}$ protons, and they travel at a distance of 7.5 meters from the others. They are accelerated, at 99,9999991% the speed of light, in two different beam pipes kept in ultra-high vacuum regime. The beams are focused by 392 magnetic quadrupoles distributed along the collider, and the circular trajectory is maintained by means of a 8.4 T magnetic field produced by 1232 superconductive 14.3 m long dipoles. Furthermore, the magnets needs to be kept at an operating temperature of 1.9 K, reached by means of 96 tonnes of superfluid helium-4. The collisions takes place

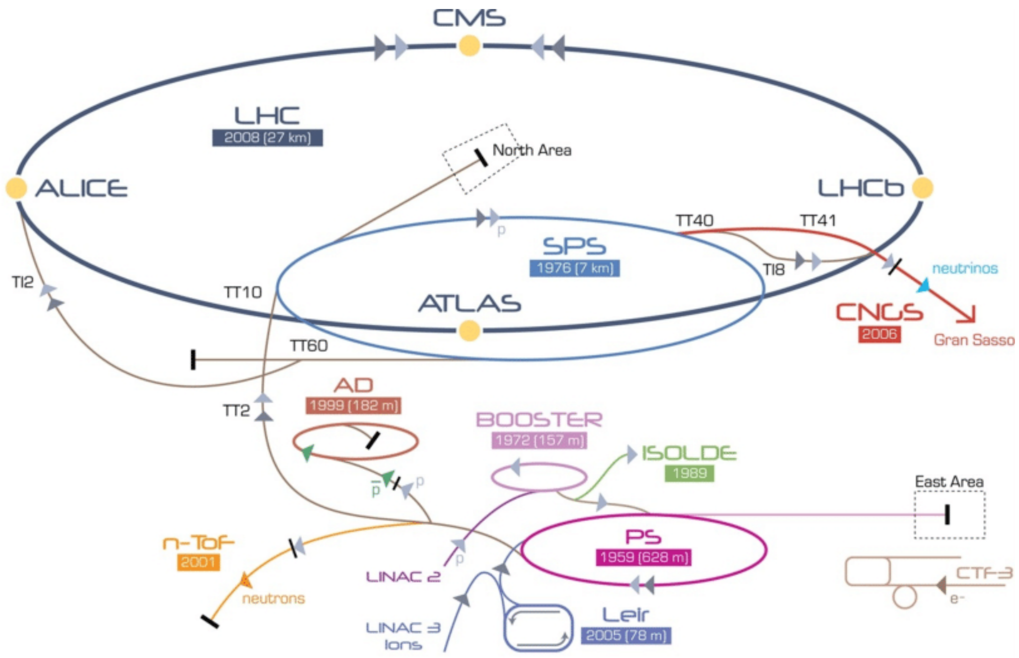

Figure 4.1: The injection chain for the Large Hadron Collider.

in four interaction points along the ring, and in correspondence of them there are the four main experiments, always shown in Figure 4.1:

- ATLAS [92] (A Toroidal LHC ApparatuS) that is a general-purpose detector whose aim is to study high-energy pp collisions in order to do precise tests on the Standard Model and to investigate new physics phenomena.
- CMS [93] (Compact Muon Solenoid) is the other large general-purpose detector at LHC, that will be described in detail in Section 4.2. Together with ATLAS, the CMS detector discovered the Higgs boson in July 2012.
- LHCb [94] (Large Hadron Collider beauty) that is a dedicated b-physics experiment, designed primarily to measure the parameters of CP violation in the decay of charm and beauty hadrons. The LHCb detector is a single-arm forward spectrometer, since the beauty hadrons at high energies are mostly produced in the same forward or backward cone.
- ALICE [95] (A Large Ion Collider Experiment) is optimized to study heavy-ion (Pb-Pb nuclei) collisions, and it is focused on physics of strong interactions at very high energy and density. One of its aims is to verify the existence of the quark-gluon plasma, whose properties would be crucial for the understanding of many quantum chromodynamics aspects as, for example, the color confinement.

The collision rate at LHC is 40 MHz, that means that the interactions take place every 25 ns. The LHC was designed to collide protons at a center-of-mass energy of 14 TeV with a peak instantaneous luminosity L = $10^{34}\text{cm}^{-2}\text{s}^{-1}$. For a process of cross section σ the instantaneous luminosity is defined as

$$L = \frac{\mathrm{d}N}{\mathrm{d}t} \cdot \frac{1}{\sigma} \, .$$

In order to express the size of the collected data, the integrated luminosity $\int L\mathrm{d}t$ is used, measured in inverse of barns. The luminosity depends on the beam parameters and can be written as

$$L = \frac{N_b^2 \, n_b \, f_{rev} \gamma_{rev}}{4\pi \, \epsilon_n \, \beta^*} F$$

where N_b is the number of protons in each bunch and n_b the number of bunches per beam. f_{rev} is the revolution frequency, γ_r is the Lorentz factor, ϵ_n the normalized transverse beam emittance and β^* is the amplitude function at the collision point. F is the geometric luminosity reduction factor due to the crossing angle θ_C at the interaction point

$$F = \left(1 + \left(\frac{\theta_C \sigma^z}{2\sigma^*} \right)^2 \right)^{1/2}$$

where σ^z and σ^* are the r.m.s. bunch length and the transverse r.m.s. beam size at the interaction point respectively.

4.2 The Compact Muon Solenoid experiment

The Compact Muon Solenoid (CMS) experiment is one of the two general-purpose experiments installed at LHC. It is located near Cessy, in France, at the interaction point 5 along the LHC ring, about 100 meters underground. It was conceived to study the high-energy, high-luminosity proton-proton collisions and it has a wide number of research lines, from precision measurements of Standard Model parameters and study of the Higgs boson properties to investigation of new beyond Standard Model physics, extra dimensions and dark matter. The CMS detector has a cylindrical structure, symmetrical around the interaction point, and can be divided into two regions: the *barrel* represents the central part and is coaxial with the beamline, and two *endcaps* close the central part on both sides. It can be described as a series of concentric sub-detectors, each one with a specific function. Starting from the inner one they are: the silicon tracker, the electromagnetic calorimeter, the hadron calorimeter, and the muon chambers. The latters are placed inside the return yoke of the superconducting solenoid magnet, that produces a magnetic field of 3.8 T. The whole structure has a length of 21.6 m and a diameter of 14.6 m and weights 12500 t. The CMS structure is shown in Figure 4.2, and the sub-detectors are here briefly listed.

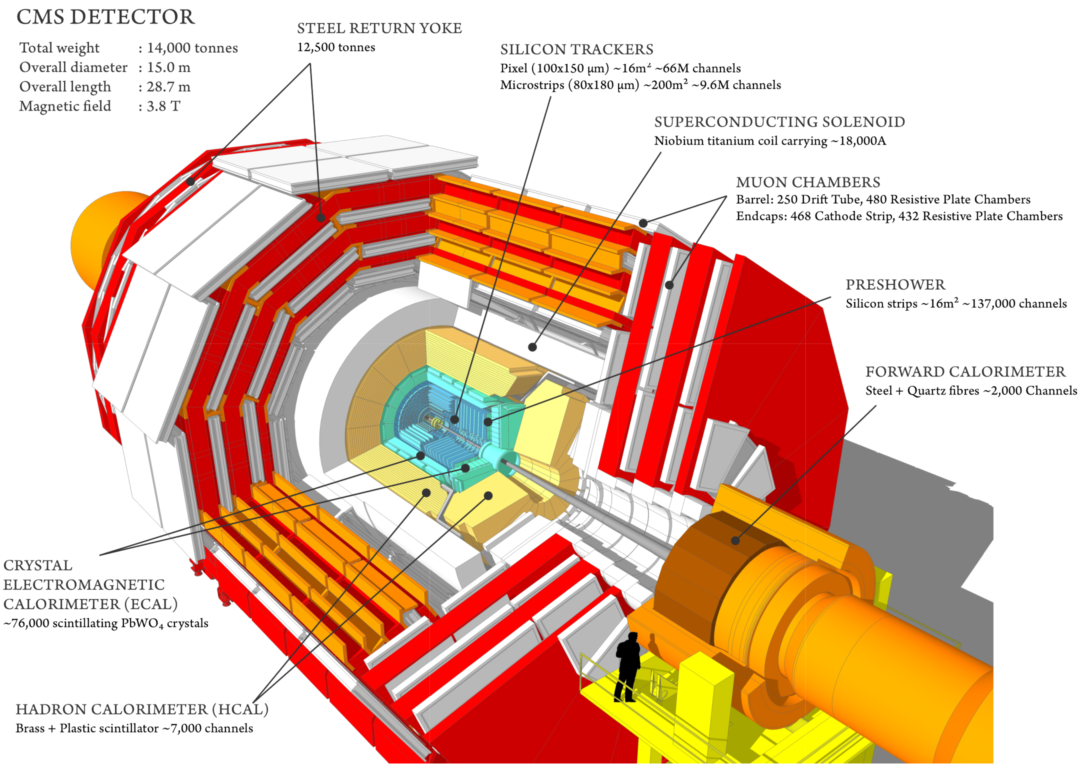

Figure 4.2: The CMS detector structure.

4.2.1 The inner tracking system

The inner detector is the tracker [96], whose aim is to measure the track and the momentum of charged particles with the highest precision and to reconstruct the secondary vertices. It is fully immersed in the magnetic field produced by the solenoid and it has 5.8 m length and 2.6 m diameter. It is placed in the inner detector region to receive particles that interacted less with the detector materials and it is built in order to interfere with the particles trajectory as little as possible. Silicon detectors are here used to obtain a high granularity and a fast response. The tracking system is composed by *pixels* and *microstrips*, with a total active area of 215 m^2 and a 95% efficiency of electron and muon tracks reconstruction. The pixel detector is made of three barrel layers with radius between 4.4 and 10.2 cm and the endcaps are made by 3 disks. The microstrip tracker has two barrel sections: the inner barrel with 4 layers and the outer barrel with 6 detection layers, with radius up to 1.1 m, and two endcaps with 3 plus 9 disks on each side of the barrel.

4.2.2 The Electromagnetic Calorimeter

The Electromagnetic Calorimeter [97] (ECAL) measures the energy of electrons and photons that are produced in the electromagnetic shower. It is a hermetic

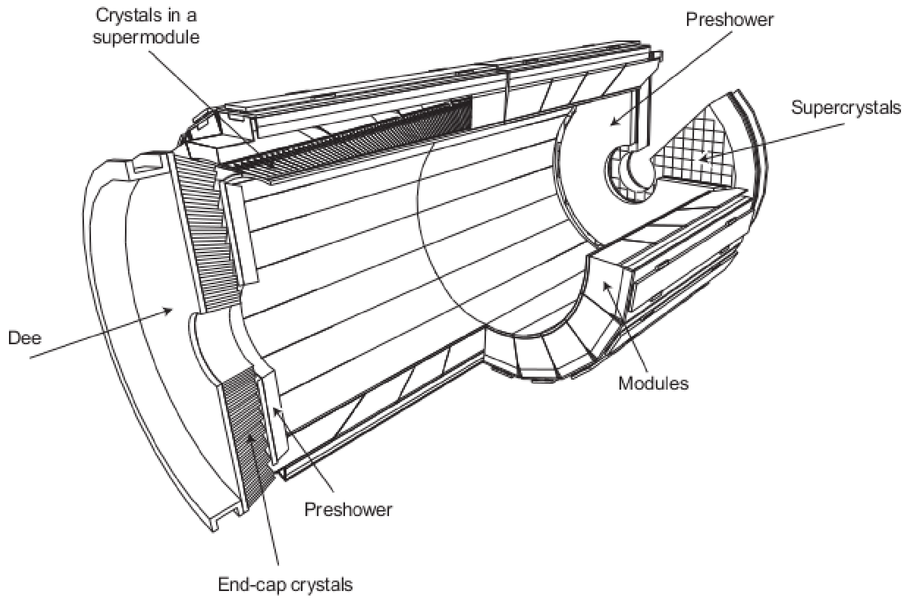

Figure 4.3: Schematic view of the ECAL calorimeter

homogeneous calorimeter made of lead tungstate ($PbWO_4$) scintillating crystals: 61200 in the barrel and 7324 in each of the endcaps. The lead tungstate has a high density (ρ = 8.28 g/cm^3), a short radiation length (X_0 = 0.89 cm) and a small Moliere radius (RM = 2.2 cm), characteristics that make this material ideal to built a compact detector with high granularity. ECAL also contains preshower detectors in front of the endcaps, constituted of lead radiators and silicon strips. They allow CMS to discriminate between single high-energy photons and collinear pairs of low-energy photons deriving from neutral pion decays. The energy resolution in ECAL can be written as

$$\frac{\sigma_E}{E} = \frac{S}{\sqrt{E}} \otimes \frac{N}{E} \otimes C = \frac{2.8\%\ \mathrm{GeV}^{1/2}}{\sqrt{E}} \otimes \frac{0.12\ \mathrm{GeV}}{E} \otimes 0.3\%.$$

where S is the stochastic term, N the noise term and C the constant term. Their values are extracted from beam test measurements. A sketch of the section of the ECAL calorimeter is shown in Figure 4.3.

4.2.3 The Hadronic Calorimeter

The Hadron Calorimeter [98] (HCAL) measures the energy of hadrons, providing also measurements of missing-transverse-energy due to the production in the collision of undetected particles, like neutrinos or exotic particles. HCAL is a hermetic sampling calorimeter divided in four sections: barrel (HB), endcaps (HE), outer hadron calorimeter (HO) and forward hadron calorimeter (HF), covering different space regions. HB, HE and HO are made of brass absorber layers alternated

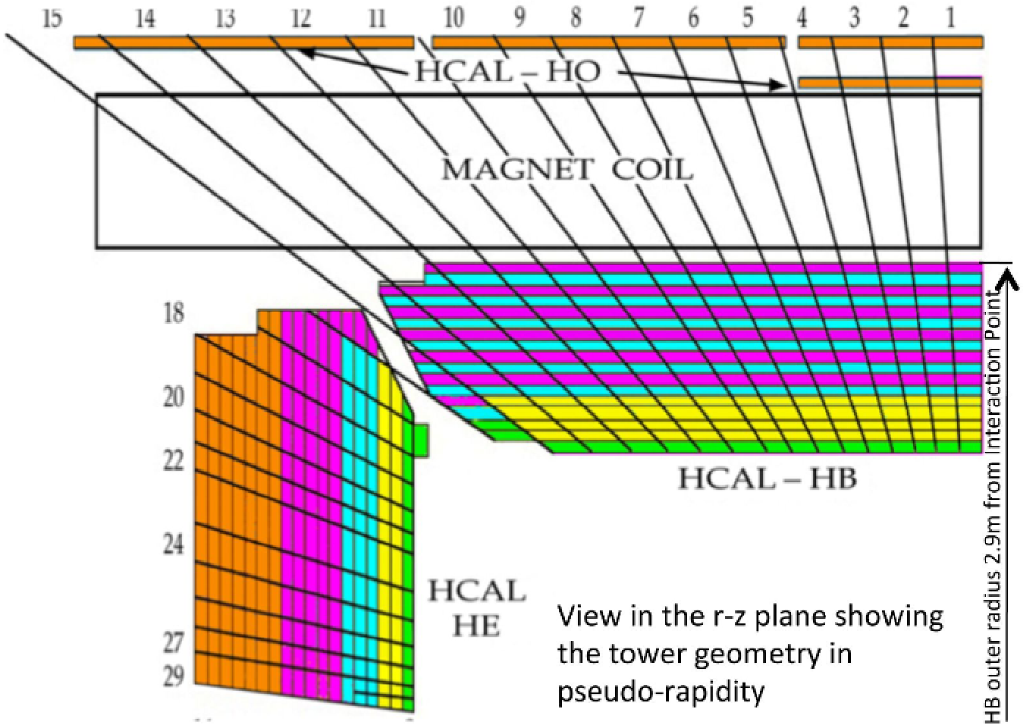

Figure 4.4: A schematic side view of the HCAL calorimeter.

with plastic scintillators as active medium, while HF, that covers the region with the highest particle flux, is made of steel plates with quartz fibres as active medium. The energy resolution for a single neutral pions, determined by beam tests, is

$$\frac{\sigma_E}{E} = \frac{100\%\ \mathrm{GeV}^{1/2}}{\sqrt{E}} \otimes 0.8\%$$

A sketch of the section of the HCAL calorimeter is shown in Figure 4.4.

4.2.4 The Superconducting Solenoid

The Superconducting Solenoid magnet [99] is constituted by a series of refrigerated superconducting niobium-titanium coils, and it is 13 m long and 6 m in diameter. It provides a magnetic field of 3.8 T that deviates the charged particles trajectory, to allow measurement of their momenta through their trajectory curvature in the field. The *return yoke* of the superconducting solenoid has a diameter of 14 m and it allows through only muons and weakly interacting particles, as neutrinos.

4.2.5 The Muon chambers

Due to their minimum energy loss in the matter, muons are not stopped by any of CMS's calorimeters and they are detected in the muon chambers [100], placed

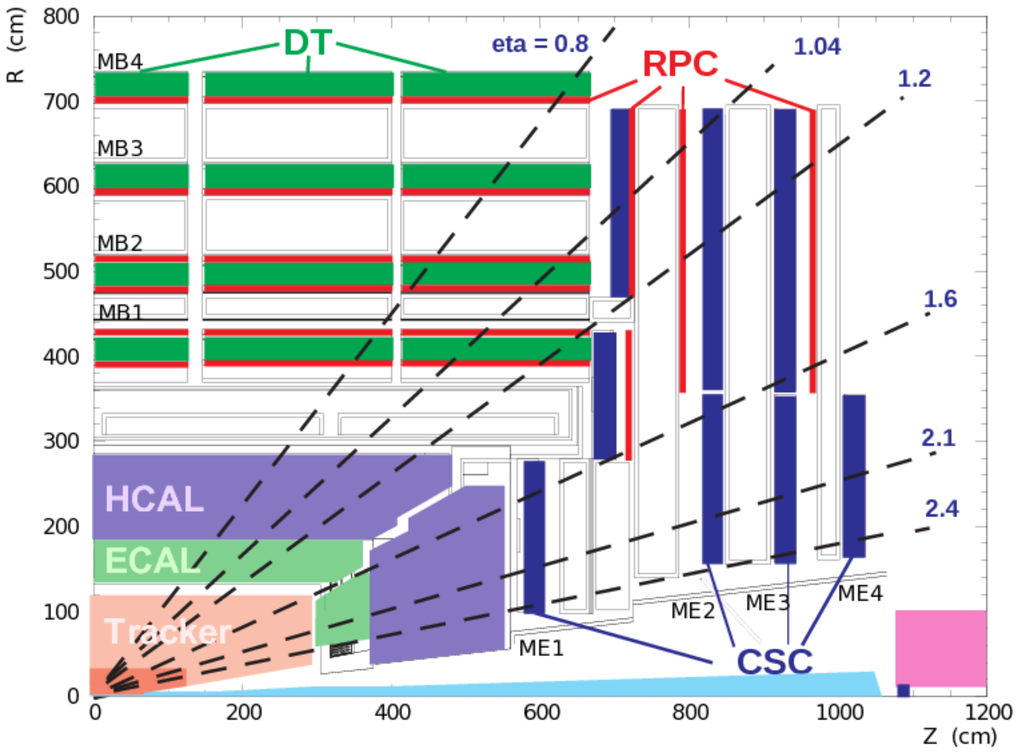

Figure 4.5: Layout of one quadrant of CMS. The four DT stations in the barrel, the four CSC stations in the endcap, and the RPC stations are shown.

in the outermost part of CMS. The muon system is made of three different types of gaseous detectors: drift tube chambers (DT) in the barrel, cathode strip chambers (CSC) in the endcaps, and resistive plate chambers (RPC) in both the regions. Each DT chamber contains 60 tubes, it measures on average 2m x 2.5m in size, and is made of 12 aluminium layers, arranged in three groups of four. The cathode strip chambers are made of arrays of positively-charged “anode” wires crossed with negatively-charged copper “cathode” strips, placed inside a gas volume. The resistive plate chambers consist of two parallel plates, one positively charged anode and one negatively charged cathode; they are both made of plastic material and they are separated by a gas volume. The layout of the muon chambers is shown in Figure 4.5.

Chapter 5

Characterization of the $V\gamma\gamma$ phase space at 13 TeV

In this chapter, the differential cross section distributions are obtained from $W\gamma\gamma$ and $Z\gamma\gamma$ samples. In the first part of this chapter the characterization of the $V\gamma\gamma$ phase space on 13 TeV Monte Carlo (MC) samples is presented. The characterization of the phase space is needed to extract from the global phase space of all the final state particles a fiducial region that includes genuine $V\gamma\gamma$ events. For this purpose, some selections on physical observables are applied on the $V\gamma\gamma$ events, by means of the Rivet software, whose description is also provided in this chapter. The CMS data and MC processing chain are briefly described in the second part of the chapter, together with the $V\gamma\gamma$ sample data format. To verify the reliability of the Rivet routine implemented for the characterization of the phase space, the obtained distributions are compared to those extracted, without using Rivet, from a different data format.

5.1 Rivet

Rivet [101] (Robust Independent Validation of Experiment and Theory) is an object-oriented C++ framework for validation and tuning of Monte Carlo event generators, and for comparisons between data and Monte Carlo. It stores a wide number of analysis and it can be used by LHC and other high-energy collider experiments, since it is generator and experiment independent, and it operates on HepMC Events [102]. The HepMC Event Record describes particles and vertices involved in a high-energy collision as edges and nodes of a graph, as shown in Figure 5.1. In that way, multiple collisions can be handled as a super-position of many, non-connected graphs. An event is a container of all vertices, each of them associated with the list of incoming and outgoing particles. Particles are described by the Lorentz vector and the polarisation information; the PDG particle identifier code, name, charge, mass, lifetime and spin are also stored in the event. In the analysis, the FIFO (first-in, first-out) method is used to stream the HepMC events. The main objects employed in Rivet are the *projections*. Projections are able to calculate properties from an event. Such properties can be single numbers, a single complex objects (a vector or a tensor) or even lists of such objects. As an example, the `FinalState` projection provides a list of stable, physical particles for each event. Every Rivet analysis must implement at least three methods: `init()`, `analyze()` and `finalize()`. In the first one, histograms are booked and projections are added to the analysis; the second one loops over all the events to select particles according to the chosen selections, construct observables and fill histograms; in the third one the histograms are normalized. The histogramming is performed using the YODA (Yet more Objects for Data Analysis) system. Among its features, YODA includes proper treatment of irregular bin widths, gaps, overflows/underflows and weights, and histograms reweighting up to second-order correlations.

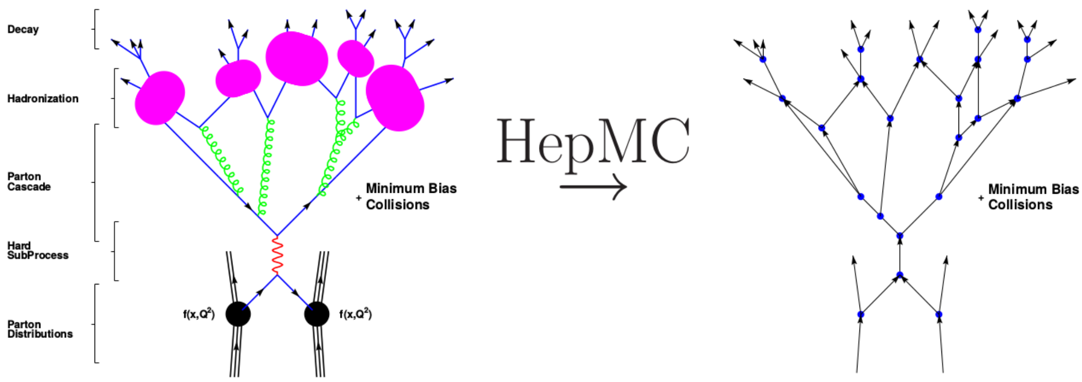

Figure 5.1: Graph structure of an HepMC event (left) compared to the structure of a high-energy collision (right) [102].

5.2 Characterization of the V$\gamma\gamma$ phase space

The characterization of the phace space provides a fiducial region for the signal processes, within which the cross section measurements are performed. It is a fundamental step to extract the correct information from the outcome of the collisions and to avoid misidentification of the process under study. In this analysis, the characterization of the V$\gamma\gamma$ phace space is performed on 13 TeV CMS MC distributions obtained with MadGraph5aMC@NLO interfaced with Pythia 8 for parton shower. In Figure 5.3 and Figure 5.4, the event display of a pp $\rightarrow$ Z($\rightarrow \mu^-\mu^+$)$\gamma\gamma$ and pp $\rightarrow$ W($\rightarrow \mu\nu_\mu$)$\gamma\gamma$ simulated processes are respectively shown. Two MC samples are used, generated in order to study the W$\gamma\gamma$ production and the Z$\gamma\gamma$ production, separately. The selections applied on MC are equal to those applied on data, in order to obtain comparable distributions. The differential cross section distributions are then produced, as functions of different physical observables of the processes of interest (momentum, mass).

5.2.1 Preliminary selections

The coordinate system adopted at the LHC is a cylindrical right-handed system (Figure 5.2), with the origin placed in the collision point. The z-axis follows the beam direction, the x-axis points to the center of the LHC rings while the y-axis points upward and it is perpendicular to the beam direction. The radial coordinate in the x-y plane, corresponding to the distance from the z-axis, is denoted by r. The polar angle θ is measured from the positive z-axis and the azimuthal angle ϕ is measured from the positive x-axis in the x-y plane. To describe the angle of a particle with respect to the beam axis, the pseudorapidity η is introduced as $\eta \equiv -\ln\left[\tan\left(\theta/2\right)\right]$. Pseudorapidity is preferred over θ since η differences are invariant under boosts along the longitudinal axis. Hadronic collisions are not collisions

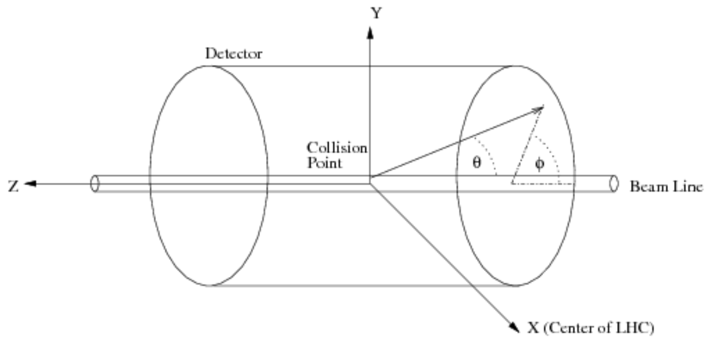

Figure 5.2: The CMS coordinate system.

amongst point particles, which implies that the z-component of the momentum, i.e. the longitudinal momentum, is not conserved. However, the momentum in the transverse plane is conserved and for that reason, in the analysis, transverse quantities are mostly used. The first selections applied are on η and transverse momentum p_T. Leptons and photons are required to have $p_T >$ 15 GeV and 20 GeV respectively, corresponding to the minimum threshold with which lepton- and photon-candidates are reconstructed in the detector and then recorded. Furthermore, only prompt (i.e. not originating from hadron decays) and stable photons are

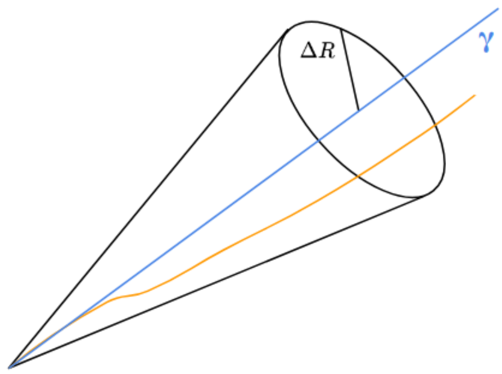

Figure 5.5: Isolation cone for photons.

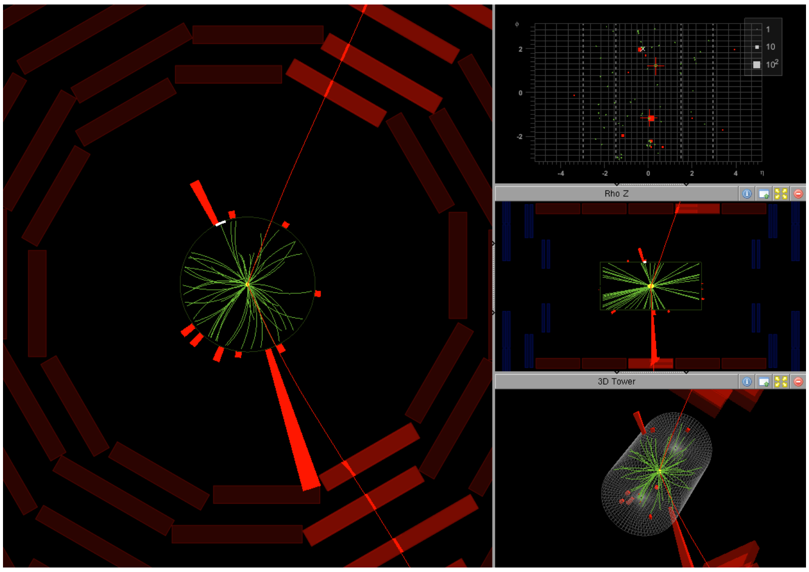

Figure 5.3: Event display of a pp $\rightarrow$ Z($\rightarrow \mu^{-}\mu^{+}$)$\gamma\gamma$ MC event reconstructed in the CMS detector. The muon pair is identified by the two tracks in the muon chamber, in the external part of the detector. In the inner part of the detector, the green lines are associated to electromagnetic activity while the bright red structure to hadronic activity. On the left the reconstructed event projection on the R-ϕ plane is shown. On the right, from top to bottom, the *lego* projection on the $\eta - \phi$ plane, the projection on the R-z plane and the 3D detector representation are shown.

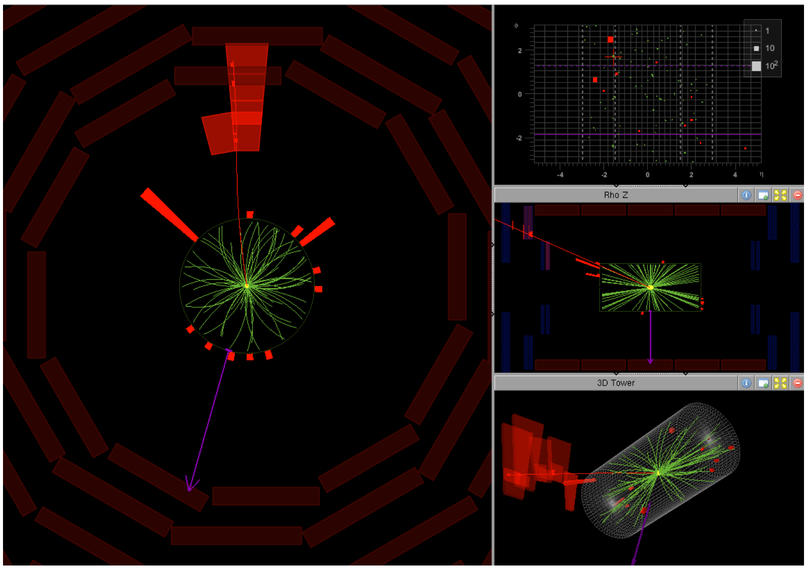

Figure 5.4: Event display of a pp $\rightarrow$ W($\rightarrow \mu\nu_{\mu}$)$\gamma\gamma$ MC event reconstructed in the CMS detector. The muon is identified by the tracks in the muon chamber, in the external part of the detector, and the undetected neutrino is here pictured as a violet arrow.

selected. In both cases pseudorapidity is required to be, in module, less than 2.4. This selection corresponds to the region of pseudorapidity covered by the CMS muon system. Since the aim of the characterization of the phase space is to identify genuine V$\gamma\gamma$ events, isolation selections are applied in order to avoid mistaking initial or final state radiation photons for photons coming from the vertex of interest. An isolation cone with radius $\Delta R = \sqrt{(\Delta\eta)^2 + (\Delta\phi)^2}$ is drawn around the photon direction (Figure 5.5). If a lepton is found in the cone of radius 0.4, or a parton is found in the smaller cone of radius 0.1, the photon is rejected. Another important element that has to be considered is the presence of electrons and muons coming from the leptonic decay of the τ, which are filtered at the beginning of the events selection.

5.2.2 Characterization of the W$\gamma\gamma$ and Z$\gamma\gamma$ phase space

Events selected for the W$\gamma\gamma$ analysis must have one muon or electron and at least two isolated photons. An additional cut on the transverse momentum of the leptons is implemented, requiring $p_T > 30$ GeV for muons and $p_T > 35$ GeV for electrons. No lower constraints are applied on the missing transverse energy (MET) of the neutrino, defined as the magnitude of $p_T^{miss} = -\sum_i p_T^i$, where the sum is performed over all the particles detected in the event. The transverse mass of the W boson, defined as

$$m_T = \sqrt{2p_T^{\ell} p_T^{miss}\left\{1 - \cos\left[\phi(\mathbf{p_T^{\ell}}) - \phi(\mathbf{p_T^{miss}})\right]\right\}}$$

is required to be greater than 40 GeV and it is expected to peak at approximately 80 GeV. The transverse momentum of the lepton and of the undetected neutrino are denoted with p_T^{ℓ} and p_T^{miss}, respectively. On data distributions this selection is applied in order to remove background not having genuine p_T^{miss}, for example diphoton events with a fake lepton. Events selected for the Z$\gamma\gamma$ analysis must have two electrons or muons of opposite charge and at least two photons. The leading lepton, i.e. the most energetic lepton of the pair, is required to have a transverse momentum greater than 35 GeV for the electrons or 30 GeV for the muons. The reconstructed dilepton mass

$$m_{\ell\ell} = \sqrt{m_{\ell^+}^2 + m_{\ell^-}^2 + 2\left(E_{\ell^+}E_{\ell^-} - p_{\ell^+}p_{\ell^-}\cos\theta\right)}$$

is required to be greater than 51 GeV and smaller than 131 GeV. Such selection is applied to data to remove backgrounds that have low dilepton invariant masses. In the Rivet analysis, the bosons are reconstructed by means of the two projections `WFinder` and `ZFinder`. They take as inputs: the total list of particle found in the event through the `FinalState` projection; the particle code, to specify if the decay is via electrons or muons; the leptons selections on p_T and η; the minimum and maximum values of the reconstructed mass (or transverse mass), and

Definition of the W$\gamma\gamma$ fiducial region
$p_T^{\gamma} > 20$ GeV, $\lvert\eta^{\gamma}\rvert < 2.4$
$p_T^{e} > 35$ GeV, $\lvert\eta^{\gamma}\rvert < 2.4$
$p_T^{\mu} > 30$ GeV, $\lvert\eta^{\gamma}\rvert < 2.4$
One candidate lepton and two candidate photons
$m_T > 40$ GeV
$\Delta R(\gamma,\gamma) < 0.4$ and $\Delta R(\gamma,\ell) < 0.4$
$\Delta R(\gamma,q) < 0.1$ and $\Delta R(\gamma,\mathrm{g}) < 0.1$
Definition of the Z$\gamma\gamma$ fiducial region
$p_T^{\gamma} > 20$ GeV, $\lvert\eta^{\gamma}\rvert < 2.4$
$p_T^{\ell} > 15$ GeV, $\lvert\eta^{\gamma}\rvert < 2.4$
Two oppositely charged candidate leptons and two candidate photons
leading $p_T^{e} > 35$ GeV
leading $p_T^{\mu} > 30$ GeV
$51 < m_{\ell\ell} < 131$ GeV
$\Delta R(\gamma,\gamma) < 0.4$, $\Delta R(\gamma,\ell) < 0.4$ and $\Delta R(\ell,\ell) < 0.4$
$\Delta R(\gamma,q) < 0.1$ and $\Delta R(\gamma,\mathrm{g}) < 0.1$

Table 5.1: Fiducial region definitions for the W$\gamma\gamma$ analysis and Z$\gamma\gamma$ analysis.

the maximum ΔR value for photons around charged leptons, which is chosen to be 0.1. Photons with $\Delta R < 0.1$ are taken into account for the so-called leptons *dressing*, that consists in adding to leptons energy the energy of the photons that may have been emitted through initial or final state radiation. The selections applied are summarized in Table 5.1, and the obtained distribution are listed in Table 5.4.

5.3 Event processing chain at CMS

Production of MC samples is performed in the CMSSW framework, a collection of software for collision data and MC analysis. The CMSSW event processing

Observable	Figure	Observable	Figure
p_T leading lepton	5.6	p_T leading lepton	5.12
p_T leading photon	5.7	p_T subleading lepton	5.13
p_T subleading photon	5.8	p_T leading photon	5.14
Diphoton p_T	5.9	p_T subleading photon	5.15
W transverse mass	5.10	Diphoton p_T	5.16
Diphoton mass	5.11	Diphoton mass	5.17
		Z mass	5.18
		Z$\gamma\gamma$ mass	5.19

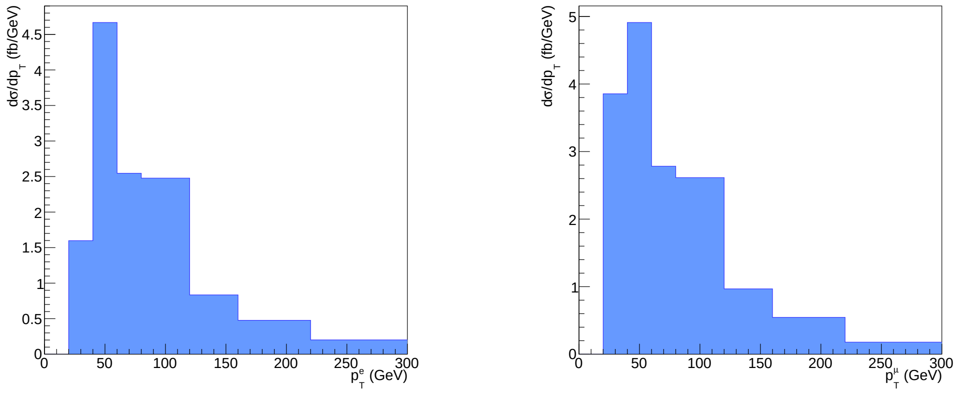

Figure 5.6: Transverse momentum of the W decay electron (left) and muon (right).

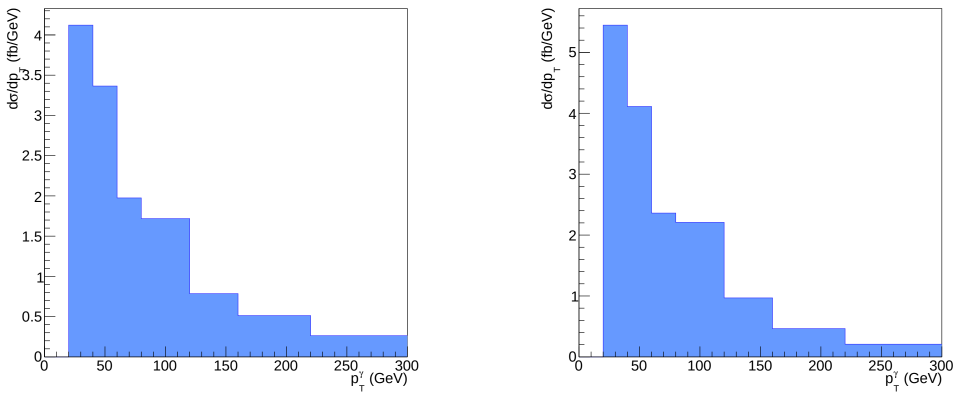

Figure 5.7: Transverse momentum of the leading photon of the W$\gamma\gamma$ vertex for the electronic (left) and muonic (right) W decay.

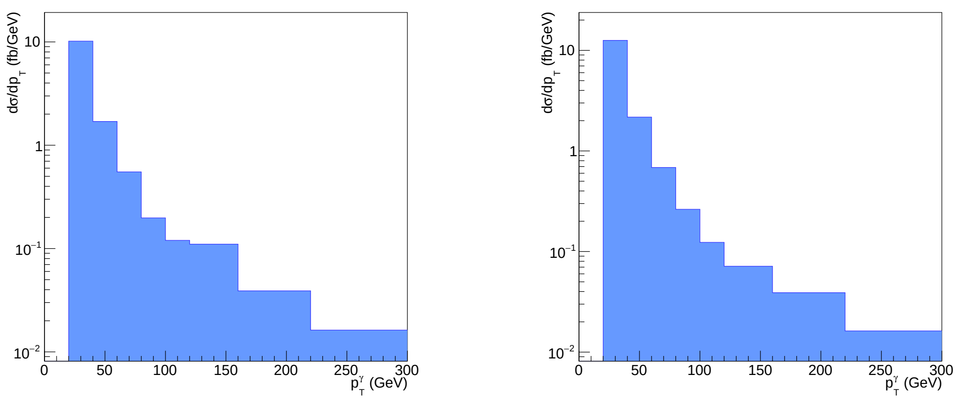

Figure 5.8: Transverse momentum of the subleading photon of the W$\gamma\gamma$ vertex for the electronic (left) and muonic (right) W decay.

model consists of one executable, called `cmsRun`, and different modules containing all the instructions needed for such processing, as reconstruction or filtering

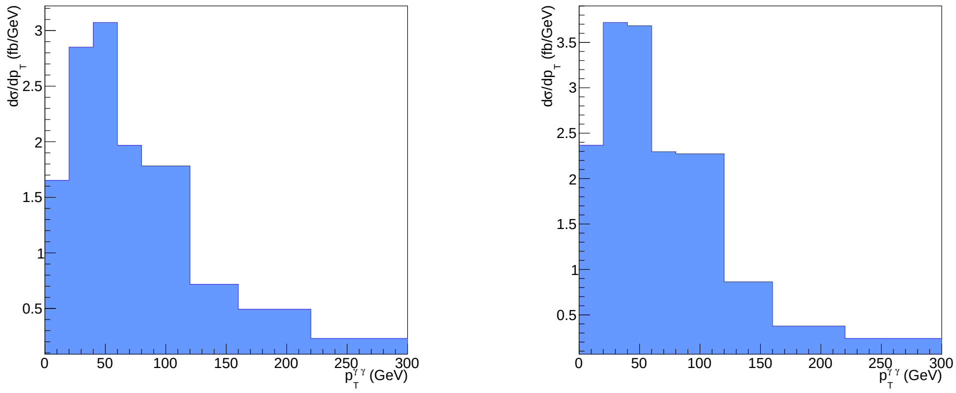

Figure 5.9: Diphoton transverse momentum for the electronic (left) and muonic (right) W decay.

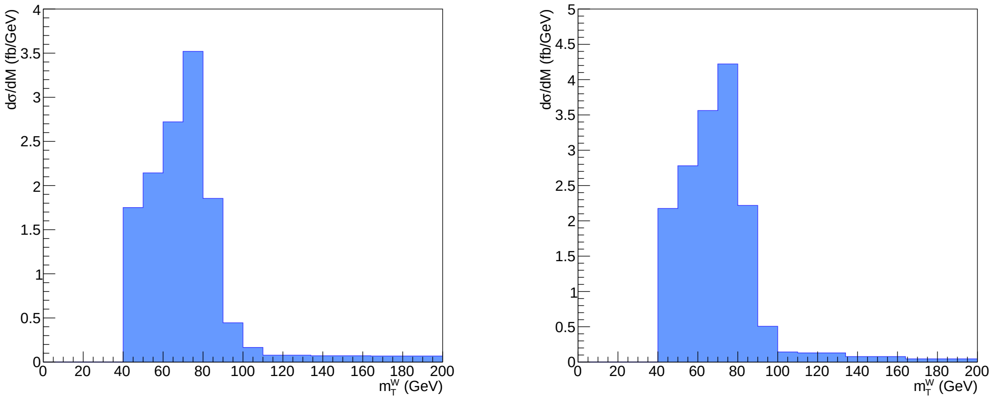

Figure 5.10: W transverse mass for the electronic (left) and muonic (right) W decay.

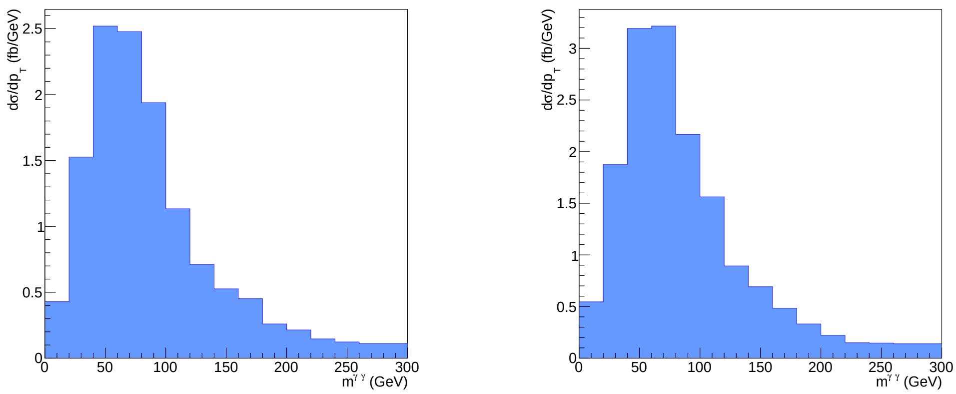

Figure 5.11: Diphoton mass for the electronic (left) and muonic (right) W decay.

algorithms. It handles data (and MC) information through the Event Data Model (EDM), which is centered around the concept of an *Event*. An Event is a C++ object container for all the data collected in a collision, that can thus be accessed only via

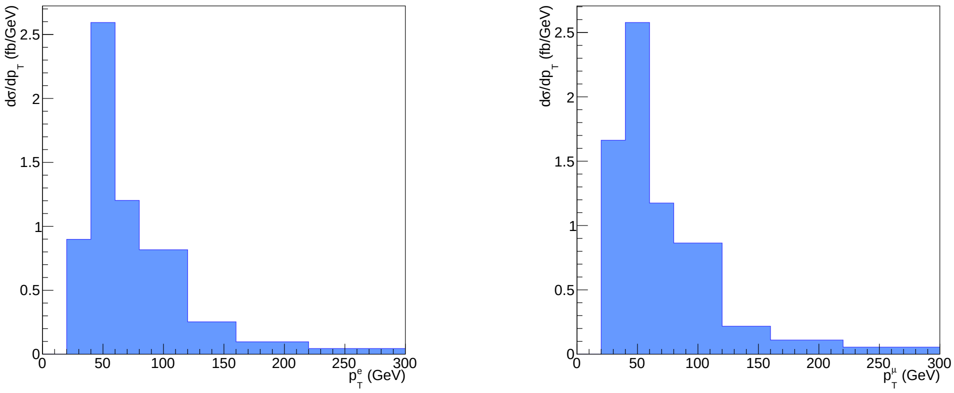

Figure 5.12: Transverse momentum of the leading Z decay electron (left) and muon (right).

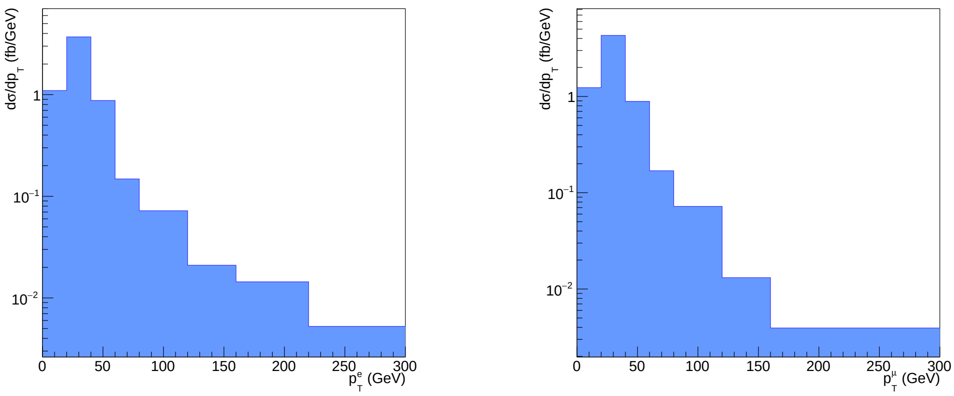

Figure 5.13: Transverse momentum of the subleading Z decay electron (left) and muon (right).

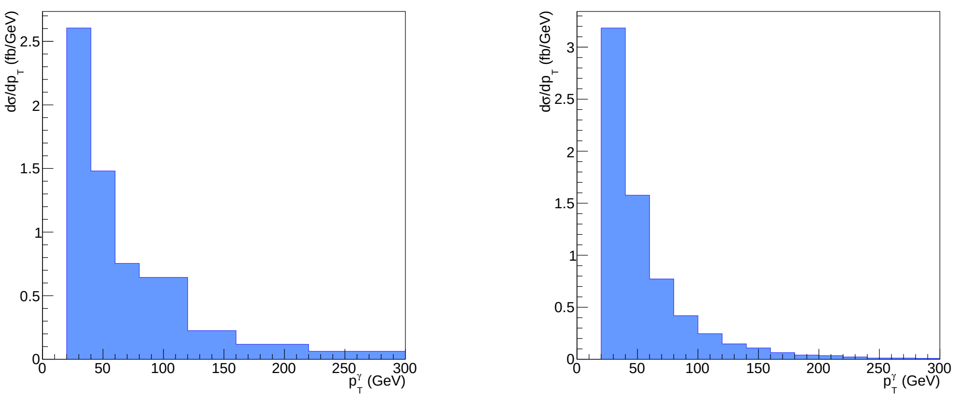

Figure 5.14: Transverse momentum of the leading photon of the $Z\gamma\gamma$ vertex for the electronic (left) and muonic (right) W decay.

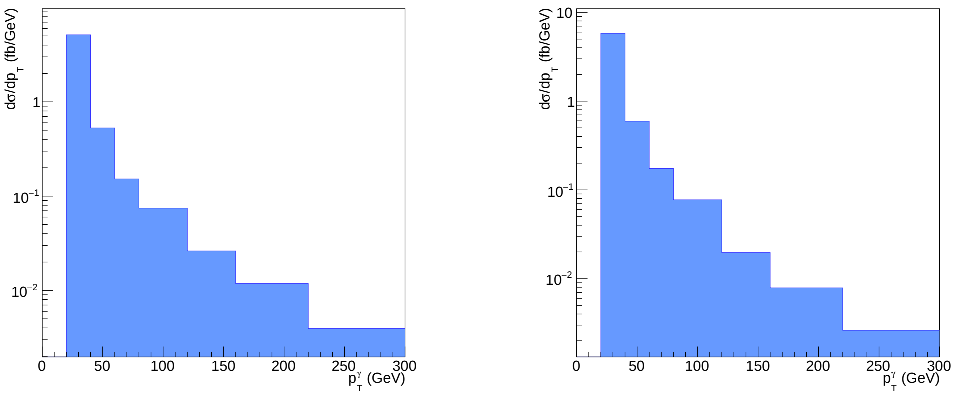

Figure 5.15: Transverse momentum of the subleading photon of the W$\gamma\gamma$ vertex for the electronic (left) and muonic (right) W decay.

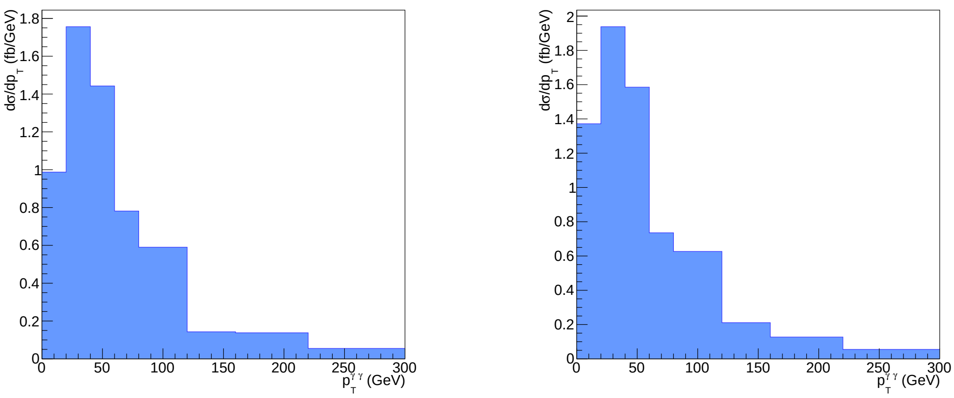

Figure 5.16: Diphoton transverse momentum for the electronic (left) and muonic (right) Z decay.

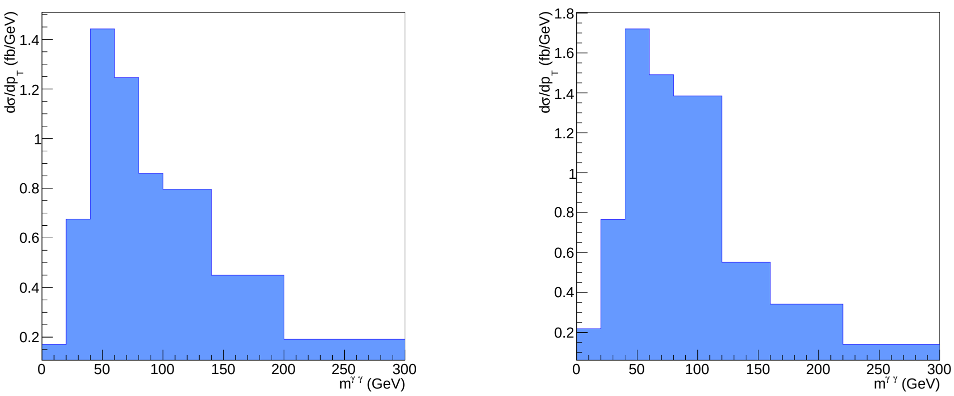

Figure 5.17: Diphoton mass for the electronic (left) and muonic (right) Z decay.

Event. In software terms, an Event starts when a collection of RAW data from the detector are stored in memory, in a single container called `edm::Event`. The

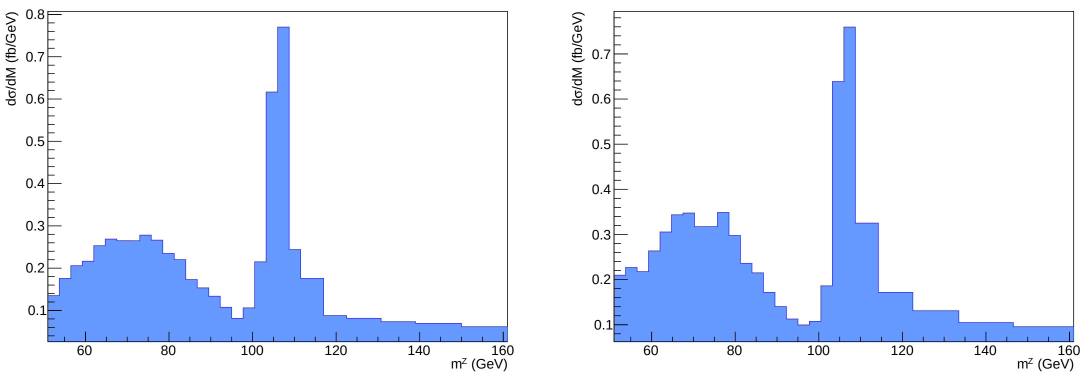

Figure 5.18: Reconstructed Z mass in the electronic (left) and muonic (right) channel. Both distributions show on the left the contribute of to the final state radiation photons, that lead to leptons reconstructed with less energy.

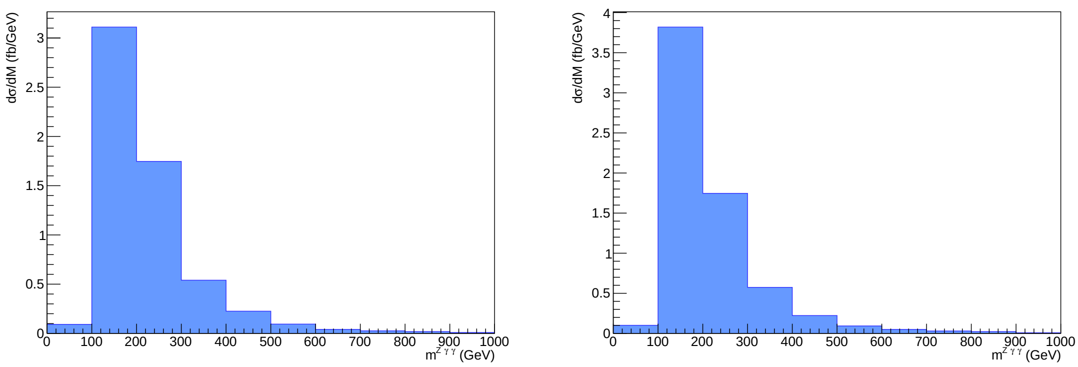

Figure 5.19: Reconstructed $Z\gamma\gamma$ mass in the electronic (left) and muonic (right) channel.

RAW data consist of DAQ (Data AcQuisition) information (detector element hits, for example), and they are not used directly for analysis. The data are then processed by an event reconstruction algorithm (Figure 5.20), which is designed to perform the following operations:

1. Detector-specific processing: the RAW data from the detector are unpacked and cluster and hit objects are reconstructed.
2. Tracking: the charged-particles tracks are built using pattern recognition algorithms and information from the hits recorded in the tracker layers.
3. Vertexing: primary and secondary vertices are reconstructed. Charged-particle tracks may be share a secondary vertex, being linked together.
4. Particle identification: the Particle-Flow algorithm [103] employs information from all the detector layers to identify each final-state particle candidate and to retrieve particle properties on the basis of such identification.

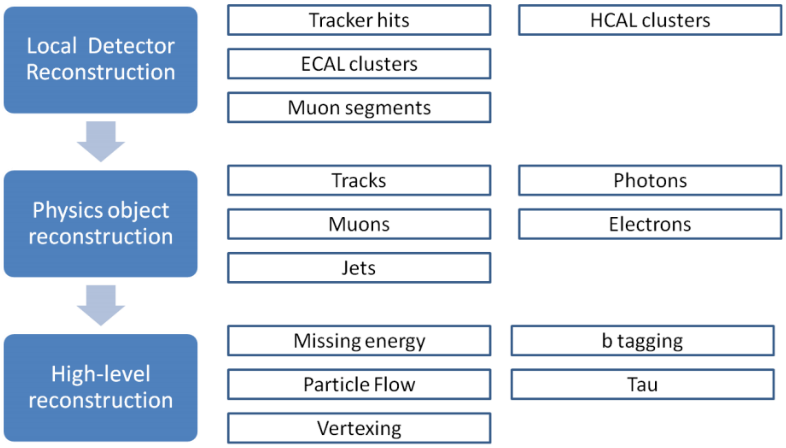

Figure 5.20: Summary of the reconstruction sequence of the CMS reconstruction algorithm.

The reconstructed (RECO) data are also stored in the Event. The processing of MC samples is slightly different from data, since the production of simulated events requires some additional steps to be compared with data [104]:

1. wmLHE: simulation of the hard scattering by specialised event generators, resulting in events written in LHE format.
2. Generation: parton shower, hadronization and hadron decays are implemented in the simulation in order to obtain the collection of the final-state particles which propagate from the collision point towards the CMS detector. At this level, the event format is called GEN.
3. Simulation: the final state particles interacts with the CMS detector and a set of simulated hits and clusters are recorded in the SIM event format.
4. Digitisation: the CMS front-end electronics is replicated and the digital information gathered is the same that would be obtained if it was raw data acquired by the real experiment. The event format is here called DIGI.

The reconstruction of the simulated events is performed in the same methods used for data. In principle the RECO data can be used for the analysis, but they contain very detailed information that make this format too big for frequent use, especially for large data samples. Therefore, the more compact and workable AOD (Analysis Object Data) are extracted from the RECO, in order to provide more manageable data for physics analyses. All the high-level physics objects (leptons, photons, jets and MET) are included in the AOD, together with a summary of the RECO information to allow the typical analysis actions, as the track refitting. However, due to its limited size, the AOD does not support some procedures (recalibration or application of new pattern recognition techniques) and in these cases the RECO or RAW data are required. For the LHC Run 1, from 2010-2012, the total size of AOD stored by CMS was about 20 Petabytes. Since the Run 2, from 2015-2018, has produced an amount of data ten times larger that would exceed the available storage resources, a new data format has been designed, called Mini-AOD [105], with the following features:

- It extract only necessary information from existing data formats, using the minimum amount of space.
- It is adaptable to a wide variety of CMS physics analysis and it supports novel analysis techniques and re-tuning and calibration procedures.
- It is able to store about five millions of events and to process them in a day or two.

Therefore, the Mini-AOD format contains high-level objects, saved with detailed information only if they pass some basic quality requirements, otherwise only the detector clusters are stored. This approach to the data storage allows the size of the Mini-AOD to be approximately 35-60 kilobytes per event, while the AOD size was about 480 kilobytes per events. The simulated particle format, called GenParticles, it would be difficult to be whole saved, since it takes a lot of space. The GenParticles are hence stored in the Mini-AOD in two different collections. One is the *prunedGenParticles*, a subset (about 50-100 per event) of the main collection that includes initial partons, heavy flavour particles, electroweak bosons, and leptons. The second is the *packedGenParticles*, that contains only stable final-state particles, together with their four momentum, charge and the PDG identifier code. Moreover, a link to their first ancestor in the *prunedGenParticles* is saved, in order to reconstruct the decay chain of the event. Beyond the Mini-AOD, a new data format has been recently developed with the aim of further reducing the size of an event by another order of magnitude (to get approximately 1 kilobyte per event), called the Nano-AOD. This format consists of a bare ROOT ntuple and it provides the basic per-event information that is needed in most generic analyses, avoiding for example the storage of detector details for objects or saving variables with limited precision.

5.4 Validation of the Rivet analysis with Nano-AOD

The Monte Carlo samples of this analysis utilizes the Mini-AOD format, and the simulation is performed at GEN level. The W$\gamma\gamma$ and Z$\gamma\gamma$ samples have been also produced in the Nano-AOD format, a more manageable format to make comparisons between MC and data that will be performed in the data analysis. The RIVET routine has been then tested comparing the Mini-AOD distributions obtained from the Rivet analysis with those obtained (without making use of Rivet) from the Nano-AOD format, at GEN level. The compared distributions are:

Observable	Figure
Z mass	5.21
p_T leading photon in Z$\gamma\gamma$	5.22
W transverse mass	5.23
p_T leading photon in W$\gamma\gamma$	5.24

The difference between the analysis of the two AOD formats, expressed as 1 - the ratio of the histograms integrals $\frac{\text{MiniAOD}}{\text{NanoAOD}}$, amounts to $\sim 2\%$ for the Z$\gamma\gamma$ sample, and $\sim 4\%$ (electronic decay) or $\sim 3\%$ (muonic decay) for the W$\gamma\gamma$ sample. This discrepancy can be ascribed to a slightly different storage of the genParticles in the two formats, and to the reduced precision of the NanoAOD variables that is less than 32bit (the precision standard adopted for MiniAOD). The distributions obtained using the Rivet routine are then considered reliable for the analysis and they will be used for the evaluation of the theoretical uncertainties performed in the next chapter.

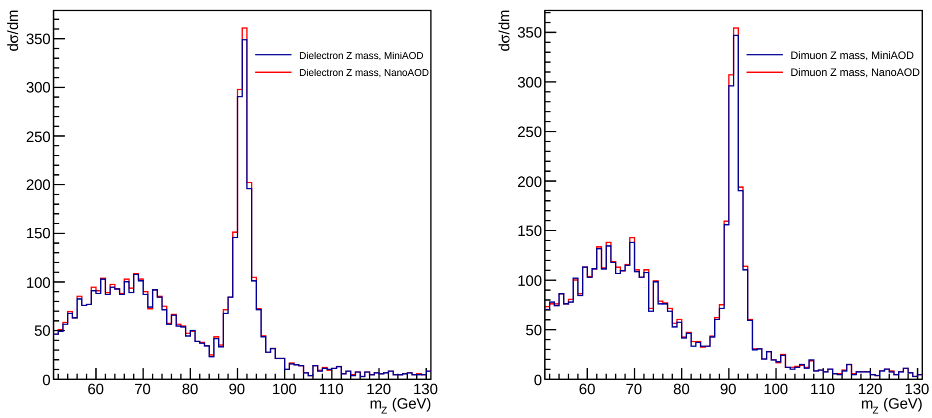

Figure 5.21: Reconstructed Z mass in the electronic (left) and muonic (right) channels. The blue histogram refers to the MiniAOD, the red one to the Nano-AOD.

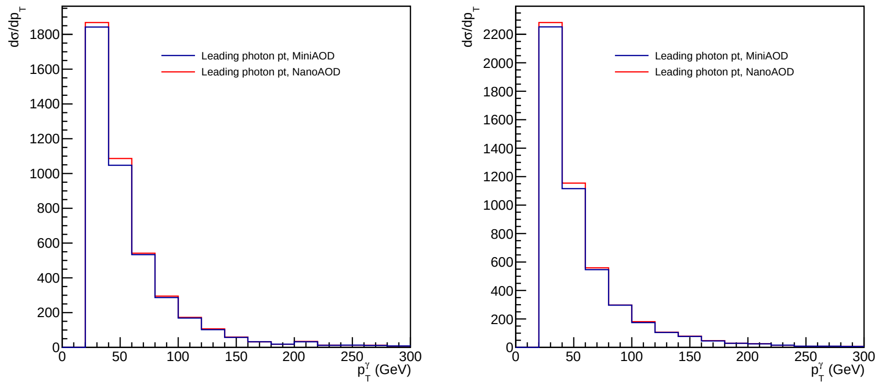

Figure 5.22: Transverse momentum p_T of the leading photon in the Z$\gamma\gamma$ event, in the electronic (left) and muonic (right) channels. The blue histogram refers to the MiniAOD, the red one to the Nano-AOD.

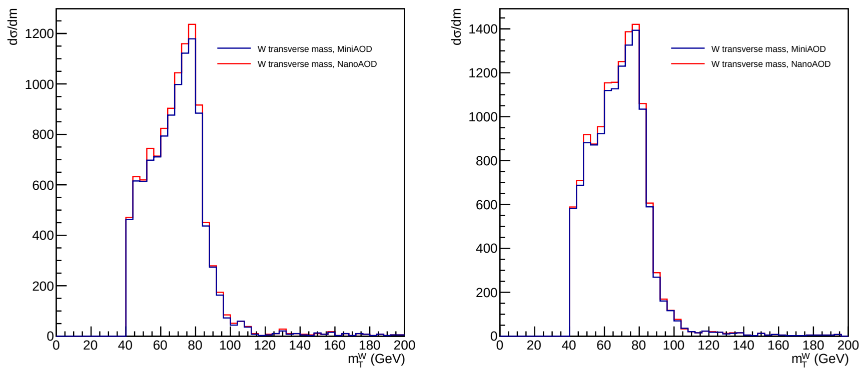

Figure 5.23: Transverse W mass in the electronic (left) and muonic (right) channels. The blue histogram refers to the MiniAOD, the red one to the Nano-AOD.

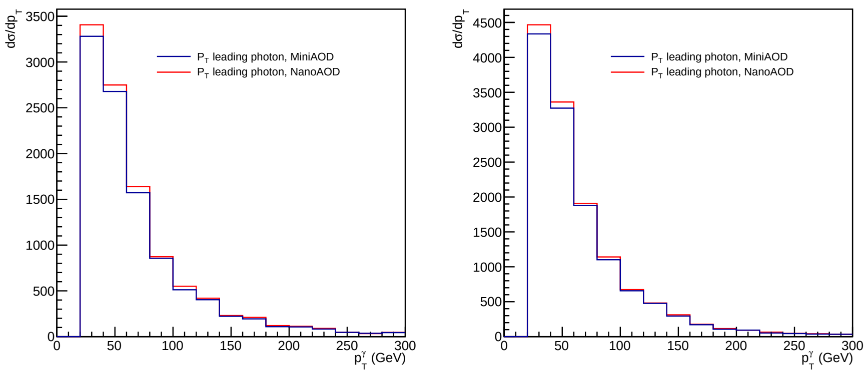

Figure 5.24: Transverse momentum p_T of the leading photon in the W$\gamma\gamma$ event, in the electronic (left) and muonic (right) channels. The blue histogram refers to the MiniAOD, the red one to the Nano-AOD.

Chapter 6

Study of the theoretical QCD uncertainties on the V$\gamma\gamma$ cross sections

In the previous chapter, the differential cross sections have been obtained from Monte Carlo samples, and the systematics affecting such measurements have been here studied. They can be due to uncertainties in the experimental apparatus (calibration errors, detector acceptance) or in the theoretical model adopted. Since the samples used in this work have been obtained at GEN level, possible apparatus effects are not present, and only the systematics due to theoretical uncertainties are therefore evaluated. They arise in the determination of the Parton Distribution Functions and the strong coupling constant, and in the arbitrary choice of the renormalization and factorization parameters, that are introduced to eliminate the divergences arisen in QCD calculations and to separate perturbative from non-perturbative terms, in order to treat them separately.

6.1 Parton Distribution Functions uncertainties

The Parton Distribution Functions (PDFs) $f_i(x, Q^2)$ gives the probability of finding in the proton a parton i carrying a fraction x of the total proton momentum, with Q being the energy scale of the hard process (see section 3.3). The PDFs have to be determined from experimental measurements, that can be for example Deep Inelastic Scattering (DIS) experiments, as those performed at HERA (Hadron Elektron Ring Anlage), where electrons (or positron) were collided with protons at $\sqrt{s} = 225 - 318$ GeV [106]. The DIS measurements can be carried out in two channels, both shown in Figure 6.1: the neutral current (NC) interaction ep $\rightarrow$ eX mediated by photons or Z boson, and the charged current (CC) interaction ep $\rightarrow \nu X$ mediated by W bosons. The DIS cross section for NC processes (and similarly for CC

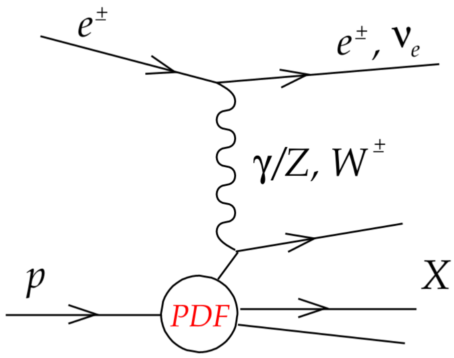

Figure 6.1: Diagrams of neutral and charged current deep inelastic scattering processes.

processes) can be expressed in terms of the structure functions $F_i(x, Q^2)^{NC}$ [107]

$$\frac{d^2\sigma^{NC}}{dxdQ^2}(x, y, Q^2) = \frac{2\pi\alpha^2}{xQ^4}\left[Y_+ F_2^{NC}(x, Q^2) \mp Y_- x F_3^{NC}(x, Q^2) - y^2 F_L^{NC}(x, Q^2)\right]$$

where

$$F_L(x, Q^2) \equiv F_2(x, Q^2) - 2xF_1(x, Q^2)$$
$$Y_\pm \equiv 1 \pm (1 - y^2).$$

These relations are written as function of the electron momentum $y \equiv \frac{p \cdot q}{p \cdot k} = \frac{Q^2}{xs}$, where p and q are the momenta of the incoming proton and lepton, respectively, $q = Q^2$ is the photon momentum and s is the center of mass energy of the lepton-proton collision, neglecting the proton mass. The structure functions can be factorized as follows

$$F_i(x, Q^2) = x \sum_a \int_x^1 \frac{dz}{z} C_{i,a}\left(\frac{x}{z}, \alpha_S(Q^2)\right) f_a(z, Q^2)$$

where $f_a(z, Q^2)$ is the distribution of the parton a in the proton and $C_{i,a}$ is the structure function computed with an incoming parton. At leading order, $C_{i,a}$ can be zero (for gluons) or a constant times a Dirac delta.

6.1.1 Determination of the PDFs

The general procedures for the determination of the PDFs consists in parameterizing the x-dependence of the distributions at some value of $Q^2 = Q_0^2$ such that the unknown terms of the perturbative expansion can be assumed to be negligible, and then evolving these distributions up in Q^2 using a DGLAP equation that takes the form

$$\frac{\partial f_a}{\partial Q^2} \sim \frac{\alpha_S(Q^2)}{2\pi} \sum_b (P_{ab} \otimes f_b)$$

where P_{ab} are the splitting functions that describe the probability of a given parton to separate into two, and n_f represents the number of quark flavours. At the leading order, the splitting functions are

$$
\begin{aligned}
P_{qq} &= \frac{4}{3}\left[\frac{1+x^2}{1-x}\right] \\
P_{qg} &= \frac{1}{2}\left[x^2+(1-x)^2\right] \\
P_{gq} &= \frac{4}{3}\left[\frac{1+(1-x)^2}{x}\right] \\
P_{gg} &= 6\left[\frac{1-x}{x}+x(1-x)+\frac{x}{1-x}\right] \\
&+\left[\frac{11}{2}-\frac{n_f}{3}\right]\delta(1-x).
\end{aligned}
$$

The obtained distributions are then fitted to different sets of experimental DIS and hard scattering data, with a number of unknown parameters between 10 and 30. At present, there are six groups involved in the PDFs determination: MMHT [109], CTEQ [110], NNPDF [111], HERAPDF [112], ABMP [113] and JR [114]. They all provide PDFs up to next-to-next-leading-order (NNLO). The MMHT (Martin-Motylinski-Harland Lang-Thorne) PDFs are extracted from HERA DIS data for the low-x behaviour and from fixed target DIS for the high-x behaviour. In this region, also TEVATRON data are used to constrain the distributions. The CTEQ (Coordinated Theoretical/Experimental Project on QCD Phenomenology) PDFs are determined employing the same data, but using a different analysis model. The NNPDF (Neural Net PDF) group works on MC replicas of the experimental data, extracting the PDF via neural network algorithms. The HERAPDF group performs the fit only on HERA DIS data, while the ABMP (Alekhin-Blümlein-Moch-Placakyte) employs only NC DIS data and some results from fixed-target experiments. JR (Jimenez Delgado-Reya) PDFs are instead determined using a dynamical model for the evolution of the input distributions, which are obtained at a very low starting scale with respect to the other groups. In all these analysis, the masses of the u, d and s quarks are assumed to be negligible, while the treatment of heavy b and c quark masses is slightly different among the groups. The results are all summarized in the PDF4LHC report [115].

6.1.2 Evaluation of the PDFs uncertainties

The evaluation of the PDFs uncertainties can be performed using the *Hessian* method or the *Monte Carlo* method [116].

Hessian method

The Hessian method is based on the standard least squared technique. The χ^2 function can be written as [107]

$$\chi^2 = \sum_{i=1}^{N_{dat}} \sum_{j=1}^{N_{dat}} (D_i - T_i)\left(V^{-1}\right)_{ij}\left(D_j - T_j\right)$$

where D_i represents the experimental data, T_i the theoretical predictions, and V^{-1} is the experimental covariance matrix. Assuming that $\{a_1^0, ..., a_n^0\}$ is the set of parameters that minimize χ^2, which is also assumed to be quadratic around the global minimum, one can define

$$\Delta\chi^2 \equiv \chi^2 - \chi^2_{min} = \sum_{i,j=1}^{n} H_{ij}\left(a_i - a_i^0\right)\left(a_j - a_j^0\right),$$

where H is the Hessian matrix, whose coefficients are given by

$$H_{ij} = \frac{1}{2}\frac{\partial^2\chi^2}{\partial a_i \partial a_j}\bigg|_{min}.$$

The Hessian matrix can be inverted and then diagonalized to obtain the covariance matrix set of eigenvalues λ_k and the orthonormal eigenvectors $\mathbf{v}_k$, with $k \in \{1, ..., n\}$. The distance of a parameters set from the one that minimizes the χ^2 can be then written in the basis of the rescaled eigenvectors $\mathbf{e_k} = \sqrt{\lambda_k}\mathbf{v_k}$, such as $a_i - a_i^0 = \sum_{k=1}^{n} e_{ik} z_k$. The index i identifies the i-component of $\mathbf{e}_k$. Exploiting the eigenvectors orthonormality,

$$\chi^2 = \chi^2_{min} + \sum_{k=1}^{n} z_k^2$$

that is the equation of an hypersphere of radius $t = (\Delta\chi^2)^{1/2} = \left(\sum_{k=1}^{n} z_k^2\right)^{1/2}$. To evaluate the PDF uncertainties on a given observable X, two new PDFs $S_k^{\pm}$ sets are produced, with parameters $a_i(S_k^{\pm}) = a_i^0 \pm te_{ik}$, where t is chosen properly to obtain uncertainties with the desired confidence level (CL). Hence

$$(\Delta X)_+ = \sqrt{\sum_{k=1}^{n} \{\max\left[X(S_k^+) - X(S_0), X(S_k^-) - X(S_0), 0\right]\}^2}$$

$$(\Delta X)_- = \sqrt{\sum_{k=1}^{n} \{\max\left[X(S_0) - X(S_k^+), X(S_0) - X(S_k^-), 0\right]\}^2}$$

where $X(S_k^{\pm})$ corresponds to the variable X evaluated with a given PDFs set. A symmetric error can also be evaluated

$$\Delta X = \frac{1}{2}\sqrt{\sum_{k=1}^{n} [X(S_k^+) - X(S_k^-)]^2}.$$

Monte Carlo method

The Monte Carlo method works with MC replicas of the data sets, that can be generated as follows

$$D_{m,i} \rightarrow \left(D_{m,i} + R_{m,i}\sigma_{m,i}\right).$$

$D_{m,i}$ is the i-th point of the data set labelled with m, $\sigma_{m,i}$ is the associated error and $R_{m,i}$ is a random number obtained from a Gaussian distribution of mean zero and variance one. For each replica a PDFs set is extracted, and an observable X is then evaluated as the average over all the N_{rep} replicas

$$\langle X \rangle = \frac{1}{N_{rep}} \sum_{k=1}^{N_{rep}} X(S_k)$$

with standard deviation

$$\Delta X = \sqrt{\frac{N_{rep}}{N_{rep}-1}\left(\langle X^2 \rangle - \langle X \rangle^2\right)}.$$

The two methods are approximately equivalent, and the results obtained are reciprocally consistent. The Monte Carlo approach is better suited for fitting limited data sets and exploring parameterization bias.

6.1.3 Uncertainties on the NNPDF3.1 PDFs set

The W$\gamma\gamma$ and Z$\gamma\gamma$ Monte Carlo samples have been generated with the NNPDF3.1 PDFs set at the NNLO precision. The PDFs evaluation is performed with data from HERA DIS and fixed-target experiments, and from Tevatron and LHC collider measurements. The input distributions are parameterized at a scale $Q_0 = 1.65$ GeV and with a value of $\alpha_S(m_Z^2) = 0.118$, in terms of a neural network NN times a pre-processing factor

$$f_i(x, Q_0) \propto x^{\alpha_i}(1-x)^{\beta_i} NN_i(x)$$

where $x^{\alpha_i}(1-x)^{\beta_i}$ is the pre-processing factor, simply added to speed the fit procedure. The NNLO NNPDF3.1 PDFs set is displayed in Figure 6.2. The PDFs have been first produced as $N_{rep} = 1000$ replica sets and this number is subsequently reduced, through dedicated algorithms, to obtain both the Monte Carlo PDFs representation with $N_{rep} = 100$ replicas and the Hessian PDFs representation with $N_{eig} = 100$ symmetric eigenvectors. In particular, the set included in the present analysis is the `NNPDF31_nnlo_hessian_pdfas`, and it consists of 103 *members*:

- The central value (PDF member 0) which is the nominal value at which the distributions are evaluated.

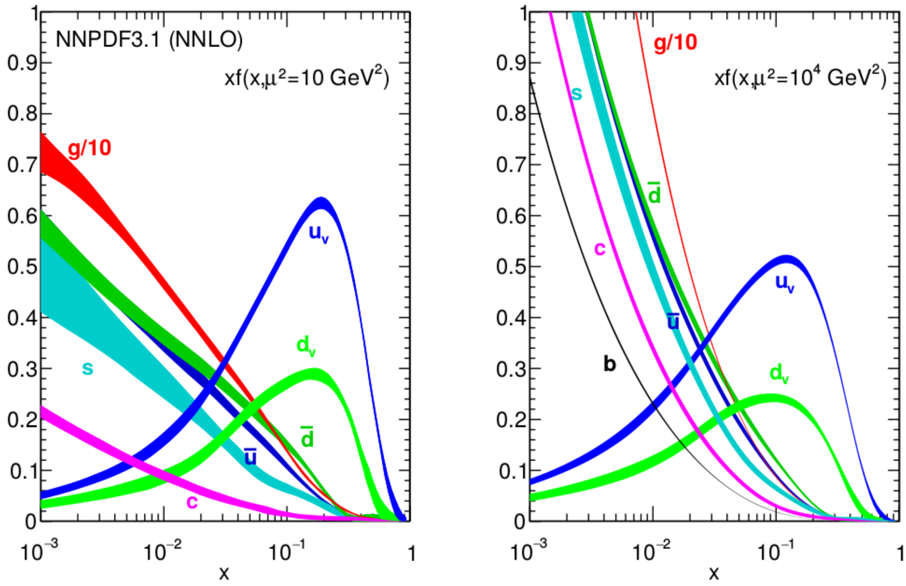

Figure 6.2: NNPDF3.1 PDFs set at $\mu^2 = 10$ GeV^2 and $\mu^2 = 10^4$ GeV^2.

- 100 *error members* (PDF members 1-100), each one corresponding to a $\pm 1\sigma$ variation along the eigenvectors direction.
- Two more central values (PDF member 101 and 102), corresponding to $\alpha_S(m_Z) = 0.116$ and $\alpha_S(m_Z) = 0.120$ respectively. The treatment of the uncertainty due to α_S will be discussed in the next section.

The PDFs uncertainties on a physical observable X are determined following the *PDF4LHC recommendations for LHC Run 2* [115], according to which

$$\delta^{PDF} X = \sqrt{\sum_{k=1}^{N_{mem}} \left(X^{(k)} - X^{(0)}\right)^2},$$

where N_{mem} is equal to 100, the number of error members, and $X^{(k)}$ is the physical observables obtained with the k-th PDF set.

6.2 Evaluation of the uncertainty on the choice of the strong coupling constant

6.2.1 The strong coupling constant α_S

The strong coupling constant, defined $\alpha_S = \frac{g_S}{4\pi}$, where g_S represents the coupling constant appeared in the QCD Lagrangian (see section 1.4), can not be directly measured in an experiment, but its value can be extracted from measurable observables in the context of perturbation theory. For example, studying the total cross section for $e^-e^+ \to$ hadrons processes, at a center of mass energy Q, the following quantity can be evaluated

$$\frac{\sigma(\mathrm{e^-e^+} \to \text{hadrons}), Q}{\sigma(\mathrm{e^-e^+} \to \mu^-\mu^+), Q} \equiv R(Q) = R_{EW}(Q)(1 - \delta_{QCD}(Q))$$

where R_{EW} is the purely electroweak prediction for the ratio, while δ_{QCD} is the correction due to QCD effects and it is expressed in terms of an α_S series expansion. The value of the strong coupling constant has been extracted from several physical analysis and using different perturbative techniques. The main results came from the analysis of the hadronic decays of τ and heavy quarkonia ($\mathrm{b\bar{b}}$ and $\mathrm{c\bar{c}}$), DIS, studies of the event shapes in the hadronic $\mathrm{e^-e^+}$ annihilation, and studies of the jets cross section and angular correlation at the hadron colliders (Tevatron and LHC). The α_S measurements have been obtained at the Z boson mass scale and then they have been combined in order to evaluate the world average value for the strong coupling. Some results, as those coming from DIS and τ decays, need to be pre-averaged before the calculation of the final value. This is done because in these cases different determinations of the strong coupling from similar datasets produce values of α_S that are only marginally compatible with each other, probably as a consequence of the difficulties encountered in including the correct systematic uncertainties. The world average value is then determined using the χ^2 *averaging* method, as illustrated in [117], that assumes pre-averaged results largely independent of each other. The obtained value is

$$\alpha_S(m_Z^2) = 0.1181 \pm 0.0011.$$

In Figure 6.3 the measurements of $\alpha_S(m_Z^2)$ used for the determination of the world average value are reported. The uncertainty due to the determination of α_S is obtained following the prescriptions of the *PDF4LHC recommendations for LHC Run 2*. The 101-th and 102-th members of the `NNPDF31_nnlo_hessian_pdfas` set correspond to PDFs central values with $\alpha_S(m_Z^2)$=0.116 and $\alpha_S(m_Z^2)$=0.120, respectively. The uncertainty on a given observable X is evaluated as follows

$$\delta^{\alpha_S} X = \frac{X(\alpha_S = 0.116) - X(\alpha_S = 0.120)}{2}.$$

Therefore, the combined PDF+α_S uncertainties are combined adding them in quadrature

$$\delta^{PDF+\alpha_S} X = \sqrt{\left(\delta^{PDF} X\right)^2 + (\delta^{\alpha_S} X)^2}.$$

In the process of evaluation of the theoretical uncertainties on the distribution obtained in the previous chapter, the LHAPDF [118] C++ library is used in the Rivet routine to provides access to the 103 members of the PDFs set.

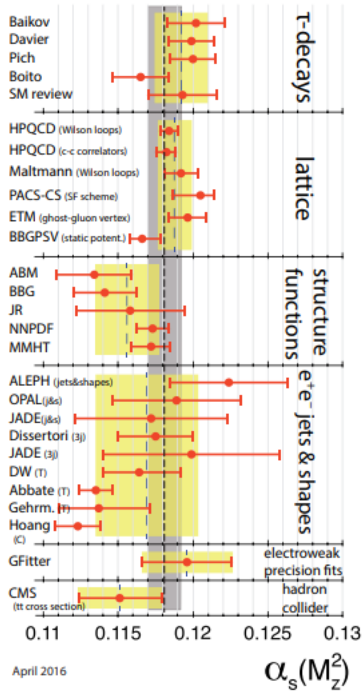

Figure 6.3: Summary of the measured values of $\alpha_S(m_Z^2)$. The yellow bands and dashed lines indicate the pre-average values, while the dotted line and grey band represent the final world average value of $\alpha_S(m_Z^2)$.

6.3 Evaluation of the uncertainty on the choice of the renormalization and factorization scale

In section 1.4.2, the running of α_S has been discussed as a consequence of the QCD renormalization procedures. In QCD calculations in fact, ultraviolet (UV) divergences can arise in the evaluation of perturbation theory integrals due to the loop corrections in the Feynman diagrams. Examples of Feynman diagrams with one-loop corrections to the electron propagator are shown in Figure 6.4. To deal

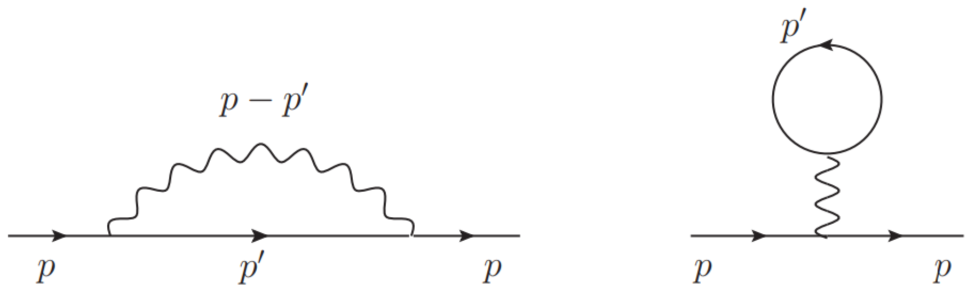

Figure 6.4: One loop diagrams arising in the expansion of the electron propagator.

with such divergences, a regularization procedure is needed, called *renormaliza-*

tion. The renormalization requires the addition of an energy cut-off that allows to separate the integrals in a finite and a divergent part, the latter removed adding to the QCD Lagrangian some appropriate counterterms. This cut-off is termed the renormalization factor μ_R, which it is not a physical observable but rather a theoretical input that has to be chosen in advance. Another energy cut-off that has to be introduced is the factorization scale μ_F, as described in 3.3.1. It represents the resolution with which the hadrons are probed in a collision, and it means that, in the collinear factorization, emissions with transverse momenta above μ_F are included in the hard scattering cross section term, while emissions with transverse momenta below μ_F are included in the PDFs term. As the renormalization factor, the factorization scale is arbitrary. The usual choice for both parameters is to take $\mu_R = \mu_F = Q$, where Q is the energy scale of the process. The uncertainty on a given variable X (the bin content here) due to this choice is determined by varying μ_R and μ_F between $Q/2$ and $2Q$, separately, for a total of nine (μ_R, μ_F) couples. More often these parameters are expressed dividing them by Q, which means that their variations are between 0.5 and 2. Hence,

$$\delta^{\mu_R+\mu_F} X = \max(X^0 - X^i),$$

where X^0 represents the variable evaluated at $\mu_R = \mu_F = 1$, while X^i is evaluated with the remaining eight couples.

6.4 Results

In the 8 TeV CMS analysis, the total statistical contribute to the uncertainty of the inclusive cross section was estimated to be about 30-50% for W$\gamma\gamma$ and 14-17% for Z$\gamma\gamma$ measurements, while the total systematic contribute was about 38% for W$\gamma\gamma$ and basically equal to the statistical contribute for Z$\gamma\gamma$. The summary of the obtained uncertainties is reported in Table 6.1. The statistical contribute to the total uncertainty was always larger or at least equal to the systematic one, due to the limited 8 TeV statistics. The 13 TeV analysis, with the full 140 fb^{-1} statistics with

	W$\gamma\gamma$		Z$\gamma\gamma$	
	e channel	μ channel	ee channel	$\mu\mu$ channel
Total statistical	47.8	29.6	16.6	13.7
Total systematic	38.3	37.9	16.5	13.7
Integrated luminosity	2.6	2.6	2.6	2.6

Table 6.1: Systematic and statistical uncertainties on the W$\gamma\gamma$ and Z$\gamma\gamma$ cross section measurements, expressed as percentages of the measured cross section.

respect to the previous 20 fb^{-1}, is expected to reduce the statistical uncertainty

Observable	Figure
p_T leading lepton	6.5
p_T leading photon	6.6
p_T subleading photon	6.7
Diphoton p_T	6.8
W transverse mass	6.9
Diphoton mass	6.10

Observable	Figure
p_T leading lepton	6.11
p_T subleading lepton	6.12
p_T leading photon	6.13
p_T subleading photon	6.14
Diphoton p_T	6.15
Diphoton mass	6.16
Z mass	6.17
Z$\gamma\gamma$ mass	6.18

by a factor two or three. Studies on the systematics affecting the measurement are then required to verify if a similar improvement can be achieved also for the other contributions to the total uncertainty. The theoretical errors due to PDFs, α_S, μ_R and μ_F, have been evaluated for all the differential cross section distributions obtained in the previous chapter, that are listed in Table 6.4. The PDFs+α_S error bars are shown in yellow, while the $\mu_R + \mu_F$ error bars are shown in blue. The relative errors on the inclusive cross section measured for each distributions are reported in Tables 6.2 and 6.3.

	e channel			μ channel		
	PDF+α_S	$\mu_R + \mu_F$	total	PDF+α_S	$\mu_R + \mu_F$	total
Lepton p_T	0.27	0.57	0.63	0.17	0.43	0.46
Leading photon p_T	0.26	0.56	0.62	0.25	0.25	0.35
Subleading photon p_T	0.41	0.52	0.66	0.40	0.38	0.55
Diphoton p_T	0.23	0.48	0.53	0.22	0.45	0.50
W transverse mass	0.15	0.53	0.55	0.12	0.39	0.41
Diphoton mass	0.03	0.52	0.52	0.03	0.53	0.53

Table 6.2: Systematic uncertainties on the W$\gamma\gamma$ differential cross section measurements, expressed as percentages of the measured cross section.

As one can see the errors associated to the PDFs and α_S are always smaller or at least equal than those associated to scale and renormalization factors in the W$\gamma\gamma$ distributions. For Z$\gamma\gamma$ instead, the two different contributes to the relative errors vary among distributions. In the p_T distribution of the subleading lepton, for example, the relative error associated with PDFs and α_S is twice the relative error associated to μ_R and μ_F Furthermore, the trend that can be observed in all the distributions is that the relative theoretical uncertainties increase at high energies, since at high p_T values the perturbative QCD series diverge and the subsequent description of the PDFs and of the other QCD parameters results to be less efficient. The relative errors associated with $\mu_R + \mu_F$ for the single bins go from ~1% at low

	ee channel			$\mu\mu$ channel		
	PDF+α_S	$\mu_R + \mu_F$	total	PDF+α_S	$\mu_R + \mu_F$	total
Leading lepton p_T	0.81	0.68	1.06	0.81	0.46	0.93
Subleading lepton p_T	0.99	0.66	1.19	1.05	0.48	1.15
Leading photon p_T	0.78	0.76	1.09	0.86	0.51	1.00
Subleading photon p_T	1.26	0.81	1.50	1.31	0.66	1.47
Diphoton p_T	0.65	0.54	0.85	0.70	0.50	0.86
Z mass	0.20	0.36	0.41	0.19	0.35	0.40
Diphoton mass	0.59	0.68	0.90	0.61	0.45	0.76
Z$\gamma\gamma$ mass	0.44	0.47	0.64	0.48	0.41	0.63

Table 6.3: Systematic uncertainties on the Z$\gamma\gamma$ differential cross section measurements, expressed as percentages of the measured cross section.

p_T or mass values, to ~20% at high p_T or mass values. The relative errors associated with PDF+α_S instead go from ~1% to ~10%. These results will be used in the evaluation of the expected limits on the anomalous quartic gauge couplings, comparing the Standard Model cross section differential distributions here produced with the reweighted distributions incorporating anomalous coupling effects, that are obtained following the reweighting procedure described in section 3.5.

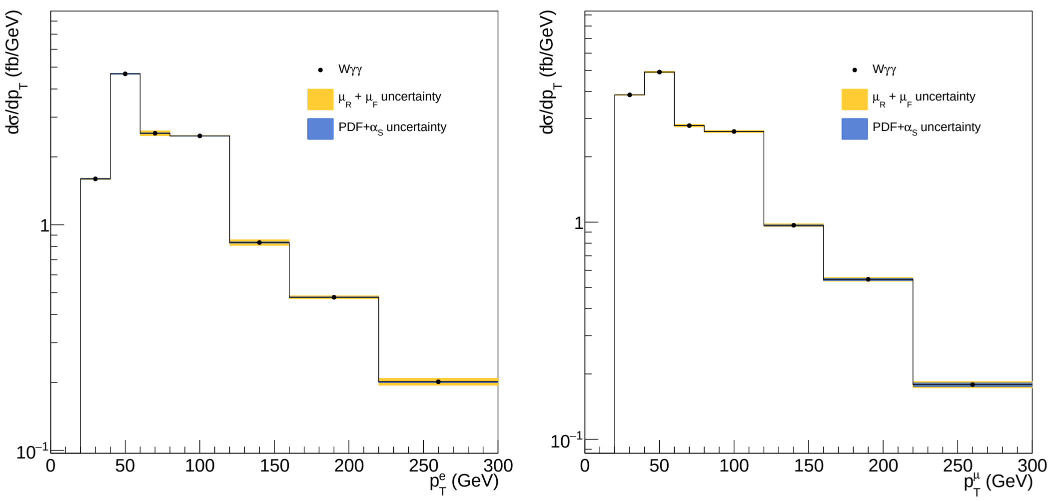

Figure 6.5: Transverse momentum of the W decay electron (left) and muon (right) in semi-log scale.

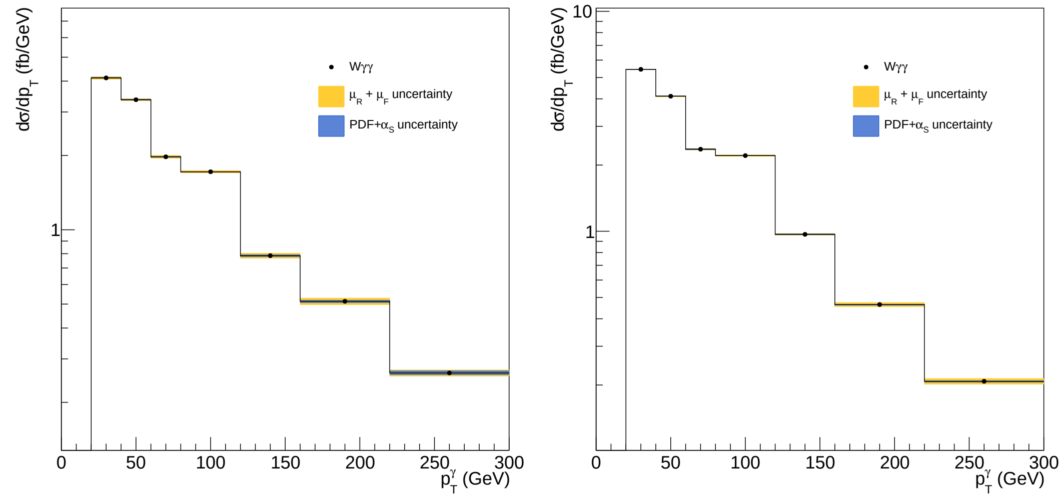

Figure 6.6: Transverse momentum of the leading photon of the W$\gamma\gamma$ vertex for the electronic (left) and muonic (right) W decay, in semi-log scale.

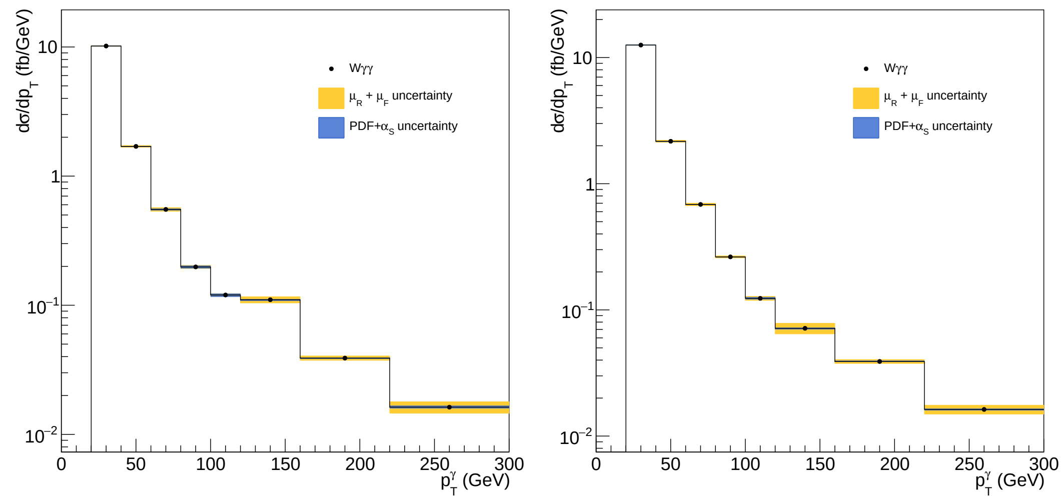

Figure 6.7: Transverse momentum of the subleading photon of the W$\gamma\gamma$ vertex for the electronic (left) and muonic (right) W decay, in semi-log scale.

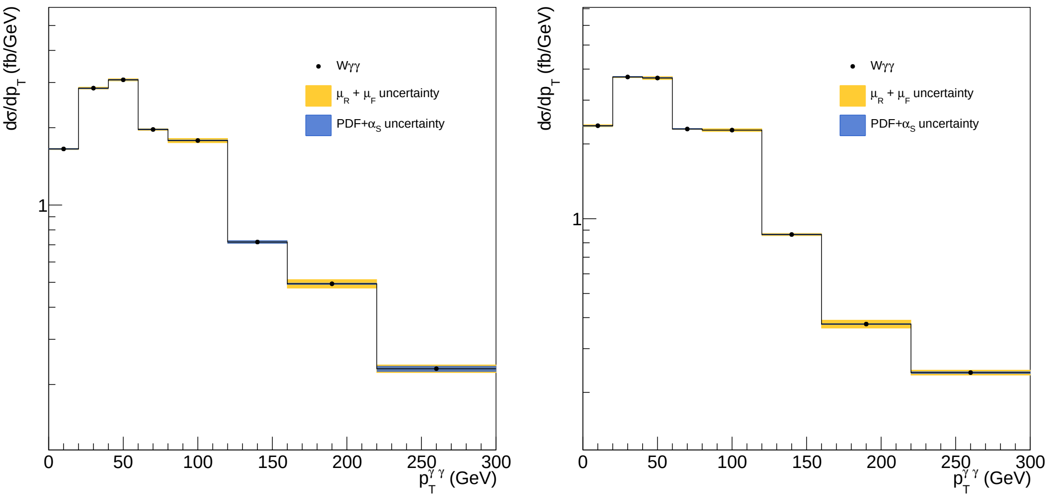

Figure 6.8: Diphoton transverse momentum for the electronic (left) and muonic (right) W decay, in semi-log scale.

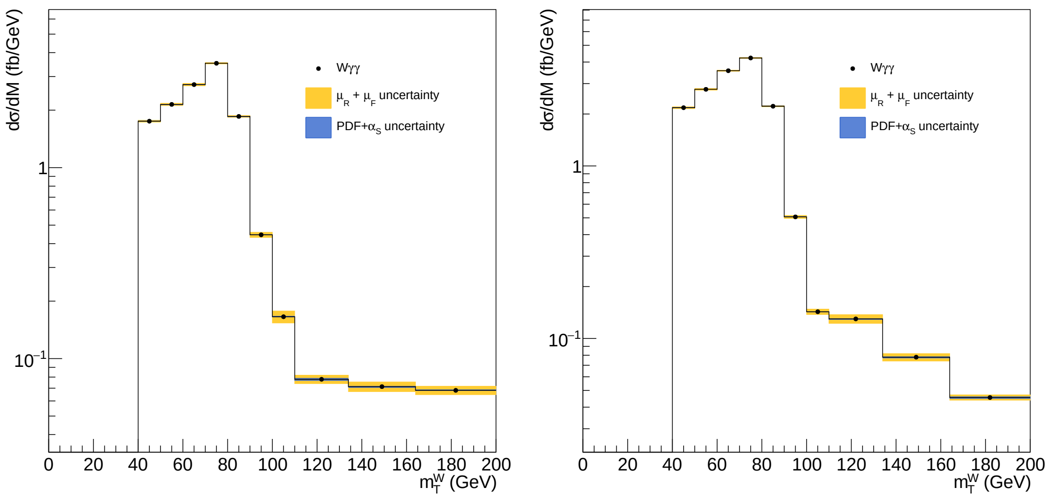

Figure 6.9: W transverse mass for the electronic (left) and muonic (right) W decay, in semi-log scale.

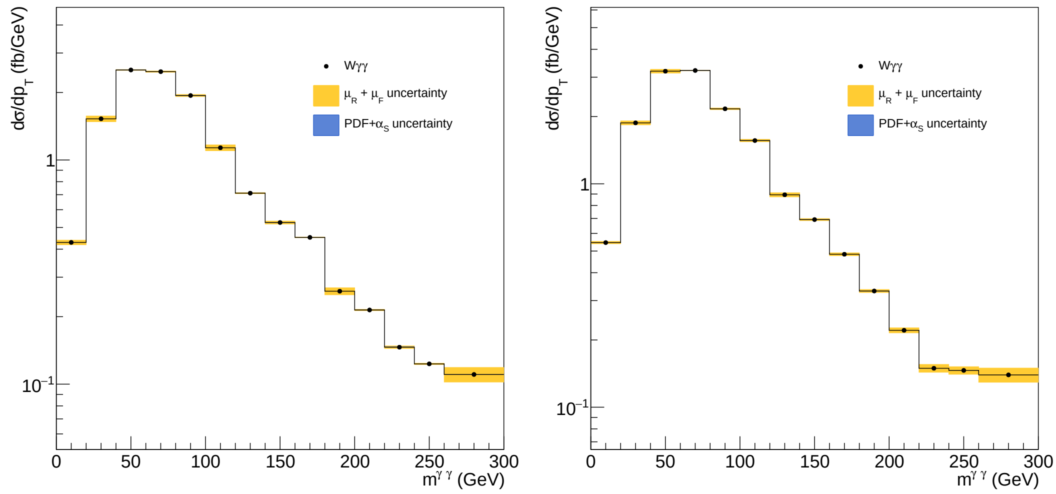

Figure 6.10: Diphoton mass for the electronic (left) and muonic (right) W decay, in semi-log scale.

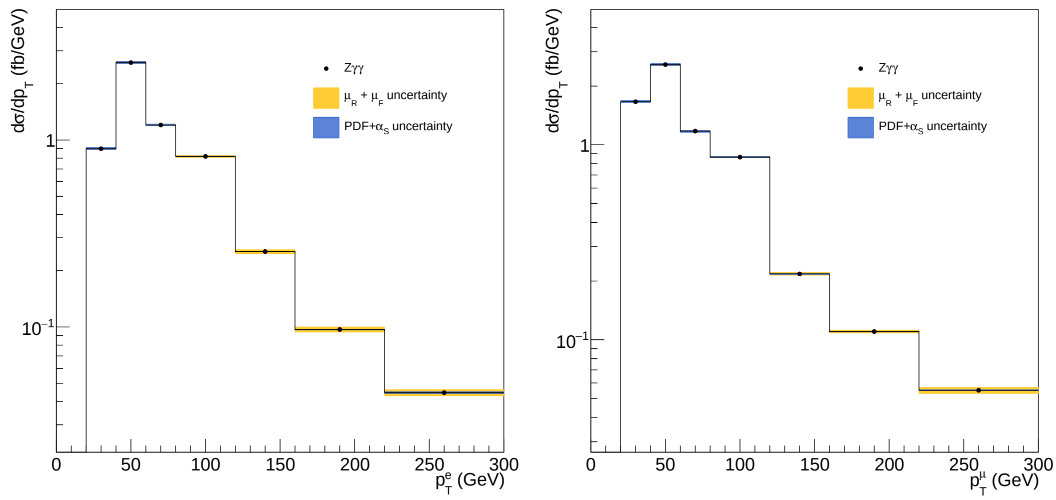

Figure 6.11: Transverse momentum of the leading Z decay electron (left) and muon (right) in semi-log scale.

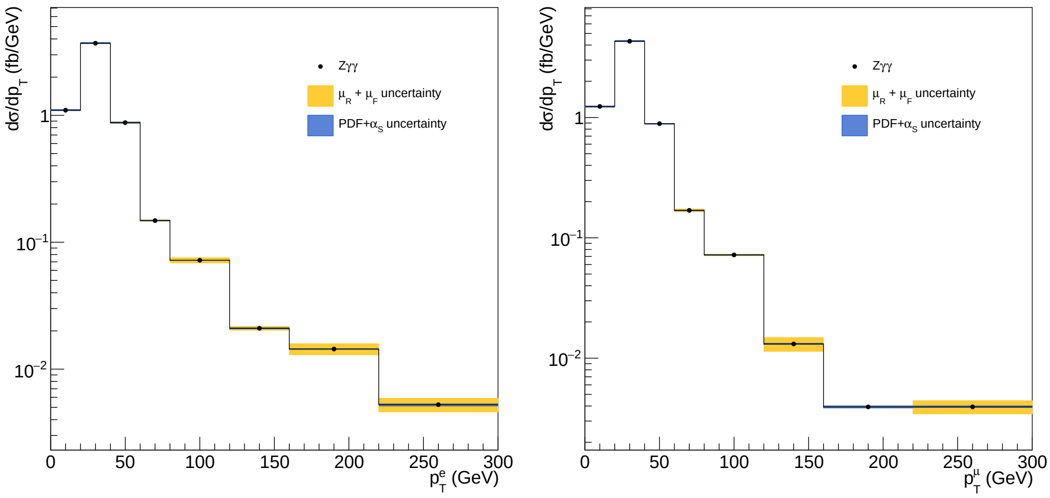

Figure 6.12: Transverse momentum of the subleading Z decay electron (left) and muon (right) in semi-log scale.

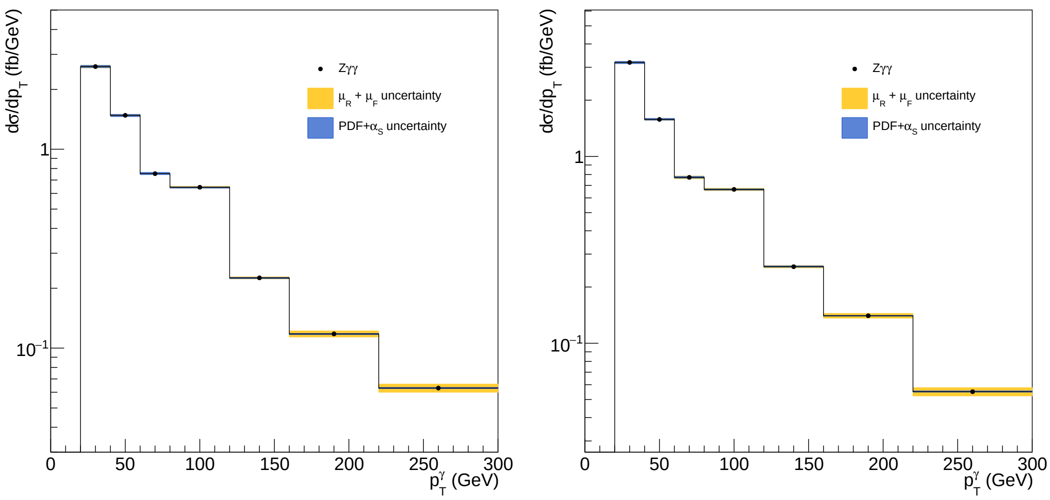

Figure 6.13: Transverse momentum of the leading photon of the $Z\gamma\gamma$ vertex for the electronic (left) and muonic (right) Z decay, in semi-log scale.

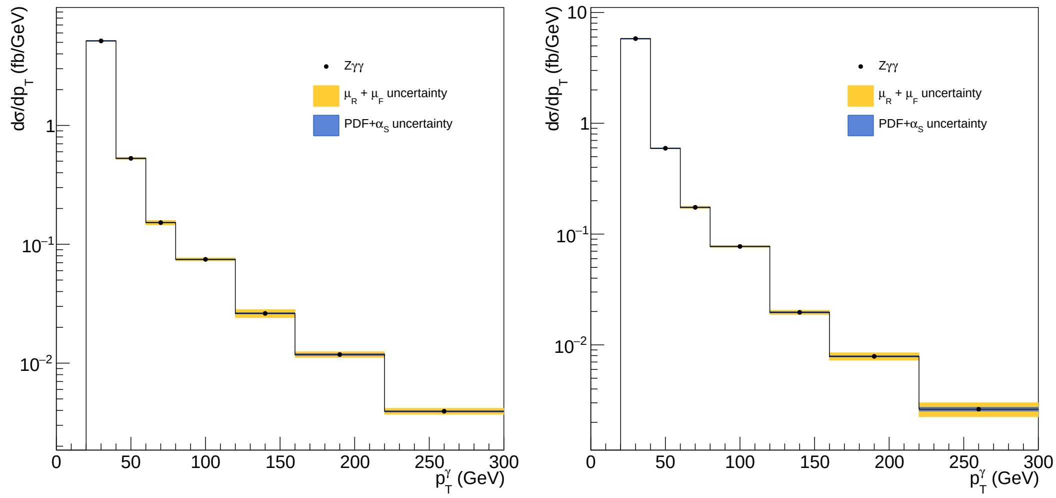

Figure 6.14: Transverse momentum of the subleading photon of the $Z\gamma\gamma$ vertex for the electronic (left) and muonic (right) Z decay, in semi-log scale.

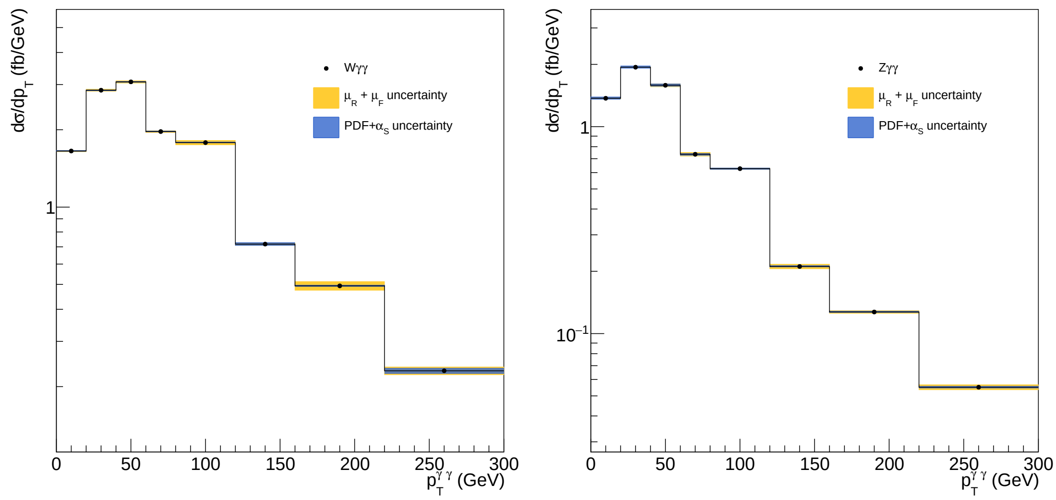

Figure 6.15: Diphoton transverse momentum for the electronic (left) and muonic (right) Z decay, in semi-log scale.

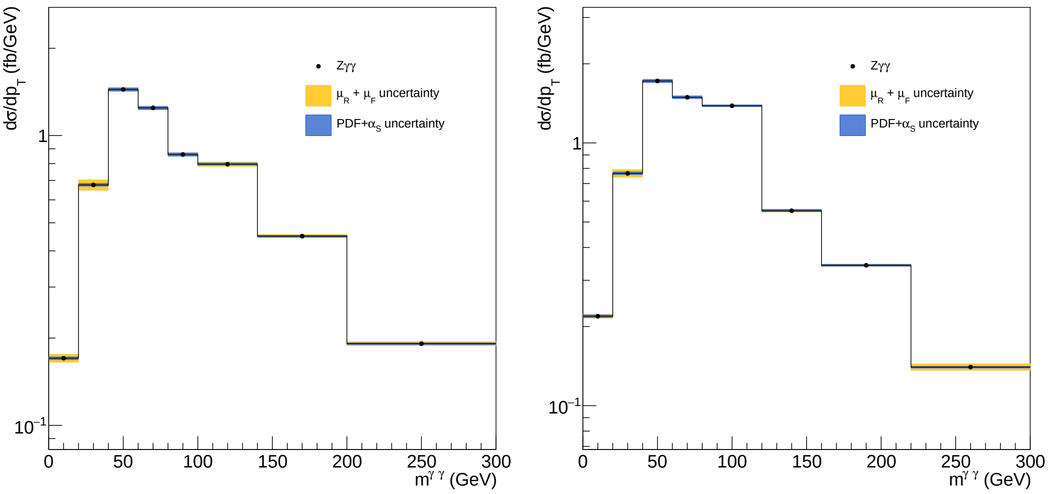

Figure 6.16: Diphoton mass for the electronic (left) and muonic (right) Z decay, in semi-log scale.

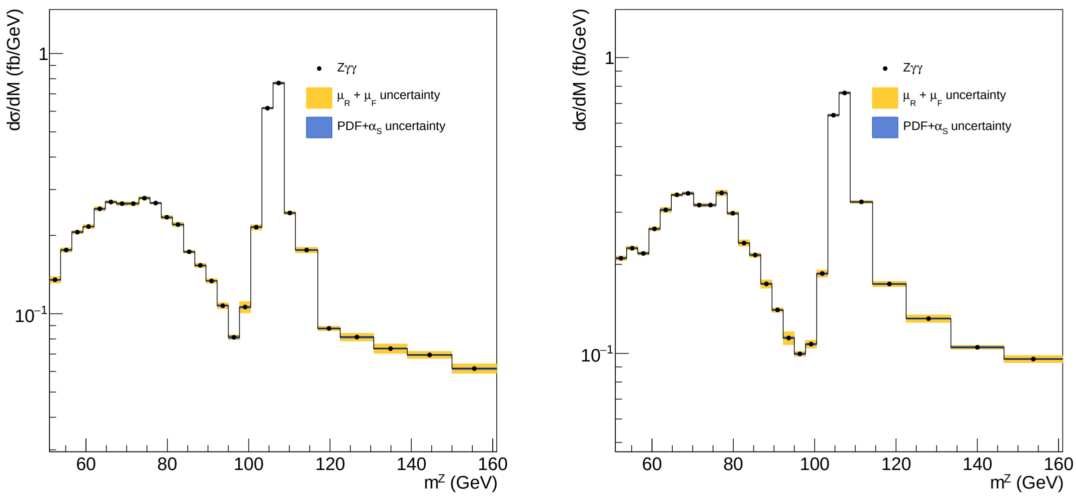

Figure 6.17: Reconstructed Z mass in the electronic (left) and muonic (right) channel, in semi-log scale.

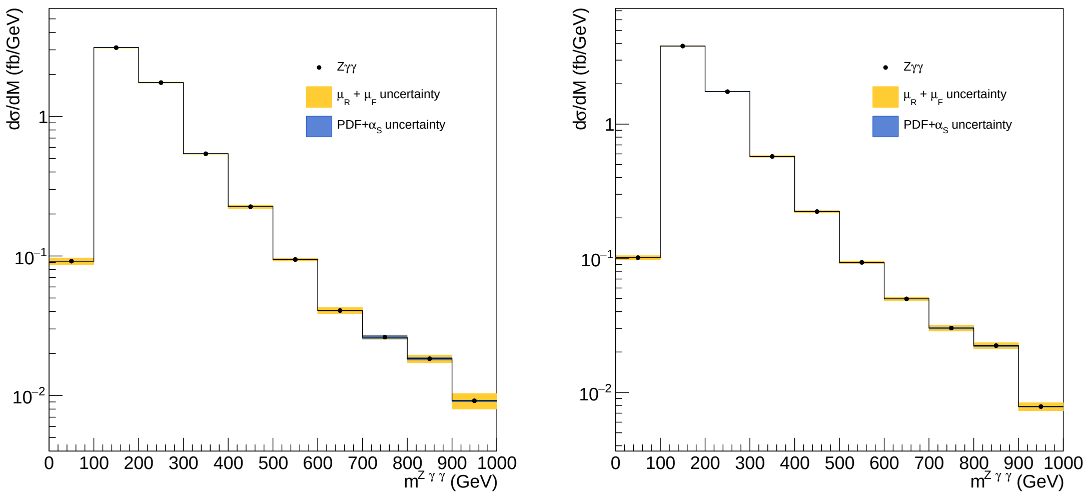

Figure 6.18: Reconstructed $Z\gamma\gamma$ mass in the electronic (left) and muonic (right) channel, in semi-log scale.

Conclusions

In my thesis work I have studied the characteristics of the 13 TeV $W\gamma\gamma$ and $Z\gamma\gamma$ physics within the Compact Muon Solenoid at the Large Hadron Collider, using Run 2 data. I used the 13 TeV Monte Carlo samples in order to characterize the phase space of the $V\gamma\gamma$ topology, and to obtain the differential cross sections as a function of the most sensitive observables of the events. The Mini-AOD format has been utilized for the analysis. In particular, I studied the leptonic decay of the $W^{\pm}$ and Z bosons, retrieving a fiducial phase space region for the cross section measurement. I developed a Rivet routine for the analysis and I validated it by comparing the Mini-AOD results with those extracted from a parallel analysis (performed without making use of Rivet) on Nano-AOD format samples. I also evaluated the theoretical uncertainties on the differential cross section distributions, in order to give an estimate of their contribution on the cross sections measurement. The computation of theoretical uncertainties is a fundamental step in the cross sections measurement, and the uncertainties investigated in this work are those deriving from the experimental determination of the Parton Distribution Functions and the strong coupling constant, and from the choice of the renormalization and the factorization scale. I have first computed the distinct contributes to the theoretical uncertainties separately, and then I added them in quadrature. The total error resulted to be smaller than what was obtained in the 8 TeV analysis and it is expected to be subdominant with respect to the statistical contribution that will affect the data. The Monte Carlo differential cross section distributions obtained in this thesis work will be used in the 13 TeV CMS analysis as a starting point for the extraction of the expected limits on anomalous quartic gauge couplings that may occur in $V\gamma\gamma$ processes, as possible evidence of beyond Standard Model effects. The evaluation of the expected limits will be performed by means of comparisons between the Standard Model distributions here produced and those obtained by a new simulation that introduces in the evaluation of the matrix elements anomalous couplings effects. The presence of anomalous couplings will increase the production of $V\gamma\gamma$ with increasing momentum, therefore the expected limits will be extracted in regions of the phase space where the p_T of the leading photon of the vertex exceeds at least 70 GeV. A maximum likelihood method will be used to provide limits at 95% confidence level.

Bibliography

[1] S. Chatrchyan *et al.* [CMS Collaboration], "Observation of a New Boson with Mass Near 125 GeV in pp Collisions at $\sqrt{s}$ = 7 and 8 TeV", JHEP **1306** (2013) 081.

[2] G. Aad *et al.* [ATLAS Collaboration], "Observation of a new particle in the search for the Standard Model Higgs boson with the ATLAS detector at the LHC", Phys. Lett. B **716** (2012) 1.

[3] M. Thomson, "Modern particle physics", Cambridge University Press (2013).

[4] E. Fermi, "Tentativo di una Teoria Dei Raggi β", Il Nuovo Cimento (1924-1942), Sep. 20 (2008) **11** n.1, 1.

[5] N. Cabibbo, "Unitary Symmetry and Leptonic Decays", Phys. Rev. Lett. **10** (1963) 531.

[6] M. Kobayashi and T. Maskawa, "CP Violation in the Renormalizable Theory of Weak Interaction", Prog. Theor. Phys. **49** (1973) 652.

[7] S. Descotes-Genon and P. Koppenburg, "The CKM Parameters", Ann. Rev. Nucl. Part. Sci. **67** (2017) 97.

[8] S. L. Glashow, "The renormalizability of vector meson interactions", Nucl. Phys. **10** (1959) 107.

[9] A. Salam and J. C. Ward, "Weak and electromagnetic interactions", Nuovo Cim. **11** (1959) 568.

[10] S. Weinberg, "A Model of Leptons", Phys. Rev. Lett. **19** (1967) 1264.

[11] C. N. Yang and R. L. Mills, "Conservation of Isotopic Spin and Isotopic Gauge Invariance", Phys. Rev. **96** (1954) 191.

[12] M. Tanabashi *et al.* [Particle Data Group], "Review of Particle Physics", Phys. Rev. D **98** (2018) no.3, 030001.

[13] G. Knippen, "Triple and Quartic Gauge Couplings", Particle Physics at the LHC - Seminar Report, June 17, 2014.

[14] A. Deur, S. J. Brodsky and G. F. de Teramond, "The QCD Running Coupling", Prog. Part. Nucl. Phys. **90** (2016) 1.

[15] G. Arnison *et al.* [UA1 Collaboration], "Experimental Observation of Isolated Large Transverse Energy Electrons with Associated Missing Energy at $\sqrt{s}$ = 540 GeV", Phys. Lett. **122B** (1983) 103.

[16] G. Arnison *et al.* [UA1 Collaboration], "Experimental Observation of Lepton

Pairs of Invariant Mass Around 95- GeV/c^2 at the CERN SPS Collider", Phys. Lett. **126B** (1983) 398.

[17] P. W. Higgs, "Broken Symmetries and the Masses of Gauge Bosons", Phys. Rev. Lett. **13** (1964) 508.

[18] F. Englert and R. Brout, "Broken Symmetry and the Mass of Gauge Vector Mesons", Phys. Rev. Lett. **13** (1964) 321.

[19] J. Goldstone, A. Salam and S. Weinberg, "Broken Symmetries", Phys. Rev. **127** (1962) 965.

[20] J. Ellis, M. K. Gaillard and D. V. Nanopoulos, "A Historical Profile of the Higgs Boson" (2012).

[21] E. J. Weinberg, S. R. Coleman, "Radiative corrections as the origin of spontaneous symmetry breaking", Phys. Rev. D. **7** (1973) 6.

[22] B. W. Lee, C. Quigg, H. B. Thacker, "The Strength of Weak Interactions at Very High-Energies and the Higgs Boson Mass", Phys. Rev. Lett. **38** (1977) 16.

[23] ALEPH, DELPHI, L3, OPAL Collaborations, and LEP Working Group for Higgs Boson Searches, "Search for the standard model Higgs boson at LEP", Phys. Lett. B **565** (2003) 61.

[24] CDF and D0 Collaborations, "Combination of Tevatron Searches for the Standard Model Higgs Boson in the W^+ W^- Decay Mode", Phys. Rev. Lett. **104** (2010) 061802.

[25] S. Dittmaier *et al.* [LHC Higgs Cross Section Working Group], "Handbook of LHC Higgs Cross Sections: 1. Inclusive Observables".

[26] G. Aad *et al.* [ATLAS and CMS Collaborations], "Combined Measurement of the Higgs Boson Mass in pp Collisions at $\sqrt{s} = 7$ and 8 TeV with the ATLAS and CMS Experiments", Phys. Rev. Lett. **114** (2015) 191803.

[27] NobelPrize.org, The Nobel Prize in Physics 2013, https://www.nobelprize.org/prizes/physics/2013/summary/.

[28] F. Abe *et al.* [CDF Collaboration], "Observation of top quark production in $\bar{p}p$ collisions", Phys. Rev. Lett. **74** (1995) 2626.

[29] J. Erler and M. Schott, "Electroweak Precision Tests of the Standard Model after the Discovery of the Higgs Boson", Prog. Part. Nucl. Phys. **106** (2019) 68.

[30] M. Drees, "Dark Matter Theory", PoS ICHEP **2018** (2019) 730.

[31] M. Felcini, "Searches for Dark Matter Particles at the LHC", 53rd Rencontres de Moriond on Cosmology, March 17-24, 2018, La Thuile, Italy.

[32] D. H. Weinberg *et al.*, "Observational Probes of Cosmic Acceleration", Phys. Rep., **530** (2013) 87-255.

[33] E. K. Akhmedov, G. C. Branco and M. N. Rebelo, "Seesaw mechanism and structure of neutrino mass matrix", Phys. Lett. B **478** (2000) 215.

[34] C. Degrande, N. Greiner, W. Kilian, O. Mattelaer, H. Mebane, T. Stelzer, S. Willenbrock and C. Zhang, "Effective Field Theory: A Modern Approach to Anomalous Couplings", Annals Phys. **335** (2013) 21.

[35] M. Baak *et al.*, "Working Group Report: Precision Study of Electroweak Interactions", Int. J. Mod. Phys. A **29** (2014) no.26, 1430053.

[36] F. Behner, "WW and ZZ production at LEP", PoS silafae **-III** (2000) 003.

[37] P. Mastrandrea [CDF and D0 Collaborations], "Multi-boson production", 29th International Conference on Physics in Collision, (PIC 2009) Kobe, Japan, Aug. 30-Sep. 2, (2009).

[38] D. R. Green, P. Meade and M. A. Pleier, "Multiboson interactions at the LHC", Rev. Mod. Phys. **89** (2017) no.3, 035008.

[39] M. Schott and J. Zhu, "Diboson production in proton-proton collisions at $\sqrt{s} = 7$ TeV", Int. J. Mod. Phys. A **29** (2014) no.26, 1430053.

[40] S. Chatrchyan *et al.* [CMS Collaboration], "Measurement of the $W\gamma$ and $Z\gamma$ inclusive cross sections in pp collisions at $\sqrt{s} = 7$ TeV and limits on anomalous triple gauge boson couplings", Phys. Rev. D **89** (2014) no.9, 092005.

[41] G. Aad *et al.* [ATLAS Collaboration], "Measurement of $W\gamma$ and $Z\gamma$ production cross sections in pp collisions at $\sqrt{s} = 7$ TeV and limits on anomalous triple gauge couplings with the ATLAS detector", Phys. Lett. B **717** (2012) 49.

[42] V. Khachatryan *et al.* [CMS Collaboration], "Measurement of the $\mathrm{W}^+\mathrm{W}^-$ cross section in pp collisions at $\sqrt{s} = 8$ TeV and limits on anomalous gauge couplings", Eur. Phys. J. C **76** (2016) no.7, 401.

[43] G. Aad *et al.* [ATLAS Collaboration], "Measurement of total and differential W^+W^- production cross sections in proton-proton collisions at $\sqrt{s} = 8$ TeV with the ATLAS detector and limits on anomalous triple-gauge-boson couplings", JHEP **1609** (2016) 029.

[44] S. Chatrchyan *et al.* [CMS Collaboration], "Measurement of the Sum of WW and WZ Production with W+Dijet Events in pp Collisions at $\sqrt{s} = 7$ TeV", Eur. Phys. J. C **73** (2013) no.2, 2283.

[45] G. Aad *et al.* [ATLAS Collaboration], "Measurement of the $WW + WZ$ cross section and limits on anomalous triple gauge couplings using final states with one lepton, missing transverse momentum, and two jets with the ATLAS detector at $\sqrt{\mathrm{s}} = 7$ TeV", JHEP **1501** (2015) 049.

[46] V. Khachatryan *et al.* [CMS Collaboration], "Measurement of the WZ production cross section in pp collisions at $\sqrt{s} = 7$ and 8 TeV and search for anomalous triple gauge couplings at $\sqrt{s} = 8$ TeV", Eur. Phys. J. C **77** (2017) no.4, 236.

[47] G. Aad *et al.* [ATLAS Collaboration], "Measurement of the $W^{\pm}Z$ production cross section and limits on anomalous triple gauge couplings in proton-proton collisions at $\sqrt{s} = 7$ TeV with the ATLAS detector", Phys. Lett. B

709 (2012) 341.

[48] G. Aad *et al.* [ATLAS Collaboration], "Measurements of $W^{\pm}Z$ production cross sections in pp collisions at $\sqrt{s}$ = 8 TeV with the ATLAS detector and limits on anomalous gauge boson self-couplings" Phys. Rev. D **93** (2016) no.9, 092004.

[49] S. Chatrchyan *et al.* [CMS Collaboration], "Measurement of the ZZ Production Cross Section and Search for Anomalous Couplings in 2l2l ' Final States in pp Collisions at $\sqrt{s}$ = 7 TeV", JHEP **1301** (2013) 063.

[50] V. Khachatryan *et al.* [CMS Collaboration], "Measurement of the $pp \to ZZ$ production cross section and constraints on anomalous triple gauge couplings in four-lepton final states at $\sqrt{s}$ =8 TeV," Phys. Lett. B **740** (2015) 250.

[51] G. Aad *et al.* [ATLAS Collaboration], "Measurement of ZZ production in pp collisions at $\sqrt{s}$ = 7 TeV and limits on anomalous ZZZ and $ZZ\gamma$ couplings with the ATLAS detector", JHEP **1303** (2013) 128.

[52] M. Aaboud *et al.* [ATLAS Collaboration], "Measurement of the ZZ production cross section in proton-proton collisions at $\sqrt{s}$ = 8 TeV using the $ZZ \to \ell^-\ell^+\ell'^-\ell'^+$ and $ZZ \to \ell^-\ell^+\nu\bar{\nu}$ channels with the ATLAS detector", JHEP **1701** (2017) 099.

[53] S. Chatrchyan *et al.* [CMS Collaboration], "Search for $WW\gamma$ and $WZ\gamma$ production and constraints on anomalous quartic gauge couplings in pp collisions at $\sqrt{s}$ = 8 TeV", Phys. Rev. D **90** (2014) no.3, 032008.

[54] M. Aaboud *et al.* [ATLAS Collaboration], "Search for triboson $W^{\pm}W^{\pm}W^{\mp}$ production in pp collisions at $\sqrt{s}$ = 8 TeV with the ATLAS detector", Eur. Phys. J. C **77** (2017) no.3, 141.

[55] A. M. Sirunyan *et al.* [CMS Collaboration], "Search for the production of $W^{\pm}W^{\pm}W^{\mp}$ events at $\sqrt{s}$ = 13 TeV", Phys. Rev. D **100** (2019), 012004.

[56] S. Chatrchyan *et al.* [CMS Collaboration], "Measurement of the Hadronic Activity in Events with a Z and Two Jets and Extraction of the Cross Section for the Electroweak Production of a Z with Two Jets in pp Collisions at $\sqrt{s}$ = 7 TeV", JHEP **1310** (2013) 062.

[57] V. Khachatryan *et al.* [CMS Collaboration], "Measurement of electroweak production of a W boson and two forward jets in proton-proton collisions at $\sqrt{s}$ = 8 TeV", JHEP **1611** (2016) 147.

[58] V. Khachatryan *et al.* [CMS Collaboration], "Measurement of electroweak production of two jets in association with a Z boson in proton-proton collisions at $\sqrt{s}$ = 8 TeV", Eur. Phys. J. C **75** (2015) no.2, 66.

[59] V. Khachatryan *et al.* [CMS Collaboration], "Measurement of electroweak-induced production of Wγ with two jets in pp collisions at $\sqrt{s}$ = 8 TeV and constraints on anomalous quartic gauge couplings", JHEP **1706** (2017) 106.

[60] M. Aaboud *et al.* [ATLAS Collaboration], "Search for anomalous electroweak production of WW/WZ in association with a high-mass dijet system in pp collisions at $\sqrt{s} = 8$ TeV with the ATLAS detector", Phys. Rev. D **95** (2017) no.3, 032001.

[61] V. Khachatryan *et al.* [CMS Collaboration], "Study of vector boson scattering and search for new physics in events with two same-sign leptons and two jets", Phys. Rev. Lett. **114** (2015) no.5, 051801.

[62] G. Aad *et al.* [ATLAS Collaboration], "Evidence for Electroweak Production of $W^{\pm}W^{\pm}jj$ in pp Collisions at $\sqrt{s} = 8$ TeV with the ATLAS Detector", Phys. Rev. Lett. **113** (2014) no.14, 141803.

[63] G. Aad *et al.* [ATLAS Collaboration], "Measurements of $W^{\pm}Z$ production cross sections in pp collisions at $\sqrt{s} = 8$ TeV with the ATLAS detector and limits on anomalous gauge boson self-couplings", Phys. Rev. D **93** (2016) no.9, 092004.

[64] A. M. Sirunyan *et al.* [CMS Collaboration], "Measurements of the pp $\rightarrow W\gamma\gamma$ and pp $\rightarrow Z\gamma\gamma$ cross sections and limits on anomalous quartic gauge couplings at $\sqrt{s} = 8$ TeV", JHEP **1710** (2017) 072.

[65] G. Aad *et al.* [ATLAS Collaboration], "Evidence of W$\gamma\gamma$ Production in pp Collisions at $\sqrt{s} = 8$ TeV and Limits on Anomalous Quartic Gauge Couplings with the ATLAS Detector", Phys. Rev. Lett. **115** (2015) no.3, 031802.

[66] G. Aad *et al.* [ATLAS Collaboration], "Measurements of $Z\gamma$ and $Z\gamma\gamma$ production in pp collisions at $\sqrt{s} = 8$ TeV with the ATLAS detector", Phys. Rev. D **93** (2016) no.11, 112002.

[67] G. Bozzi, F. Campanario, M. Rauch and D. Zeppenfeld, "$W^{+-}\gamma\gamma$ production with leptonic decays at NLO QCD", Phys. Rev. D **83** (2011) 114035.

[68] G. Bozzi, F. Campanario, M. Rauch and D. Zeppenfeld, "$Z\gamma\gamma$ production with leptonic decays and triple photon production at next-to-leading order QCD," Phys. Rev. D **84** (2011) 074028.

[69] M. H. Seymour and M. Marx, "LHC phenomenology", Springer International Publishing (2015), 287-319 .

[70] A. Buckley *et al.*, "General-purpose event generators for LHC physics", Phys. Rept. **504** (2011) 145.

[71] F. Maltoni, T. McElmurry, R. Putman and S. Willenbrock, "Choosing the Factorization Scale in Perturbative QCD" (2007).

[72] S. Hoeche, F. Krauss, N. Lavesson, L. Lonnblad, M. Mangano, A. Schalicke and S. Schumann, "Matching parton showers and matrix elements", from "HERA and the LHC: A Workshop on the implications of HERA for LHC physics: Proceedings Part A" (2005), 288-289.

[73] F. Klimpel, "Improved tuning methods for Monte Carlo generators" (2018).

[74] R. Vogt, "The Usage of the K factor in heavy ion physics", Acta Phys. Hung.

A **17** (2003) 75.

[75] Z. Nagy and D. E. Soper, "Ordering variable for parton showers", JHEP **1406** (2014) 178.

[76] J. C. Collins, "Sudakov form-factors", Adv. Ser. Direct. High Energy Phys. **5** (1989) 573.

[77] C. Oleari, "The POWHEG-BOX", Nucl. Phys. Proc. Suppl. **205-206** (2010) 36.

[78] S. Frixione, F. Stoeckli, P. Torrielli, B. R. Webber and C. D. White, "The MC@NLO 4.0 Event Generator" (2010).

[79] J. Alwall *et al.*, "The automated computation of tree-level and next-to-leading order differential cross sections, and their matching to parton shower simulations", JHEP **1407** (2014) 079.

[80] T. Sjostrand, S. Mrenna and P. Z. Skands, "PYTHIA 6.4 Physics and Manual", JHEP **0605** (2006) 026.

[81] E. Boos *et al.*, "Generic User Process Interface for Event Generators", Physics at TeV colliders. Proceedings, Euro Summer School, Les Houches, France, May 21-June 1, 2001.

[82] A. Buckley, H. Hoeth, H. Lacker, H. Schulz and J. E. von Seggern, "Systematic event generator tuning for the LHC", Eur. Phys. J. C **65** (2010) 331.

[83] M. Bahr *et al.*, "Herwig++ Physics and Manual", Eur. Phys. J. C **58** (2008) 639.

[84] A. Lebedev, L. Sinclair, E. Strickland and J. Vazdik, "Color coherence in photon induced reactions", In *Hamburg 1995/96, Future physics at HERA* 560-565.

[85] J. M. Butterworth, J. R. Forshaw and M. H. Seymour, "Multiparton interactions in photoproduction at HERA", Z. Phys. C **72** (1996) 637.

[86] J. Alwall, M. Herquet, F. Maltoni, O. Mattelaer and T. Stelzer, "MadGraph 5 : Going Beyond", JHEP **1106** (2011) 128.

[87] D. Spehler and S. F. Novaes, "Helicity wave functions for massless and massive spin-2 particles", Phys. Rev. D **44** (1991) 3990.

[88] T. Gleisberg, S. Hoeche, F. Krauss, M. Schonherr, S. Schumann, F. Siegert and J. Winter, "Event generation with SHERPA 1.1", JHEP **0902** (2009) 007.

[89] P. Skands, S. Carrazza and J. Rojo, "Tuning PYTHIA 8.1: the Monash 2013 Tune", Eur. Phys. J. C **74** (2014) no.8, 3024.

[90] A. M. Sirunyan *et al.* [CMS Collaboration], "Extraction and validation of a new set of CMS PYTHIA8 tunes from underlying-event measurements", (2018) CMS-PAS-GEN-17-001.

[91] L. Evans and P. Bryant, "LHC Machine", JINST **3** (2008) S08001.

[92] G. Aad *et al.* [ATLAS Collaboration], "The ATLAS Experiment at the CERN Large Hadron Collider", JINST **3** (2008) S08003.

[93] S. Chatrchyan *et al.* [CMS Collaboration], "The CMS Experiment at the CERN LHC", JINST **3** (2008) S08004.

[94] A. A. Alves, Jr. *et al.* [LHCb Collaboration], "The LHCb Detector at the LHC",

JINST **3** (2008) S08005.

[95] K. Aamodt *et al.* [ALICE Collaboration], "The ALICE experiment at the CERN LHC", JINST **3** (2008) S08002.

[96] CMS Collaboration, "CMS tracker technical design report: Technical Design Report", Technical Design Report CMS, CERN, Geneva, 1998.

[97] CMS Collaboration, "The CMS electromagnetic calorimeter: Technical design report", Technical Design Report CMS, CERN, Geneva, 1997.

[98] CMS Collaboration, "The CMS hadron calorimeter: Technical design report", Technical Design Report CMS, CERN, Geneva, 1997.

[99] CMS Collaboration, "The CMS magnet project: Technical design report", Technical Design Report CMS, CERN, Geneva, 1997.

[100] CMS Collaboration, "The CMS muon project: Technical Design Report", Technical Design Report CMS, CERN, Geneva, 1997.

[101] A. Buckley, J. Butterworth, L. Lonnblad, D. Grellscheid, H. Hoeth, J. Monk, H. Schulz and F. Siegert, "Rivet user manual", Comput. Phys. Commun. **184** (2013) 2803.

[102] M. Dobbs and J. B. Hansen, "The HepMC C++ Monte Carlo event record for High Energy Physics", Comput. Phys. Commun. **134** (2001) 41.

[103] A. M. Sirunyan *et al.* [CMS Collaboration], "Particle-flow reconstruction and global event description with the CMS detector", JINST **12** (2017) no.10, P10003.

[104] G. Boudoul *et al.*, "Monte Carlo Production Management at CMS", 2015 J. Phys.: Conf. Ser. 664 072018.

[105] G. Petrucciani *et al.* [CMS Collaboration], "Mini-AOD: A New Analysis Data Format for CMS", J. Phys. Conf. Ser. **664** (2015) no.7, 7.

[106] R. Plačakytė [H1 and ZEUS Collaborations], "Structure Functions and PDF determination at HERA", 48th Rencontres de Moriond on QCD and High Energy Interactions, 9-16 Mar 2013. La Thuile, Italy.

[107] S. Forte and G. Watt, "Progress in the Determination of the Partonic Structure of the Proton", Ann. Rev. Nucl. Part. Sci. **63** (2013) 291.

[108] R. Placakyte [H1 and for the ZEUS Collaboration], "Parton Distribution Functions", XXXI Physics in Collision, Vancouver, BC Canada, 28 Aug-1 Sep, 2011.

[109] L. Harland-Lang *et al.*, "Parton distributions in the LHC era: MMHT 2014 PDFs", Eur. Phys. J. C75, 204 (2015).

[110] S. Dulat *et al.*, "New parton distribution functions from a global analysis of quantum chromodynamics", Phys. Rev. D **93** (2016) no.3, 033006.

[111] R. D. Ball *et al.* [NNPDF Collaboration], "Parton distributions from high-precision collider data", Eur. Phys. J. C **77** (2017) no.10, 663.

[112] H. Abramowicz *et al.* [ZEUS Collaboration], "Deep inelastic cross-section

measurements at large y with the ZEUS detector at HERA" Phys. Rev. D **90** (2014) no.7, 072002.

[113] S. Alekhin, J. Blümlein, S. Moch and R. Placakyte, "Parton distribution functions, α_s, and heavy-quark masses for LHC Run II", Phys. Rev. D **96** (2017) no.1, 014011.

[114] P. Jimenez-Delgado and E. Reya, "Delineating parton distributions and the strong coupling", Phys. Rev. D **89**, (2014) 074049.

[115] J. Butterworth *et al.*, "PDF4LHC recommendations for LHC Run II", J. Phys. G **43** (2016) 023001.

[116] G. Watt and R. S. Thorne, "Study of Monte Carlo approach to experimental uncertainty propagation with MSTW 2008 PDFs", JHEP **1208** (2012) 052.

[117] M. Schmelling, "Averaging correlated data", Phys. Scripta 51 (1995) 676.

[118] A. Buckley, J. Ferrando, S. Lloyd, K. Nordström, B. Page, M. Rüfenacht, M. Schönherr and G. Watt, "LHAPDF6: parton density access in the LHC precision era", Eur. Phys. J. C **75** (2015) 132.

Sail forth – steer for the deep waters only,
Reckless, O soul, exploring, I with thee, and thou with me,
For we are bound where mariner has not yet dared to go,
And we will risk the ship, ourselves and all.

---

from 'Passage to India', Walt Whitman, American poet and writer (1819-1892)